Photoconductive Metasurfaces for Terahertz Applications

Lucy L Hale

A dissertation submitted in partial fulfillment

of the requirements for the degree of

Doctor of Philosophy

of

University College London.

Department of Electronic & Electrical Engineering

University College London

June 3, 2021

I, Lucy L Hale, confirm that the work presented in this thesis is my own. Where information has been derived from other sources, I confirm that this has been indicated in the work.

Abstract

Photoconductive antennas (PCAs) are widely used as terahertz (THz) detectors for spectroscopy and imaging. However, their relatively low efficiency and sensitivity often limits the signal-to-noise and measurement capabilities of experimental systems. By replacing the photoconductive region with an all-dielectric, fully-absorbing metasurface the efficiency and sensitivity of PCAs is substantially improved.

This thesis describes the design, modelling and experimental testing of highly absorbing metasurfaces made for the purpose of improving PCAs. Perfect absorption is achieved through the degenerate critical coupling of Mie modes. By simple modifications of the metasurface geometry, perfect absorption is obtained across the wavelength range of near-infrared ultrafast lasers commonly used for PCA excitation. When used as PCA detectors, high signal-to-noise is achieved at unprecendently low excitation powers, and extremely low dark resistance enables high sensitivity detection. Furthermore, when integrated with near-field aperture probes, the ultra-thin design of such metasurface PCAs could significantly enhance the spatial resolution and spectral sensitivity of THz near-field systems.

In addition to PCA detectors, this thesis investigates whether GaAs metasurfaces could be used for THz emission via ultrafast charge carrier dynamics. Perfect absorption is demonstrated when the metasurface is excited at oblique angles, as necessary for THz emission and out-coupling. This work suggests the possibility of efficient, adaptable and integrable THz sources which do not require external bias for operation.

Finally, this thesis explores whether metasurfaces can enhance absorption in

low-temperature materials at sub-bandgap energies. It is shown that substantial improvements in absorption are possible using degenerate critical coupling, even for materials with very low absorption coefficients. This finding invites the future development of efficient PCA detectors that use convenient, turn-key operated fiber lasers for excitation - enabling cheaper, more functional THz spectroscopy and imaging systems.

Impact Statement

In this thesis I demonstrate the design, fabrication and experimental characterisation of fully-absorbing dielectric metasurfaces. These metasurfaces are used to enhance the efficiency of terahertz (THz) ultrafast detectors, and I also suggest their use as broadband THz emitters. One of the key obstacles in THz research is the lack of efficient, sensitive detectors and powerful sources. This work is therefore relevant to the broad range of THz spectroscopy and imaging applications which require efficient detectors and emitters, such as medical and security imaging, communications and semiconductor materials research.

The metasurfaces designed in this work have particular potential to improve the spectral and spatial resolution of THz aperture near-field detectors. Near-field THz research enables the investigation of sub-wavelength local phenomena: improving these systems could further the investigation of material systems on the micron scale, such as biological samples, topological insulators and 2D materials.

Finally, the new understanding of physical mechanisms in highly absorbing dielectric metasurfaces contributes to fast-growing research on fundamental metamaterial phenomena. Metasurfaces enable the precise engineering of material properties in ultra-thin layers; in particular, dielectric metasurfaces have the potential to improve upon and replace bulk semiconductor materials in a vast range of optical and electronic devices.

This work has been disseminated through the publication of journal articles and presentations at national and international conferences.

List of Publications

Journal Publications

- **L. L. Hale**, P. P. Vabishchevich, T. Siday, C. T. Harris, T. S. Luk, S. J. Addamane, J. L. Reno, I. Brener, O. Mitrofanov "Perfect Absorption in GaAs Metasurfaces near the Bandgap Edge" *Optics Express* **28** (23) 2020.

- **L. L. Hale**, J. Keller, T. Siday, R. I. Hermans, J. Haase, J. L. Reno, I. Brener, G. Scalari, J. Faist, O. Mitrofanov, "Noninvasive Near-Field Spectroscopy of Single Subwavelength Complementary Resonators" *Laser and Photonic Reviews* **14** (4) 2020 (Cover Story).

- O. Mitrofanov, **L. L. Hale**, P. P. Vabishchevich, T. S. Luk, S. J. Addamane, J. L. Reno, I. Brener, "Perfectly Absorbing Dielectric Metasurfaces for Photodetection" *APL Photonics* **5** (10) 101304 2020.

- T. Siday, **L. L. Hale** , R. I. Hermans, O. Mitrofanov, "Resonance-enhanced terahertz nanoscopy probes" *ACS Photonics* **7** (3) 2020.

- T Siday, P.P. Vabishchevich, **L. Hale**, C. T. Harris, T. S. Luk, J. L. Reno, I. Brener, O. Mitrofanov, "Terahertz Detection with Perfectly Absorbing Photoconductive Metasurface" *NanoLetters* **19** (5) 2019.

Conference Presentations & Proceedings

- **L. Hale** *et al.*, (Contributed Oral) "Tuneable Fully Absorbing Metasurfaces for Efficient THz Detection" 45th International *Conference on Infrared, Millimeter and Terahertz Wave* (IRMMW-THz 2020).

- **L. Hale** *et al.*, (Contributed Oral) "Photoconductive Metasurfaces for Terahertz Detection" *Conference on Lasers and Electro-Optics* (CLEO 2020).

- **L. Hale** *et al.*, (Contributed Oral) "Efficient Terahertz Detection with Perfectly Absorbing Metasurface" *44th International Conference on Infrared, Millimeter and Terahertz Wave* (IRMMW-THz 2019).

- **L. Hale** *et al.*, (Contributed Oral) "Probe-Sample Interaction in Aperture-Type THz Near-Field Microscopy of Complementary Resonators" *44th International Conference on Infrared, Millimeter, and Terahertz Wave* (IRMMW-THz 2019).

- **L. Hale** et al., (Contributed Oral) "Aperture-type Collection Mode Near-Field Microscopy and Spectroscopy of Individual Sub-Wavelength THz Resonators" *Conference of Optical Terahertz Science and Technology* (OTST 2019).

- **L. Hale** et al., (Poster) "Probe-Sample Interaction in Aperture-type Collection Mode Near-Field Microscopy and Spectroscopy" *Conference of Optical Terahertz Science and Technology* (OTST 2019).

- N. W. Almond, R Hermans, **L. L. Hale** et al., " Terahertz aperture SNOM mapping of metamaterial coupled resonators " *Metamaterials, Metadevices and Metasystems*, SPIE 114601, 2020.

Acknowledgements

First and foremost, I would like to thank my supervisor Prof. Oleg Mitrofanov for providing me with every opportunity to learn new skills and grow as a researcher during my PhD, as well as his encouragement in pursuing new research avenues and career opportunities. I am also very grateful for the support and guidance of my second supervisor, Prof. Cyril Renaud - particularly for his help facilitating this project in the beginning.

Thank you to everyone in the Photonics group who has taken time out of their own work to help me and patiently answer my questions - in particular Tom Siday, Rodolfo Hermans and James Seddon. Thank you to all my friends in EEE and the Integrated Photonics and Electronics CDT for making the past three years so enjoyable.

Thank you to my family: to my parents for instilling in me a lifelong love of learning, and to Bob and John for being my biggest supporters. Finally, thank you to Richard for his patience, understanding and unique perspective - as well as his excellent proof-reading skills.

Contents

List of Figures

Chapter 1

Introduction

Terahertz (THz) radiation is electromagnetic radiation of wavelengths 100 GHz – 10 THz, which lies between infra-red and microwave radiation on the electromagnetic spectrum. Traditionally, THz radiation has been a comparatively unstudied range of the electromagnetic spectrum (despite its potential uses) owing to lack of high power THz sources and sensitive detectors [16]. However, developments since the 1980s have accelerated THz research and opened up new opportunities to study light-matter interactions at this frequency.

THz research is now a large and continually growing field with a wide range of applications. Photons in this energy range are able to excite molecular and solid vibrations, enabling the characterisation of material properties. Many electronic resonances in low-dimensional and quantum systems also typically lie in the THz region, allowing us to probe interesting charge carrier dynamics and light-matter interactions [17]. Water is also strongly absorbed at THz frequencies, enabling biological applications and use for medical diagnostics. Other uses include imaging for security purposes and astronomy, and potentially expanding the bandwidth of communication technologies.

When using THz imaging and spectroscopy techniques in the far-field the resolution achievable is determined by the diffraction limit, which is a function of the illuminating wavelength. At visible frequencies this allows imaging down to a resolution of hundreds of nanometres. However, the THz wavelength is significantly longer, limiting resolution to approximately 300 μm at 1 THz. As a result, only the

overall THz response from samples smaller than this can be studied. This poses a problem for many of the applications where THz imaging and spectroscopy would prove useful, such as studying biological samples, THz devices and solid-state materials. By acquiring knowledge about samples on a more local scale, the effects of the shape and structure of individual features could be probed, giving a more in-depth picture of the sample under investigation. Near-field microscopy techniques provide a solution to the problem of diffraction-limited imaging and spectroscopy, allowing deeply sub-wavelength features to be resolved.

Despite advances in the field, the versatility of THz systems is still often limited by the efficiency of THz sources and sensitivity of THz detectors, particularly in the near-field. The research in this thesis aims to improve photoconductive antenna detectors for use in near-field THz systems. In order to further explain the motivation for this, and the requirements of these detectors, it is necessary to briefly describe their context. This will be done by first explaining near-field microscopy, and then THz time-domain spectroscopy, which is commonly used to gain spectroscopic information both in the near-field and far-field. This allows us to understand the system which the detectors in this work are designed for, as it is a combination of these two techniques. Having provided this context, I will then discuss photoconductive antennas - a technology that is used for THz generation and detection and that will be used for the detectors developed in this project. I will review recent research into improving the sensitivity and efficiency of these devices. Finally, the topic of dielectric metasurfaces is discussed, in order to highlight the possibilities and advantages of using dielectric metasurfaces in photoconductive antenna detectors.

1.1 Near-Field Microscopy

Near-field microscopy is a technique which allows us to surpass the diffraction limit and gain information about samples on a deeply sub-wavelength scale. This is possible by placing a probe in close proximity to the object under investigation, enabling evanescent components of the electric field to be detected. These field components

decay exponentially away from the sample, and are therefore lost in far-field measurements, limiting resolution. The spatial resolution of near-field measurements is therefore not determined by the illumination wavelength (as in classical imaging) but by the properties of the near-field probe.

There are several methods for capturing these near-field components which differ in the type of probe used. One technique is to use aperture probes which illuminate or isolate the field in a sub-wavelength sized area. In collection mode, the aperture is brought close to the object and scans the surface. By placing a detecting element directly behind the aperture plane, information can be gathered about the whole object at a resolution defined by the aperture size. Carefully choosing an appropriate aperture-to-sample distance allows measurement without significantly perturbing the sample's electromagnetic response [3]. This has the potential to produce high signal-to-noise ratio measurements of entire THz devices and samples on the micrometre scale [18]. At THz wavelengths, apertures as small as 2 μm (λ/150 at 1 THz) have successfully been used in collection mode aperture studies [9, 19]. However, as the aperture size is reduced transmission through the aperture drastically decreases, meaning apertures smaller than this are impractical [20]. Alternatively, scattering near-field microscopy can be used [21, 22]. In this technique a sharp tip is brought close to the object and concentrates the field in a sub-wavelength sized spot of the sample, determined by the tip diameter. The field is usually scattered into the far-field, where it is detected. Whilst much higher resolution can be achieved (down to 40 nm at THz wavelengths [23]), the scattering efficiency from the tip into the far-field is often low, resulting in poor signal-to-noise (SNR) levels, as well as large background signals. As a result, these systems often require even higher power sources and more sensitive detection, as well as demodulation of the signal at higher harmonics to isolate the near-field information from the sample [24]. In addition, careful consideration of the tip-sample interaction needs to be taken into account in order to interpret the near-field signal observed [21].

In this thesis, detectors are designed for use in a collection-mode aperture system. Whilst aperture microscopy does not have the ultra-high resolution offered by

scattering near-field systems, it allows the sensitive investigation of a wide range of materials and devices on the micron scale. I will focus on this type of near-field system hereafter.

1.2 Terahertz Time-Domain Spectroscopy

The majority of THz frequency studies use time-domain THz spectroscopy (THz-TDS). This versatile technique forms the basis of many near and far-field systems because it provides high signal-to-noise, time-resolved measurements over the broad THz spectrum, even with relatively low power sources [25]. Given that THz devices are often developed for use in these systems, THz-TDS provides some insight into the requirements for THz sources and detectors and is therefore worth introducing before I discuss the specific THz technologies that will be used in this project.

Figure 1.1 shows an example set-up. Ultrafast femtosecond near infra-red (NIR) pulses are split into two paths - pump and probe beams - by a beam splitter. The pump beam is incident on a THz emitter, generating a broadband THz frequency pulse which is several picoseconds in length. The probe beam is used to gate a THz detector - which is only able to detect THz radiation when activated by this NIR probe pulse. By adjusting the path length for either the pump or probe beam, the delay between the pump and probe beam is adjusted - the detector thereby samples the THz field at different snapshots in time. In this way the full THz pulse is retrieved in the time-domain, providing both phase and amplitude information. A sample of interest can be placed in the THz beam path to investigate the effect of the sample on the THz field. By Fourier transforming the time-domian waveform the THz spectrum is retrieved. Normalising this to the Fourier transform of the incident THz pulse gives the spectral response of the sample in question.

Combining THz-TDS with near-field techniques enables sub-wavelength mapping of the THz field in both space and time, thus giving imaging and spectroscopic information at a spatial resolution defined by the probe. In the particular system developed at UCL [20], the near-field probe is a metallic aperture which is integrated

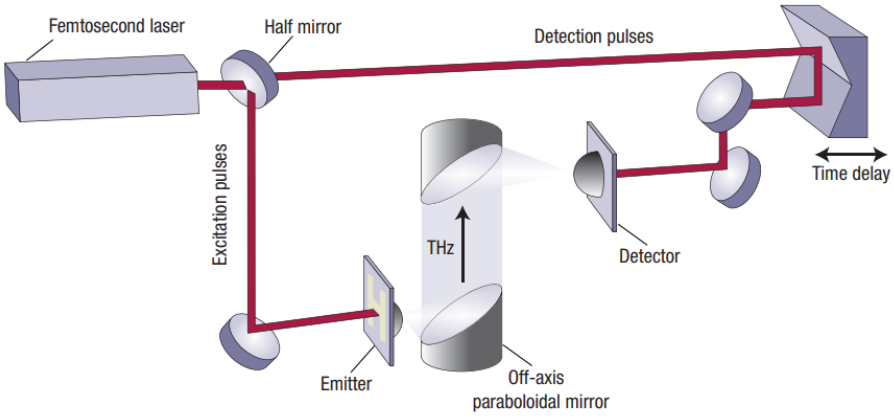

Figure 1.1: A typical THz-TDS setup (taken from [1]).

with a THz detector. This system is shown in Figure 1.2.

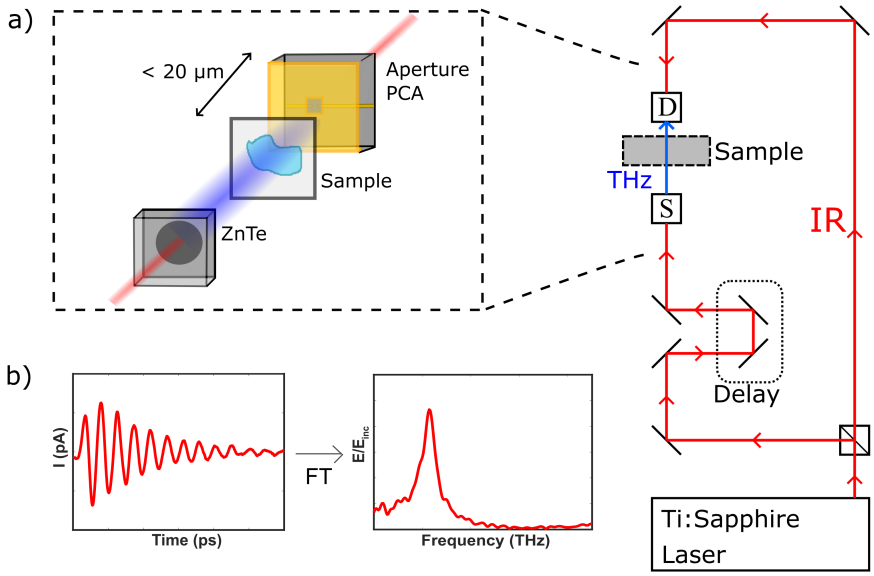

Figure 1.2: Aperture near-field THz-TDS system at UCL a) Schematic diagram of the set-up with close-up on THz region. The sample sits in the near-field of the aperture-integrated photoconductive detector. A Zinc Telluride crystal is used as a THz source. b) Example waveform from a resonant sample measured with the system. By Fourier transforming the time-domain data, spectral information is gained.

Several sources can be used for THz emission in this set-up and Figure 1.2 shows a THz pulse (blue) emitted via optical rectification in a Zinc Telluride crystal. The aperture-integrated detector is positioned in the near-field of the sample. THz waves that are transmitted through the aperture are directly detected behind

the metallic plane. Time-domain information is retrieved by changing the optical delay (as usual in TDS), but this information is now specific to an isolated, sub-wavelength sized region of the sample, defined by the size of the aperture probe. In addition, by spatially raster scanning the sample with the aperture at a fixed time delay, sub-wavelength-resolved near-field maps of the THz electric field on the sample surface are formed. Figure 1.3 gives several examples of spectroscopic information and images obtained with this system, from surface waves on graphene ribbons [2] to Mie resonances in single TiO_2 microspheres [5, 26].

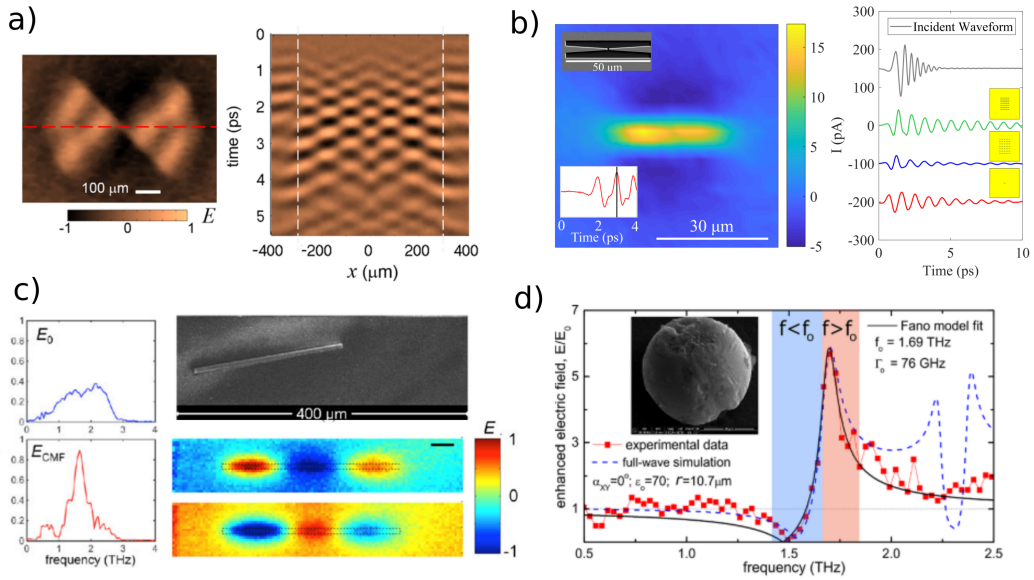

Figure 1.3: Examples of systems studied with THz aperture near-field microscopy: a) Surface plasmon waves on graphene [2]. b) Sub-wavelength complementary THz resonators as single devices and in arrays of varying periodicity [3]. c) Plasmon excitations in carbon microfibers [4]. d) Mie resonances in TiO_2 microspheres [5].

1.3 Photoconductive Antenna Detectors

Photoconductive antennas (PCAs) are very common devices used as both sources and detectors in THz systems. In their most simple form, they consist of metallic antennas on top of a photoabsorbing semiconductor layer. PCAs can be operated under continuous wave or pulsed illumination, however here we will focus on pulsed devices for simplicity, as these are most applicable to systems based on THz-

TDS. Figure 1.4 shows a simple schematic of a PCA in a pulsed detection mode. When illuminated with an ultrafast NIR pulse, electron-hole pairs are generated in the photoconductive layer. In source mode, a bias can be applied across the antenna electrodes to separate the charge carriers and create a photocurrent at THz frequencies. Alternatively, when operating as a detector, the optical pulse excites carriers and 'switches on' the detector. A photocurrent is generated by an incident THz field, which is proportional to the THz field amplitude. Carriers are collected at antenna electrodes for detection. In this way, one can see that PCAs act as both an optical switch and THz antenna, and therefore require a complex combination of both optical and electronic properties for efficient operation. In this section I will further describe these properties (focusing on PCAs for THz detection) and review how existing research has sought to achieve them.

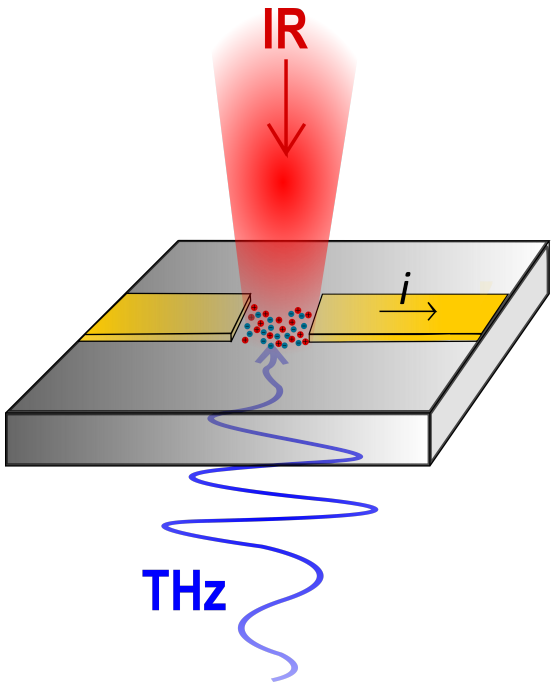

Figure 1.4: A schematic of a THz PCA.

1.3.1 Requirements for PCA Detectors

The photocurrent measured from a PCA detector is determined by a combination of the THz field amplitude present and the number of charge carriers available to respond to the THz field. Therefore, the first important requirement is to have a

high optical photon-to-charge carrier ratio, making efficient use of the optical gating pulse. In practice, this means increasing optical absorption in the photoconductive region. Secondly, in order to achieve maximum sensitivity, there must be a high contrast in conductivity between the state when optical light is present (ON state) and not present (OFF state). Note that ON/OFF contrast can be improved both by increasing the conductivity in the ON state, and increasing the resistance in the OFF state. Finally, the spectral bandwidth of the detector at high frequencies is largely determined by the carrier lifetime within the photoconductive region. Therefore, it is necessary that carriers are either detected or recombine on sub-picosecond timescales.

Satisfying all of these requirements simultaneously is a highly non-trivial problem. The most obvious way to get efficient PCA operation is to choose a photoconductive material which has beneficial properties. One of the most common materials used for this purpose is low temperature-grown gallium arsenide (LT-GaAs). As well as having relatively good carrier mobility and high dark resistivity (which are both beneficial for high signal-to-noise), it also has a very short carrier lifetime as required for fast response times and large bandwidth. This is due to the high concentration of As related defects (in particular As antisites) which act as deep trapping centres [27]. GaAs has a high band gap of $\sim$1.43 eV, which is beneficial for high dark resistivity. However, this also means that only wavelengths below $\sim$860 nm can be absorbed intrinsically. This is the reason that pulsed systems using GaAs devices (e.g. THz-TDS set-ups) usually use large Ti:Sapphire lasers that generate MHz-rate femtosecond pulses at NIR wavelengths ($\sim$800 nm). Ti:Sapphire lasers are expensive, bulky and require very sensitive handling and alignment; Chapter 5 discusses potential avenues for designing PCAs for more functional pulsed lasers. However, Ti:Sapphire lasers remain the most common lasers used in TDS systems, so here I will focus on PCAs designed for 800 nm operation, for which LT-GaAs is the dominant material used.

1.3.2 Nanostructuring PCAs for Improved Performance

Aside from clever choice of photoconductive material, the majority of recent efforts to improve PCAs have focused on nanostructuring the device in order to increase the interaction of the optical beam with the photoconductive region. One of the most popular tools for manipulating light on this scale is plasmonic nanostructures. These are metallic nanostructures deposited on the active layer which aim to couple the incident optical field to a surface plasmon wave. The surface plasmon wave is highly concentrated close to the plasmonic structure's edges, thereby strongly enhancing absorption and generating more charge carriers in this region [28].

In PCAs, plasmonic structures can either be electrically isolated or attached to the antennae in the form of plasmonic contact electrodes. Plasmonic contact electrodes have the added benefit of modifying the electronic properties of the device in addition to the optical properties: carriers are collected very efficiently because they have extremely reduced transit distances. This sometimes improves the carrier lifetime to such an extent that the deep trapping centres in low-temperature grown materials are not needed, and simple GaAs can be used as the photoconductive layer [28]. Plasmonic nanostructures are effective in a variety of different shapes: as gratings/nanorods [6, 7, 28–31], nanoislands and discs [32, 33], hexagonal designs and many others [34–36]. These nanostructures improve device performance for both sources and detectors. For example, simple nanorod contact electrodes can be used to generate 50 times more THz power in PCA sources than unstructured devices [37]. Plasmonic electrodes have in fact been used to achieve a record high PCA optical-to-terahertz conversion efficiency of 7.5%, albeit with a complicated 3D contact electrode design [30]. As detectors, interlaced contact electrodes have resulted in 40 times greater photocurrent in comparison to similar non-plasmonic devices [7].

Plasmonic structures are often combined with back reflectors such as distributed bragg reflectors (DBRs) in order to create optical nanocavities which trap photons in the photoconductive layer [8, 9, 38]. Usually, the thickness of the photoconductive region is determined by the absorption length of light ($\sim$ 0.8 μm at 800

nm); to enhance absorption it is beneficial to have a thick photoconductive layer. However, in general for the photoconductive materials used in PCAs, this distance is larger than the average distance photocarriers travel in the device - for LT-GaAs with a mobility of 400 cm^2/Vs and a carrier lifetime of 100 fs, the approximate distance charge carriers travel before recombining is only 20 nm [39]. Therefore, for efficient carrier collection it is preferable to have a thin photoconductive layer to decrease the length carriers must travel. In order to maximise absorption whilst using a thin photoconductive layer, light is trapped in an optical cavity. By optimising the thickness to support a standing wave, sub-wavelength dimensions can be used without sacrificing absorption efficiency. This technique has been used to develop PCAs with photoconductive layers as thin as 170 nm [8] - several times shorter than the absorption length in GaAs [40].

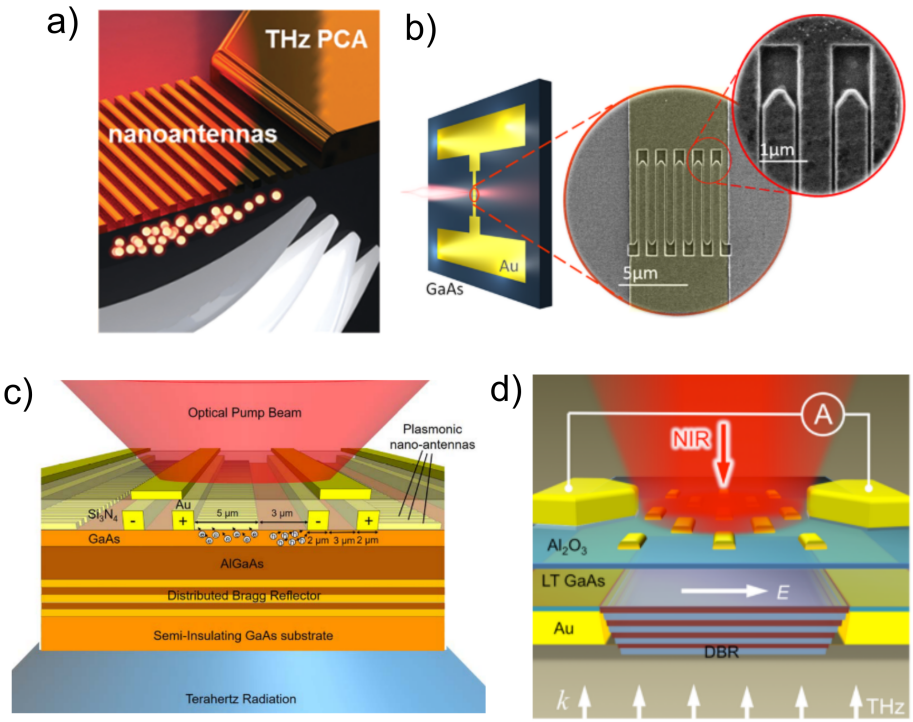

Figure 1.5: Examples of plasmonic electrodes and nanocavities in the literature: a) Schematic of plasmonic nanorods in [6]. b) Schematic and scanning electron microscope image (SEM) of interlaced plasmonic contact electrodes in [7]. c) Plasmonic contact electrodes incorporated with a DBR nanocavity in [8]. d) Nanocavity with plasmonic nanoantennas in [9].

1.3.3 Aperture Integrated PCAs

The use of nanostructuring in PCAs could be particularly useful when integrating PCAs with apertures for aperture near-field studies (as shown in Figure 1.2). In this setting we have extra considerations and constraints to take into account. For aperture PCAs the photoconductive region and antenna remain the same, but a metallic plane with an aperture is placed on the far side of the photoconductive region, isolating the THz field in the area of the aperture before entering the detector (Figure 1.6). The aperture probe is sensitive to two different types of electric fields: propagating fields polarised in the direction of the antenna, E_x, and non-propagating, evanescent fields which are polarised orthogonal to the aperture plane, E_z. The mechanism by which each of these components is detected is different (see [41] for an in-depth analysis). As a result, the probe is sensitive to the temporal derivative of the field for propagating waves ($\frac{d}{dt}E_x$), whereas for evanescent waves the probe is sensitive to the spatial derivative of the field in the direction of the antenna ($\frac{d}{dx}E_z$).

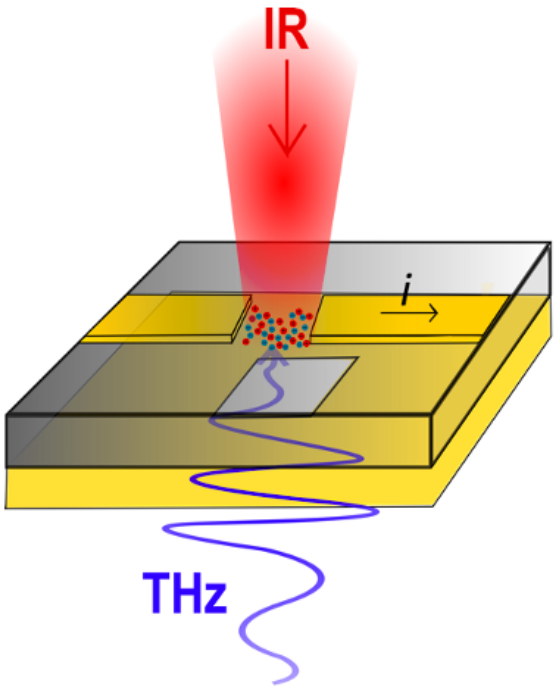

Figure 1.6: Schematic of aperture-integrated PCA detector, as used in the near-field system at UCL (Fig. 1.2).

The aperture size must be sub-wavelength to isolate near-field components and

retrieve information at the desired resolution. However, this drastically limits the intensity of the field which is able to couple through - so high detection sensitivity is all the more important. Given that the wavelength of the THz field is usually much larger than the aperture cut-off wavelength [20] only evanescent fields can to couple through the aperture - these field components decrease in intensity with distance from the aperture plane. However, electron-hole pairs are generated by the optical beam on the far (antennae) side of the detector. To illustrate the problem this poses, Figure 1.7 shows the detection of a THz surface plasmon polariton wave (SPP) travelling along a metal-air interface with a near-field aperture probe. A fraction of the SPP field couples through the aperture and decays with distance from the aperture plane. The thickness of the photoconductive layer is thereby constrained as it is necessary that carriers generated near the antennae are close enough to the aperture to be sufficiently sensitive to the weak THz field [4].

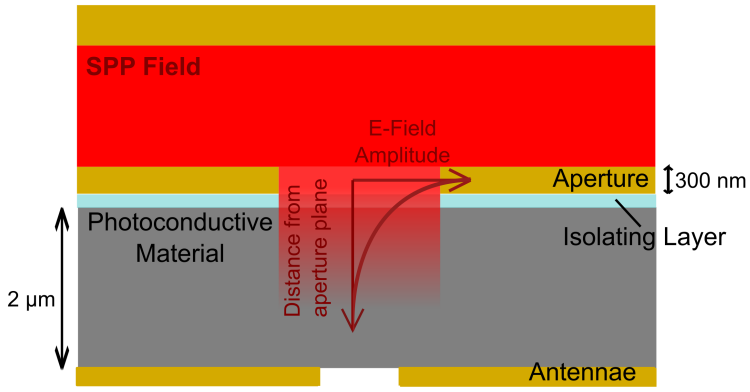

Figure 1.7: Schematic of a surface plasmon polariton (SPP) wave travelling along a metal interface, interacting with a near-field aperture probe.

As previously described, nanostructuring techniques such as plasmonics and optical cavities have enabled high sensitivity with ultra-thin PCA layers. These techniques have also been used to improve the sensitivity of aperture detectors in near-field settings [4, 9]. In the near-field, nanocavities have the added benefit of blocking transmission of the NIR beam through the structure, which could otherwise interfere with the sample under investigation.

Despite their successes in both general sources and detectors as well as near-

field probes, there are several drawbacks to the use of plasmonic structures in PCAs. Whilst they are very effective at enhancing optical absorption, they have a detrimental impact on the contrast between conductive and non-conductive states. Adding metallic structures to enhance absorption may increase the carriers present in the ON state, but they also increase the conductivity of the device in the OFF state, reducing the overall contrast and thereby reducing SNR. Furthermore, the use of metallic (often gold) structures introduces absorption losses and heating of the device, which limit the optical power that can be tolerated. Adding structures of any absorbing material, such as gold plasmonic features or dielectric DBRs, also reduces the proportion of absorption in the photoconductive region itself. In fact, in [42] it was found that whilst up to 83% of photons can be trapped in a cavity using plasmonic structures and DBRs, less than half of these are absorbed in the photoconductive region itself, meaning the rest of the optical power is effectively wasted. Finally, the addition of extra structures adds to the fabrication complexity and thickness of the device. Clearly it would be preferable to have the benefits of plasmonic structures and optical nanocavities (i.e. high optical absorption in thin photoconductive regions) without lossy metallic structures which reduce the conductivity contrast.

1.4 Dielectric Metasurfaces

Metamaterials have become an extremely active field of research in recent decades due to their ability to tailor the optical properties of materials by controlling the material geometry on a sub-wavelength scale [43]. They consist of periodic, sub-wavelength sized structures known as meta-atoms, which can be varied in size and shape in order to manipulate incident electromagnetic waves in a controlled way. This results in exotic material properties that are not found in nature. In planar metamaterials known as metasurfaces, these meta-atoms are arranged in a single layer slab of sub-wavelength thickness which can be conveniently fabricated using optical or electron-beam lithography. When incorporated into optoelectronic devices, metasurfaces allow us to design devices with desirable functionalities by

simply engineering the meta-atom design.

Metasurfaces can be made from both metallic and dielectric meta-atoms. In metallic structures, light is localised and manipulated using the plasmonic effect discussed in Section 1.3. Dielectric metasurfaces, on the other hand, operate by supporting resonances within the dielectric medium itself. For example, Mie resonances can be excited in individual meta-atoms (Figure 1.8), where the size of the meta-atoms are comparable to the electromagnetic radiation wavelength inside the dielectric media [44]. As a result, these resonances can be tuned in frequency by adjusting the geometry of the meta-atom. One can see that if a high refractive index media is used, dielectric metasurfaces can manipulate light below the free-space diffraction limit. In comparison to plasmonic resonances, dielectric metasurfaces can also have strong magnetic responses as well as electric, by supporting both magnetic and electric dipoles (as well as higher order multipole modes). Several extraordinary material properties have been demonstrated using dielectric metasurfaces, such as uni-directional scattering, ultra-high Q resonances and high-harmonic generation [10, 45, 46]. Dielectric metasurfaces have also been used in applications such as full colour printing [47], frequency mixers [48] and THz imaging [49].

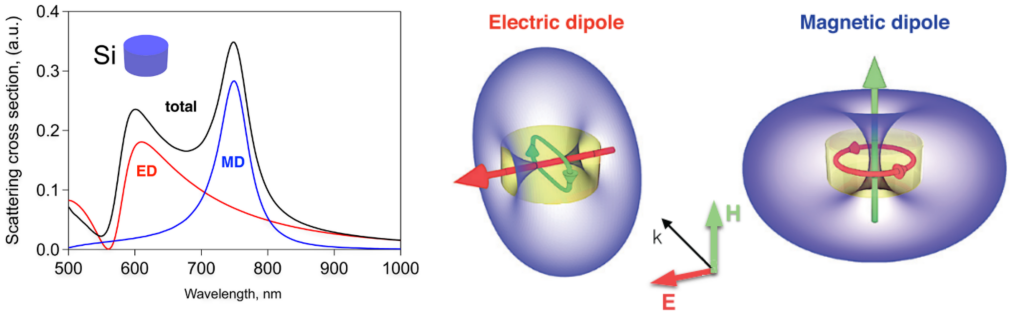

Figure 1.8: Mie Resonances in dielectric resonators: scattering spectra of a dielectric nanodisk and the radiation patterns of electric and magnetic dipoles. Taken from [10].

In the past few decades, metasurfaces have been investigated as a method to achieve enhanced light absorption in optically thin layers [50, 51], and have found uses in a wide range of applications, from photovoltaics [52–54] to infra-red sensing [55, 56]. Specifically, dielectric resonators have enabled enhanced [12, 57–59]

and even full (100%) absorption [15, 60–62] without the use of metallic elements. This suggests that dielectric metasurfaces are ideal candidates for use in PCAs, as they have the potential to increase optical absorption whilst reducing losses and potentially improve the dark resistance of the device. In addition, light is efficiently concentrated in a sub-wavelength thickness without any additional elements such as back-reflectors. This may increase detection sensitivity, particularly in aperture-integrated PCAs. The ability to modify the meta-atom shape and design means that the metasurface can be tailored to suit particular requirements of PCAs, such as achieving high optical absorption whilst also incorporating conductive channels for the necessary electronic properties.

Very recently, researchers have started using metasurfaces to improve the performance of PCAs [63]. However, most of these studies have used metallic metasurfaces, which have the drawbacks described in 1.3.3. The few studies which have used dielectric metasurfaces have either focused on improving THz collection or out-coupling (using non-absorbing metasurfaces) [64, 65] or have used metasurfaces as anti-reflection coatings [66] and as a means to enhance coupling into optical cavities using extra elements such as DBRs [12]. Thus far, there has been no studies achieving full absorption within an optically-thin photoconductive region in a PCA.

1.5 Thesis Overview

This thesis is about the design, fabrication and testing of all-dielectric metasurfaces for use in photoconductive antennas to detect THz radiation. The use of all-dielectric metasurfaces allows us to directly engineer both the photonic and electronic properties of the photoconductive region - without the use of additional structures or ohmic losses - in order to improve THz detection performance. These detectors are designed to be used in near-field microscopy systems with the aim of increasing system sensitivity and spatial resolution.

In this work, it is shown how full optical absorption can be achieved in an ultra-thin photoconductive region by using degenerate critical coupling of modes.

By engineering the metasurface through design parameters, enhanced absorption using this technique is demonstrated across the NIR range where intrinsic material absorption varies significantly. The metasurfaces are integrated into THz PCA detectors, which demonstrate high sensitivity and improved efficiency by an order of magnitude. In addition, I show how the metasurfaces can be designed for angular excitation, enabling THz emission via photo-current transients in the metasurface layer. Finally, by designing metasurface detectors which operate at the wavelength of typical turn-key pulsed fiber lasers, this work opens doors to developing near-field systems which are more robust, more compact and cheaper than current systems.

The thesis is organised in the following way. Chapter 2 first describes the physics and operational principle behind the metasurfaces developed in this work. It then describes, through simulations, how the metasurface properties can be manipulated and controlled by varying different parameters in the metasurface design. A physical explanation is provided for the effects observed. Finally, this chapter demonstrates a selection of metasurface designs which work optimally at varying wavelengths and for different levels of intrinsic material absorption, showing the versatility of the metasurface. Chapter 3 demonstrates the fabricated metasurfaces designed in Chapter 2 and shows their experimentally measured optical characteristics. An example of the metasurface-integrated PCA detector used in a typical THz-TDS detection scheme is shown, exhibiting the beneficial properties of the metasurface for this application. Chapter 4 describes the design of a metasurface for angular excitation and thereby THz emission. Chapter 5 discusses a metasurface design for a terahertz detector which operates at telecom wavelengths (around 1550 nm). Light at this wavelength has energies below the GaAs bandgap, creating challenges for efficient absorption. Despite this, it is still possible to achieve highly absorbing devices at this wavelength. Finally, Chapter 6 concludes and summarises this work, and proposes several avenues of future research that could stem from this project.

Chapter 2

Designing Metasurfaces for Terahertz Detection

The original concept for the metasurfaces shown in this Chapter was conceived by O. Mitrofanov and I. Brener. All the metasurface simulations shown here were carried out by L. Hale. The methods for tuning perfect absorption and final designs shown in Section 2.3 were devised by L. Hale. Some of the contents of this chapter have been published in [67]. Permission for the use of this content has been granted by the publisher where necessary.

As seen in Chapter 1, one of the key requirements for efficient photoconductive antennas is high optical photon-to-charge carrier conversion efficiency, which is achieved by increasing absorption in the photoconductive layer. Plasmonic structures and nano-cavities have led to increased absorption, but not without drawbacks. As an alternative, dielectric metasurfaces have proven to be effective in enhancing absorption in a thin dielectric layer without additional structures. Here, we design a dielectric metasurface to use as the photoconductive region in a THz PCA detector.

Before describing the specific metasurface design it is worth summarising some key characteristics that the metasurface needs to have for use in a THz detector:

- The metasurface should achieve maximum possible absorption, and should be adaptable across the wavelength range of typical femtosecond pulsed lasers

used in THz-TDS systems (700 - 900 nm).

- The metasurface should have photoconductive channels so that generated charge carriers can be swept to the antennae for detection.
- The metasurface should be made out of LT-GaAs due to its beneficial properties of high dark resistance and sub-picosecond carrier lifetime.
- For detectors that are to be integrated with near-field probes, the metasurface should be sub-wavelength thickness for enhanced detection sensitivity.

The following sections briefly describe the theory behind highly absorbing dielectric metasurfaces, and this is then used to develop a metasurface design considering the specifications above.

2.1 Enhanced Absorption in Dielectric Metasurfaces

It has been both postulated [15, 68, 69] and experimentally demonstrated [60–62] in recent years that subwavelength dielectric resonators - the building blocks of dielectric metasurfaces - can achieve complete absorption by exciting two resonant modes within the structure which satisfy the following three key conditions:

- Resonances must be at the same wavelength (i.e. degenerate).
- Resonances must have opposite symmetries to each other with respect to the metasurface plane (for comparison, if two modes with equal symmetry are excited, only a maximum of 50% of light can be absorbed [68]).
- Each resonance must be critically coupled to the incident field. This means that their radiative loss rate, γ, must match the material loss rate, δ , i.e. $\gamma = \delta$.

When these conditions are satisfied, reflection and transmission of the resonator cancel out to give full absorption. This is known as *degenerate critical coupling*, and is the concept used in this work to design metasurface absorbers. An explanation of the theory behind the requirements for degenerate critical coupling can be found in Appendix A.

In order to achieve degenerate critical coupling, the first challenge is to select appropriate modes that can be directly excited by the incident field. In dielectric metasurfaces the size of individual meta-atoms in a periodic array can be tailored to excite Mie modes within each meta-atom. These modes are used in the metasurfaces designed in this work. It is worth noting, however, that the degenerate critical coupling theory does not only apply to Mie modes - different modes such as plasmonic or resonant lattice modes of the entire metasurface have also been used to show enhanced absorption [48, 54–56, 58, 70–72].

In order to explain the basic metasurface design we consider a unit cell of a single dielectric cube. In this metasurface we excite the lowest order Mie mode - the magnetic dipole. The magnetic dipole mode occurs roughly when the width of the dielectric cube is comparable to the wavelength in the material, λ/n. In a symmetric cube the magnetic dipoles in all polarisations are degenerate. However, when the cube is excited by linearly polarised light, only the in-plane dipole orthogonal to the light polarisation is directly excited. This is shown in Figure 2.1a - light with E-field polarised in the y-direction directly excites the dipole in the x-direction, denoted M_x.

To achieve degenerate critical coupling we also need to excite another mode with opposing symmetry to the M_x mode. In order to do this, the idea of symmetry breaking is used [73]. By breaking the unit cell symmetry (with respect to the incident beam polarisation) of dielectric metasurfaces based on structures such as cubes and cylinders, this incident field can couple to a mode that previously could not be directly excited by the incident beam (known as a 'dark' mode). These are sometimes referred to as quasi bound-in-continuum states (BICs) [74]. With this technique, extremely high Q-factors and field enhancements have been recorded [45, 75–78]. For the metasurface developed in this work, the symmetry is broken by adding a bar structure on one side of the cube. This allows coupling of the incident field to the out-of-plane M_z mode. Figure 2.1b demonstrates this process, and the opposing symmetries of the two excited modes with respect to the metasurface plane (x-y plane) are shown in Figure 2.1c. The symmetries of the modes

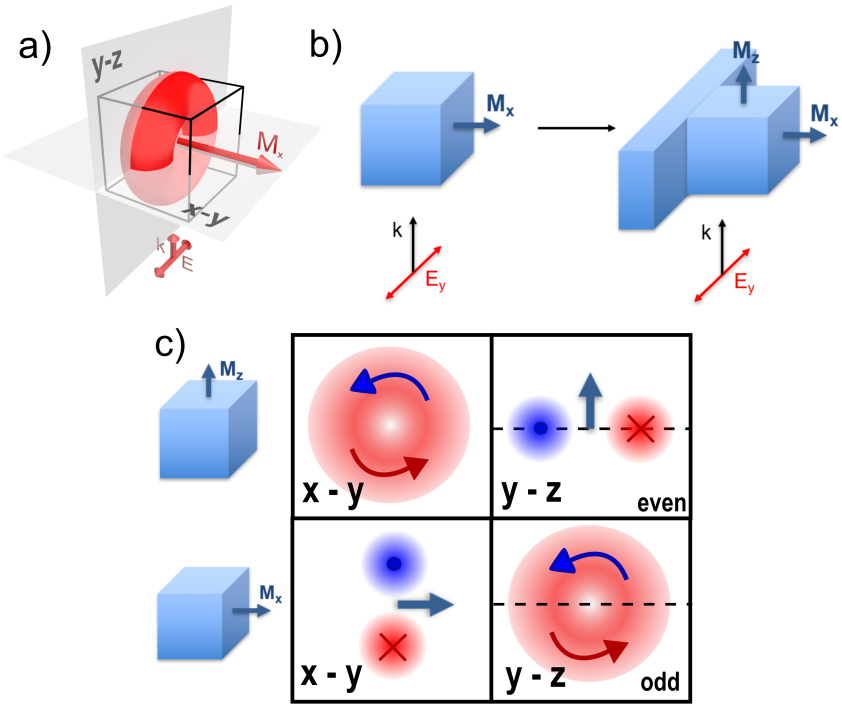

Figure 2.1: Exciting two Mie modes by symmetry breaking: a) A schematic demonstrating the fundamental magnetic dipole in a dielectric cube, oriented in the x-direction. b) Directly excited M_x mode couples to the out-of-plane M_z mode when a bar is added on one side. c) An illustrative diagram showing the opposing symmetries of the two modes with respect to the metasurface plane (x-y plane, shown by dashed line). Red and blue shapes represent the E-field distribution associated with each mode (top row - M_z mode, bottom row, M_x mode). Blue and red indicate fields polarized in opposite directions.

can be determined by observing the electric field distributions with respect to the x-y plane. The out-of-plane magnetic dipole has even symmetry with respect to the metasurface plane as the electric field distribution is symmetrical on either side of the plane, as shown by the dashed line on Fig. 2.1c. On the other hand, the in-plane magnetic dipole has odd symmetry with respect to the x-y plane, as the field is polarized in opposite directions above and below the plane. In addition to enabling the excitation of the out-of-plane mode, the bar is also necessary for the electrical operation of the metasurface, as it electrically connects dielectric cubes in rows, allowing charge carriers excited in the structure to be swept by the THz field to antennas for detection.

Now that we have a basic design for a metasurface which supports two mag-

netic dipoles of opposing symmetries, we can explore how to tailor the metasurface in order to achieve mode degeneracy at a desired wavelength and critically couple modes to the incident field for full absorption. For dispersive materials such as GaAs near the interband transition edge (800 - 860 nm), the process of satisfying these conditions simultaneously is highly non-trivial. Intrinsic material absorption in this spectral range changes rapidly with photon energy (Fig. 2.2). As a result, adjusting modal wavelengths changes the absorption loss, δ, of the mode, modifying the critical coupling condition. Therefore, if perfect absorption is achieved at a given wavelength, tuning the metasurface to a different wavelength will necessarily lead to a breakdown of the critical coupling of the modes, thereby losing the required high absorption. Due to these difficulties, several studies have focused on developing methods for designing absorbing metasurfaces at a specific wavelength. Analytic calculations have been used, however this is only possible for certain simple metasurface designs [15]. More sophisticated methods using genetic optimisation and deep learning algorithms have been explored as alternatives [79], however these are often complex and require large pre-calculated sets of training data. Consequently, typical perfectly absorbing metasurface designs are often created by trial and error, which can be time consuming and does not reveal the underlying physics of the metasurface. In the following section, I explore the underlying physics of our particular metasurface design through simulations (Section 2.2). This knowledge is then used to develop a systematic and intuitive process by which we can tailor our metasurface design to achieve perfect absorption at a wavelength of choice using a few key design parameters (Section 2.3). With this method, perfect absorption is possible at wavelengths across the GaAs bandgap, even when intrinsic material absorption is very low.

2.2 Understanding Parameter Changes

To explore how each metasurface parameter affects the modes, the metasurface design is simulated in a commercial finite-difference time-domain solver (FDTD). A single unit cell of the metasurface is simulated with periodic boundaries, surrounded

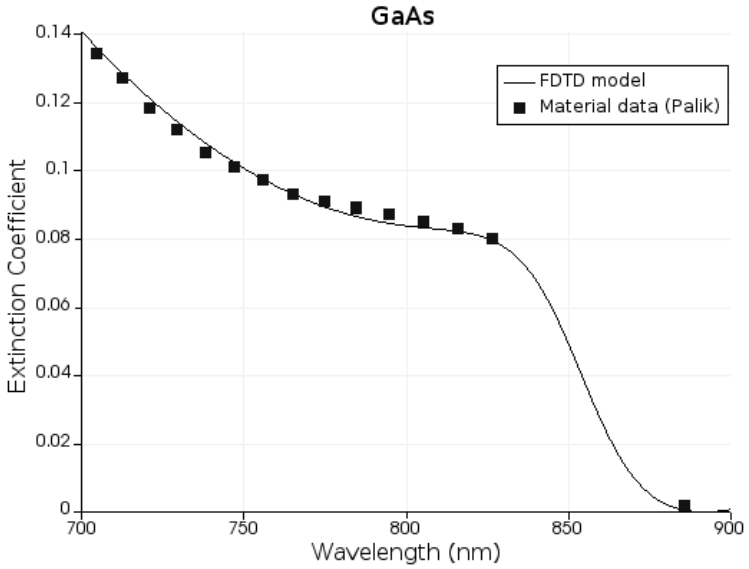

Figure 2.2: Loss in GaAs: extinction coefficient of GaAs across the bandgap. Multi-coefficient material model (see appendix B) fitted to experimental material data from [11].

by a no-loss dielectric of refractive index $n = 1.56$ to model a typical transparent substrate (e.g. glass). The structure is illuminated with a plane wave at normal incidence to the metasurface, polarised in the y-direction (as in Fig. 2.1). More information on the simulation set-up can be found in Appendix B.

Initially, the metasurface is simulated with fixed material parameters ($n = 3.684$ and $\kappa = 0.01$, independent of wavelength) to remove the effects of dispersion and solely focus on the effect of parameter sizes on the modal wavelengths. A lower extinction coefficient is used in comparison to typical values around 800 nm ($\kappa \approx 0.08$) in order to reduce the absorption and therefore linewidth of the modes, so that they are easier to distinguish and track through the parameter space.

Figure 2.3 shows the absorption spectra when a single block is simulated (Fig. 2.3a), in comparison to the block with a vertical bar introduced on one side (Fig. 2.3b). Parameter sizes were chosen in order to position modes within our desired wavelength range, and the metasurface thickness was 200 nm. When only the block is present, the lowest order mode can be seen centred around 816 nm. Magnetic field profiles at this wavelength reveal that this is the M_x dipole - we see strong magnetic field enhancement in the x-polarisation, whereas very little magnetic field is present

in the z-polarisation. In contrast, for the block with added bar, we see two distinct modes with different field profiles. In addition to the M_x mode that is now centred at 864 nm, the M_z dipole is also excited - identified by enhanced magnetic field at 902 nm in the z-polarisation. Figure 2.4 shows the corresponding electric fields for these two modes: for the M_z mode, the E-field circulates in the x-y plane; whereas for the M_x mode, the electric field circulates in the y-z plane (Fig. 2.4b). In both spectra

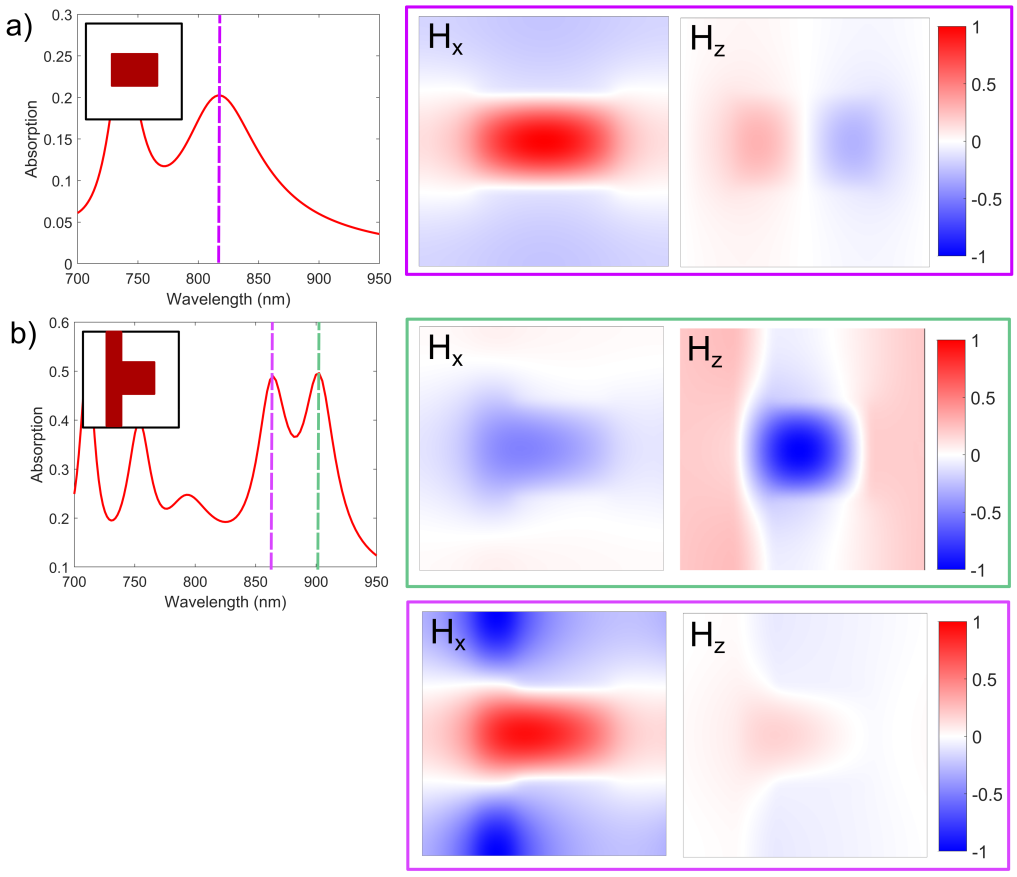

Figure 2.3: Exciting Magnetic Dipole Modes: a) Absorption Spectra when a single block is simulated. The lowest order excited mode (purple line in spectra) is the M_x mode as shown by the magnetic field distributions normalised to the maximum field in x or z polarisation at this wavelength (in this case H_x): $H_x/|H_{x,max}|$ and $H_z/|H_{x,max}|$ (purple box). b) Absorption Spectra when a block and bar is simulated. The lowest order excited mode (green line in spectra) is the M_z as shown by the magnetic field distributions normalised to the maximum field in x or z polarisation at this wavelength (in this case H_z): $H_x/|H_{z,max}|$ and $H_z/|H_{z,max}|$ (green box). The next excited mode (purple line in spectra) is the M_x mode as shown by the magnetic field distributions normalised to the maximum field in x or z polarisation at this wavelength (in this case H_x): $H_x/|H_{x,max}|$ and $H_z/|H_{x,max}|$ (purple box).

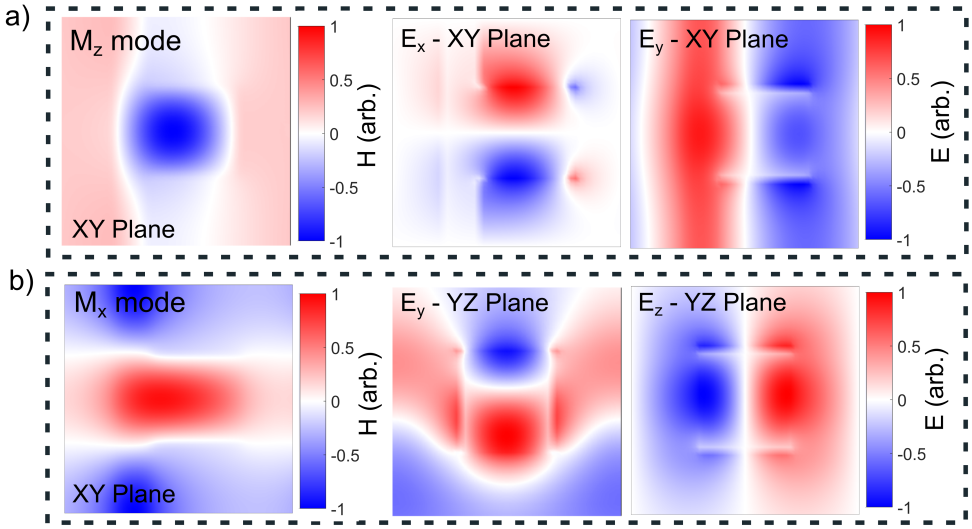

Figure 2.4: Corresponding E-Fields of Magnetic Dipoles: a) M_z mode: The magnetic field in the z-polarisation (from Fig. 2.3) and normalised electric fields E_x and E_y in the x-y plane. b) M_x mode: The magnetic field in the x-polarisation (from Fig. 2.3) and electric fields E_y and E_z in the y-z plane, at the wavelength of the magnetic dipole M_x.

in Figure 2.3, higher order modes can also be seen at shorter wavelengths. These correspond to the electric dipole in the y-polarisation and higher order electric and magnetic modes. These do not overlap with the magnetic dipole modes are not used for perfect absorption in this metasurface design.

The metasurface is characterised by six key design parameters: the block width, length and height (Figure 2.5), the bar width (Figure 2.6) and periodicities (Figure 2.8). In Figures 2.5, 2.6 and 2.8, the absorption was measured for a range of parameter sizes, and the modes are identified by dashed lines which are a linear approximation of how the mode wavelength changes as a function of the parameter. It is noted that in general the modes to not scale exactly linearly with parameter size and so this approximation should be used as a general guide only.

In Figure 2.5 the absorption spectra are shown when the block parameters are modified. The effect of increasing the block size in a given dimension is different for each mode. For all parameter dimensions, increasing the central block size allows for a larger mode volume to be accommodated and therefore the modes shift

to higher wavelengths. The modes are affected more by size increase in a given axis direction if their E-field sits in the plane involving that axis. For example, for the M_x dipole the E-field has a circular distribution and is polarised in the y-z plane (Fig. 2.4). Therefore, increasing the block size in the y or z dimensions will have a greater effect than increasing the block in the x dimension. As both modes have their E-field lying in a plane involving the y-axis, it is expected that for a simple block structure (no bar) both modes would be affected equally by the change of size in the y-direction. However, the presence of the bar modifies this. As seen in Figure 2.3, the M_x mode has a greater proportion of its field distributed in the bar, whereas the M_z mode is more centred in the cube. Given that the bar remains the same when the block height (y-direction) changes, the M_x mode is affected less.

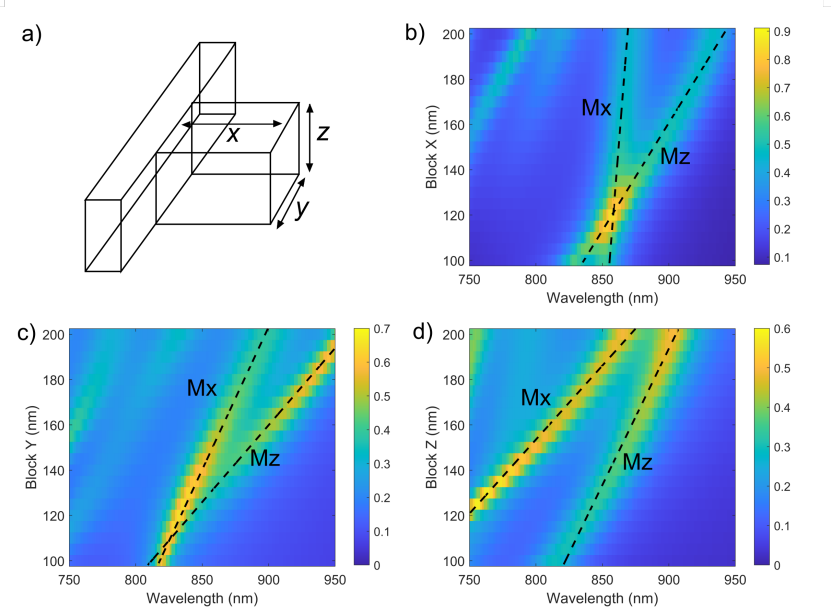

Figure 2.5: Central Block Parameters: a) Schematic of the metasurface unit cell. b) Absorption spectra for varying block width (x-direction). c) Absorption spectra for varying block length (y-direction). d) Absorption spectra for varying block height (z-direction). Dashed lines demonstrate M_x and M_z modes in the parameter space.

Figure 2.6 shows the absorption spectra for varying bar width, *b* (Fig. 2.6b). As with the central block, when the bar width increases the area of the structure in the x-y plane is expanded. The resonant wavelength of the M_z mode increases as its corresponding E-field sits in the x-y plane. For the M_x mode, although its E-field

is not polarised in the x-direction, it is also largely affected by the change in bar thickness, as a larger amount of the mode's field is distributed in the bar itself. This is demonstrated in Figure 2.7, where the spatial magnetic mode profiles for a 40 nm bar width structure are compared to a structure with a 100 nm bar width. It can be seen that - whilst the M_z field profile resides mainly in the central block and is only slightly perturbed by the change in bar width - a large proportion of the M_x field resides in the bar. Given that the electric field circulates around the centre of the magnetic dipole, a larger proportion of the electric field associated with the M_x mode will also be distributed in the bar. This proportion increases as the bar width increases. As a result, in comparison to other parameter changes, the bar width adjusts the modal wavelengths at remarkably similar rates, making it a desirable parameter to use when adjusting the metasurface for a different wavelength.

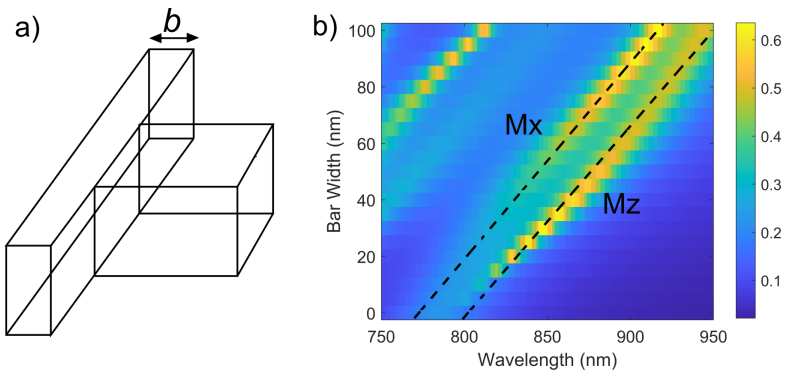

Figure 2.6: Bar Width: a) Schematic of metasurface unit cell. b) Absorption Spectra for varying bar widths. Dashed lines demonstrate M_x and M_z modes in the parameter space.

Finally, the effect of the structure periodicity is investigated (Fig. 2.8). The periodicity affects the interaction of neighbouring resonators in the metasurface. For each periodicity direction, the wavelength of one mode is changed significantly, whilst the other is less affected. For example, changing the periodicity in the y-direction corresponds to an increase in the vertical bar length in between neighbouring resonators (Fig. 2.8c). The M_x mode shifts to higher wavelengths, whereas the M_z mode is relatively unaffected, and in fact shifts slightly to lower wavelengths. This behaviour suggests that the vertical bar helps to guide the electromagnetic

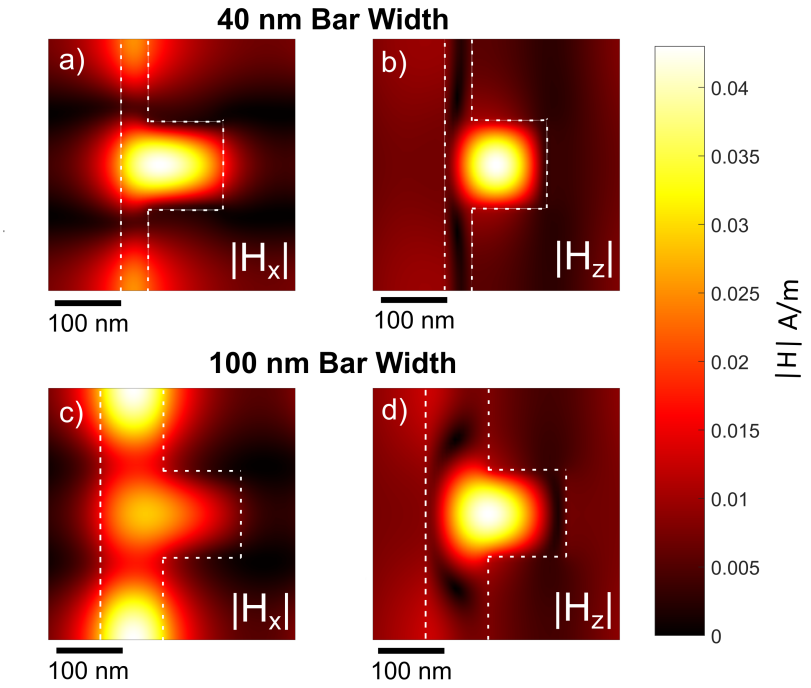

Figure 2.7: Mode Profiles for Different Bar Widths: Absolute magnetic field profiles for metasurfaces with 40 nm bar width (a & b) and 100 nm bar width (c & d). Field polarised in x-direction showing M_x mode profile (a & c) and z-direction showing M_z mode profile (b & d).

energy of the M_x mode between resonators in the y-direction. By changing the periodicity in the x-direction we also observe how resonators in parallel rows interact. Whilst the effect is less prominent than for the y-periodicity, the M_z mode is shifted to higher wavelengths and the M_x mode is relatively unaffected. By observing the E-field profile in the x-y plane of the M_z mode (Fig. 2.4a), it can be seen that the field extends all the way to the boundaries of the unit cell - suggesting some weak coupling between M_z modes in the x-direction. Given that each periodicity affects a different mode, we can infer that if both periodicities are changed simultaneously the modes will shift wavelengths at similar rates.

The information in Figures 2.5, 2.6 and 2.8 is summarised in Table 2.1, where I quantify the mode wavelength change for a 10 nm change in each parameter value. For example, the first row shows that both modes shift by 14-15 nm when the bar width changes by 10 nm.

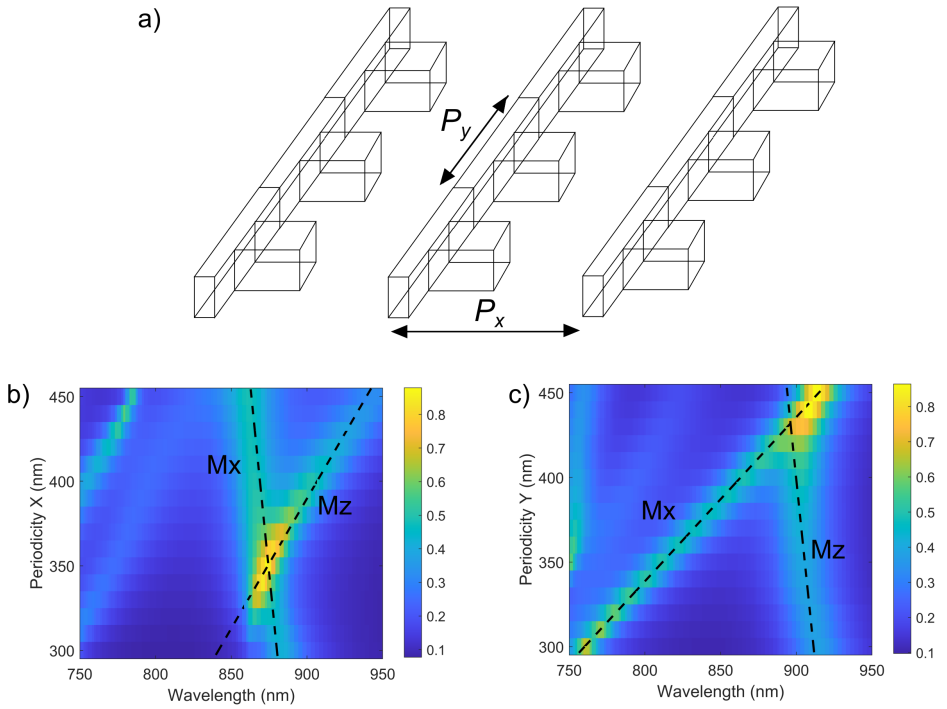

Figure 2.8: Periodicities: a) Schematic of metasurface array. b) Absorption spectra for varying periodicity in x-direction. c) Absorption spectra for varying periodicity in y-direction. Dashed lines demonstrate M_x and M_z modes in the parameter space.

Parameter Change (nm)	Mx Mode Shift (nm)	Mz Mode Shift (nm)
Bar Width	14.59	14.72
Block (x-direction)	1.38	9.45
Block (y-direction)	7.98	14.68
Block (z-direction)	15.41	8.40
Periodicity (x-direction)	10.27	-1.19
Periodicity (y-direction)	-1.10	6.42

Table 2.1: Rates of mode wavelength tuning (in nm) for a 10 nm change in parameter size.

2.3 Recipe for Perfectly Absorbing Metasurfaces

Having understood how each parameter affects the wavelengths of both modes, this information is used to develop an intuitive and prescriptive metasurface design method. This can be done by taking advantage of key design parameters which are easy to modify in the design and fabrication. The method is split into three stages: achieving mode degeneracy, tuning operation wavelength and achieving critical coupling of modes.

2.3.1 Mode Degeneracy

The first step is achieving mode degeneracy. From Figures 2.5, 2.6 and 2.8 it is clear that most parameters tune the modes to different extents, and therefore there are several points of intersection where the modes' paths cross in the parameter space and absorption is enhanced. If we do not set a requirement on the wavelength where the modes are degenerate (as this will be adjusted later), we can achieve the required mode degeneracy simply by selecting the parameters at one of these intersection points. In Chapter 3 it is demonstrated how this can be done experimentally.

2.3.2 Operation Wavelength

In order to then tune the modes to a desired wavelength, we can use the information in Table 1 to decide on appropriate parameters to change. The easiest way to tune modes simultaneously is by scaling the metasurface in all dimensions. However, this is impractical because the metasurface thickness is set during the wafer growth process and scaling in the x-y plane only will lead to loss of mode degeneracy. Instead, it can be seen in Table 1 that the bar width has the largest and most similar effect on both modes. Therefore the operation wavelength of the metasurface can be tuned without loss of degeneracy by adjusting the bar width. Figure 2.9 shows this process - the simulated absorption spectra for different bar widths is shown for a design where the two modes are degenerate. The two modes appear as a single highly absorbing band spanning from 700 - 950 nm. We see the same behaviour if we take into account dispersion in GaAs (Fig. 2.9b), however in this case we also observe a drastic variation in peak absorption as the bar width changes. Perfect absorption is achieved at 800 nm, but quickly drops off toward longer wavelengths. This is because the intrinsic absorption of the material changes with wavelength and therefore the absorption loss of the mode no longer matches radiative losses, and the structure moves away from the critical coupling condition.

2.3.3 Critical Coupling

The dispersive material simulations in Figure 2.9b highlight the fact that mode degeneracy is a necessary, but not sufficient, condition for achieving perfect absorp-

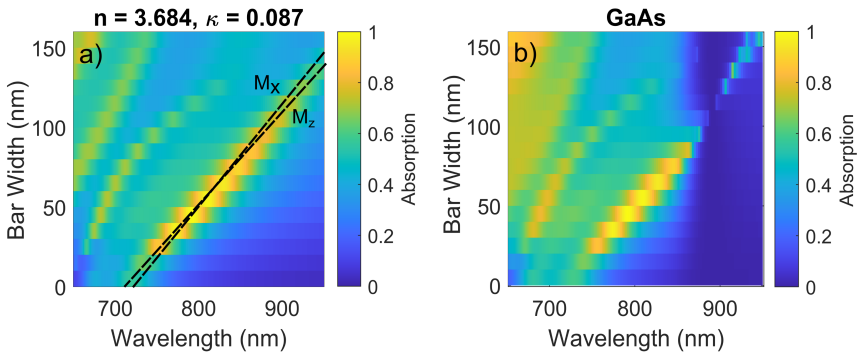

Figure 2.9: Tuning Metasurface Wavelength with Bar Width: Absorption spectra with varying bar width when modes are degenerate. a) Constant n, κ values are used for material properties. b) Dispersive material properties are used (Palik Data [11]).

tion. Once modes are made degenerate and positioned at a desired wavelength (by tuning the bar width), the critical coupling condition must be realised by balancing the radiative and absorption losses of the modes. In order to do this, the periodicity of the structure is tuned in both x and y-directions without adjusting the resonator and bar sizes. It has been demonstrated in many metasurface systems that the periodicity alters the collective behaviour of resonators, including the radiative losses [15, 80–82]. At the same time, for this specific metasurface design, tuning both periodicities has a relatively small effect on the modal wavelengths ($\sim$6% change in wavelength for a 20% change in periodicity size). We can therefore adjust the radiative losses of the modes and achieve critical coupling by tuning the periodicity, without losing mode degeneracy or drastically changing mode wavelengths. Figure 2.10 shows this process for a structure with a 40 nm bar (from Fig. 2.9), where the periodicity is tuned from 340 nm 440 nm. In this range, peak absorption changes by $\sim$20% and reaches a maximum of 99.9% at a periodicity of 395 nm.

To illustrate the impact of material absorption, Figure 2.10b shows how absorption of modes changes with varying intrinsic material absorption. For a set periodicity and metasurface parameters, the peak absorption first rises sharply as the extinction coefficient is varied from 0.001 to 0.05. At $\kappa = 0.08$ the metasurface exhibits perfect absorption. This value of material absorption corresponds to the

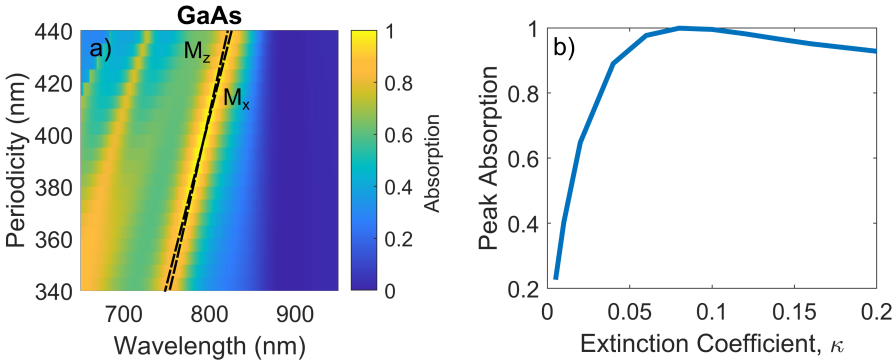

Figure 2.10: Tuning Radiative Losses with Periodicity: a) Absorption spectra for varying Periodicity. Dispersive material model used. b) Change in peak absorption with material extinction coefficient.

critical coupling condition, i.e. the absorption of the modes matches the radiative loss of the modes. If the material absorption is increased beyond this value, the structure moves away from the critically coupled condition and overall absorption of the metasurface decreases despite the increasing κ. A similar process happens when the periodicity is modified in Figure 2.10a, except here the radiative losses are mostly affected rather than the material absorption.

Whilst the bar width enables tuning of the M_x and M_z dipoles together and the periodicity allows us to adjust radiative losses, the modes may drift apart during these steps for large parameter changes. The impact of mode splitting on peak absorption varies with wavelength. In the region where intrinsic absorption is high (800 nm), the mode splitting does not greatly affect peak absorption: we find that $>$90% absorption can be achieved after adjusting the periodicity without further changes. For wavelengths where the intrinsic loss is low, the splitting plays a more significant role. For example, in Figure 2.9b, the modes visibly split into two separate absorption peaks in the region of 950 nm. The difference is due to the linewidths of the modes. If mode splitting occurs, the modes can be re-matched and absorption maximised by a process of local 'particle swarm' numerical optimization of the central block width and height in x and y-directions. The block thickness (z-direction) also affects the mode frequencies, however this parameter is fixed at the wafer growth stage and it is less practical to adjust during the fabrication process.

2.3.4 Demonstration of Perfectly Absorbing Designs

Using the three steps outlined in this section, metasurface designs were developed which achieved perfect absorption at different wavelengths. The optical properties of two of these designs are shown in Figure 2.11. The first design achieves peak absorption at 790 nm, where the photon energy is above the GaAs bandgap, and as a result intrinsic material absorption is relatively high. In contrast, the second design is centred right at the bandgap edge (860 nm), where material absorption approaches zero (see Fig. 2.2). Despite this, we can still obtain perfect absorption at this wavelength by critically coupling the two modes at the same wavelength. The linewidth of the absorption peak in design Figure 2.11b is significantly narrower than the design Figure 2.11a. This is because the linewidth is largely determined by the material absorption at that wavelength - when material absorption is low the linewidth is narrower.

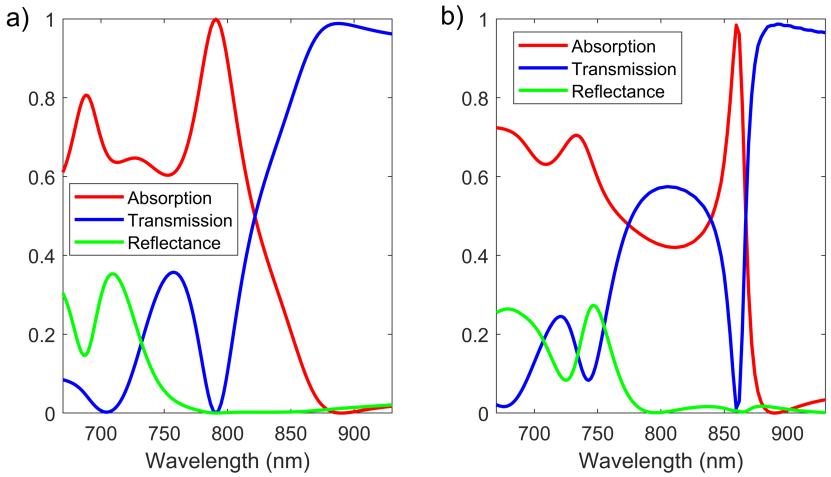

Figure 2.11: Perfectly Absorbing Designs at a) 790 nm (bar width = 40 nm, periodicity = 390 nm) and b) 860 nm (bar width = 80 nm, periodicity = 385 nm). Other parameters the same as Figs. 2.9, 2.10.

2.4 Alternative Perfectly Absorbing Designs

So far in this chapter I have demonstrated the design of one specific perfectly absorbing metasurface based on the degenerate critical coupling of two magnetic dipoles. This design relies on asymmetry in the unit cell in order to excite an out-of-plane magnetic dipole with opposing symmetry to the in-plane magnetic dipole.

However, it is also possible to achieve degenerate critical coupling - and thereby perfect absorption - using two in-plane dipoles if they have inherent opposite symmetries. This is the case if we use a magnetic dipole and the perpendicular electric dipole, e.g. M_x and E_y. Figure 2.12 shows a metasurface design based on exciting these two modes, developed by our group in [83]. In comparison to the structure in the previous section, the vertical bar is positioned in the centre of the unit cell, and the block is extended horizontally across the unit cell. Both M_x and E_y modes are directly excited by the incident field, meaning that no symmetry-breaking is required. In addition, this design has the advantage that neighboring resonators are connected in both in-plane directions, meaning it can be used in applications where photoconductivity is required in more than one direction. Despite the interconnectivity, the mode profiles resemble normal magnetic and electric dipoles excited in a cubic structure (Fig. 2.12c, d). However, the process of interconnecting the metasurface shifts both modes to longer wavelengths. By choosing appropriate size parameters, a design can be found where both modes are degenerate when neighboring resonators are fully connected.

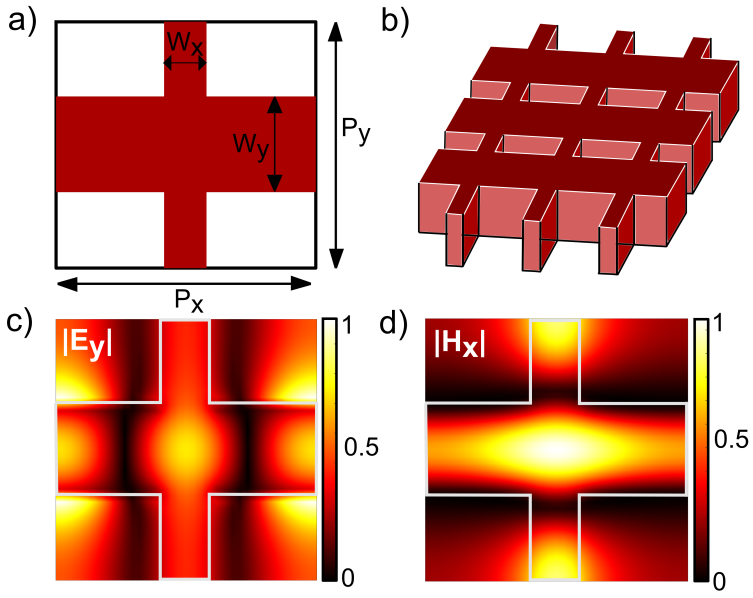

Figure 2.12: Alternative Metasurface Design a) Diagram of unit cell. b) 3D diagram of metasurface array. c) Normalised absolute field profile of Electric Dipole polarised in the y-direction, E_y. d) Normalised absolute field profile of Magnetic Dipole polarised in the x-direction, M_x.

We can use similar methods as those used in Section 2.3 to modify the wavelengths of the modes and their absorption, in order to adapt the design for different operation wavelengths. Specifically, by modifying the array periodicity, the modes can be made degenerate. By varying the width of the horizontal channel (W_y in Fig. 2.12a), modes can be tuned roughly degenerately to a wavelength of choice. Finally, the absorption of the modes can be changed by tuning the width of the narrow channel, W_x. This changes the proportion of the mode interacting with the absorbing material. Therefore, we can understand the tuning of this channel as tuning the absorption loss of each mode, and thereby the critical coupling condition. In [83] several perfectly absorbing designs are shown made from an 160 nm thick GaAs layer, ranging in operation wavelength from 715 nm to 840 nm.

2.5 Summary

In this chapter I have demonstrated the basic principles of high absorption in dielectric metasurfaces via degenerate critical coupling of two modes. I have demonstrated two metasurface designs that achieve perfect absorption using this technique. By revisiting the conditions I outlined at the start of the chapter, one can see that these metasurfaces are highly applicable to THz PCA detectors:

- They achieve full absorption which can be engineered to a NIR wavelength of choice through simple parameter changes.
- Both designs have conductive channels which allow for carrier transport to antennae for detection.
- They are designed for LT-GaAs and can achieve perfect absorption despite strong dispersion across the GaAs bandgap.
- They have extremely sub-wavelength thicknesses (200 nm or less).

In Chapter 3 the fabrication of the metasurfaces is described. The steps described in Section 2.3 are demonstrated experimentally and the designs in Figure 2.11 are realised.

Chapter 3

Metasurface Fabrication & Experimental Testing

Fabrication and optical characterisation measurements shown in this chapter were carried out at the Centre for Integrated Nanotechnologies (CINT), Sandia National Labs, USA by O. Mitrofanov. Metasurface designs were informed by simulations done by L. Hale and T. Siday. Analysis of the optical data was carried out by L Hale. Electronic detector measurements were done at CINT by O. Mitrofanov. Terahertz detection measurements were done by O. Mitrofanov, T. Siday and L. Hale. Some of the contents of this chapter have been published in [67], [84]. Permission for the use of this content has been granted by the publisher where necessary.

In Chapter 2 a three-step process was outlined for designing perfectly absorbing metasurfaces at a desired wavelength. This was used to achieve perfect absorption in regions of the spectrum where GaAs is highly absorbing as well as at the bandgap edge where absorption is low. In this chapter the fabrication of the metasurfaces is described, and the optical characteristics of fabricated metasurfaces are measured – showing that the fabricated metasurfaces have same dependence on the bar width and periodicity as the simulated structures. The simulated designs in Figure 2.11 are fabricated and their optical properties discussed. Finally, the THz detection properties of a metasurface operating at 800 nm are investigated. It is shown that the metasurface has many beneficial properties for THz detection, such as very high dark resistance and high SNR detection with remarkably low optical

pump powers.

3.1 Methods

3.1.1 Metasurface Fabrication

The main stages in the fabrication of the metasurfaces are shown in Figure 3.1. Metasurfaces are fabricated from a 200 nm epilayer of low-temperature grown GaAs on a semi-insulating GaAs substrate. Two thin AlGaAs layers sit between the LT-GaAs and SI-GaAs and act as stop-etch layers later in the fabrication process. Firstly, the LT-GaAs is annealed to improve the dark resistivity of the material. The metasurface is then patterned using electron beam lithography (EBL) and dry reactive ion etching (RIE) is used to etch the 200 nm thick metasurface. If the metasurface is used for THz detection, metallic antennae with tapered ends are deposited on top of the metasurface using EBL and metal evaporation (see Section 3.3 for more details). The metasurfaces are then transferred onto sapphire substrates using epoxy ($n = 1.57$) to bond the metasurface to the substrate. Finally the structures are mechanically lapped on the SI-GaAs side and wet-etched to the stop-etch layers. The final result is a 200 nm thick LT-GaAs metasurface embedded in 2 μm of epoxy on a sapphire substrate, where the epoxy replaces the LT-GaAs that has been etched away. Information about the specific fabrication conditions can be found in Appendix C. Scanning electron microscope (SEM) images of example metasurfaces are shown in Fig. 3.1b, c.

3.1.2 Optical Characterisation

Once the metasurfaces are fabricated, the optical transmission and reflectance of the samples are measured using a confocal microscope set up. White light from an incandescent lamp is focused on the metasurface with a microscope objective to a spot size of $\sim$10 μm. The transmitted beam is collected by another microscope objective and analysed with a diffraction grating spectrometer. Polarisers are used to polarise the light incident on the metasurface and light collected by the objective in the same orientation. Transmission measurements are normalised to the incident light spectrum, taking to account the transmission of the sapphire substrate. Reflec-

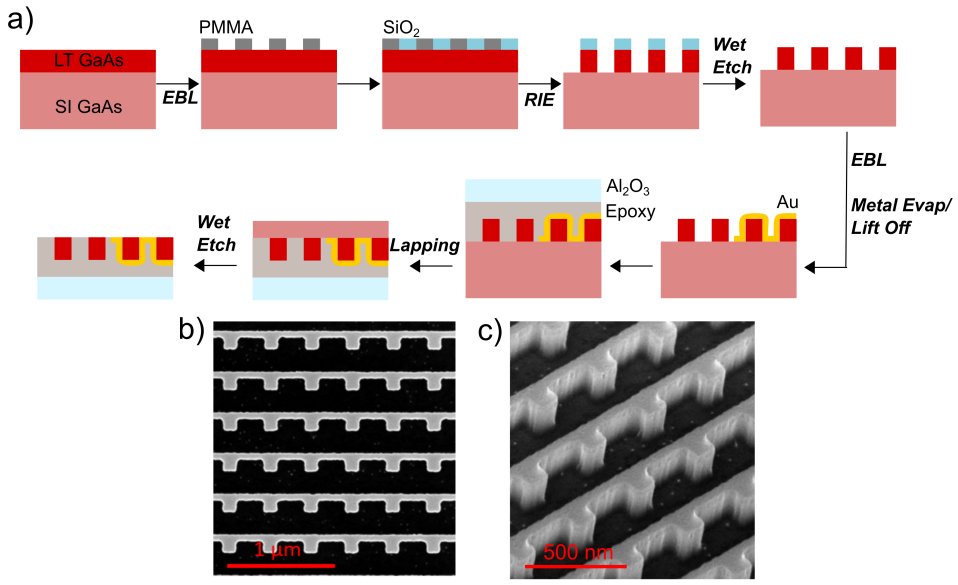

Figure 3.1: Metasurface Fabrication: a) Schematic showing key steps in the metasurface fabrication process. b) SEM image of the metasurface (top view). c) SEM of metasurface taken at oblique angle.

tion measurements are normalised to the spectrum reflected from a reference gold surface, taking into account the gold reflectivity ($\sim 96\%$) within the spectral range of interest. Absorption is then calculated from these normalised transmission and reflectance measurements as $A = 1 - (R + T)$.

3.2 Achieving Perfect Absorption in Fabrication

In order to fabricate fully absorbing metasurfaces at a specific wavelength, a similar process to the design in Chapter 2 (Section 2.3) can be carried out experimentally. Firstly the modes are made degenerate, then they are tuned simultaneously to the chosen wavelength. Finally, high absorption is regained by tuning the radiative losses.

3.2.1 Mode Degeneracy, Wavelength & Absorption

Firstly, a set of metasurface parameters is chosen from simulations which aligns the modes at the same wavelength. However, different fabrication conditions will lead to different parameter sizes from the original design, meaning modes may be misaligned. One important condition is the EBL exposure, which affects the bar

width and size of the central block. These parameters will increase in size for an overexposed structure, leading to a redshift for both modes, which may result in spectral splitting of the modes. This is demonstrated in Figure 3.2, which shows the experimentally measured transmission spectra for four metasurface samples. Each sample is fabricated using the same EBL pattern (chosen from a simulated design where modes are degenerate), but different exposure levels. The position of modes can be identified by dips in the transmission spectrum, where absorption is enhanced. For most exposures two transmission dips can be seen, as the two modes sit at different wavelengths. At a normalised exposure of 1 (purple line) the modes become degenerate, indicated by the fact that both modes appear as a single feature. Therefore, this exposure can be chosen for subsequent fabricated samples of this design, where the bar width and periodicity are modified to change the wavelength and absorption level of the modes.

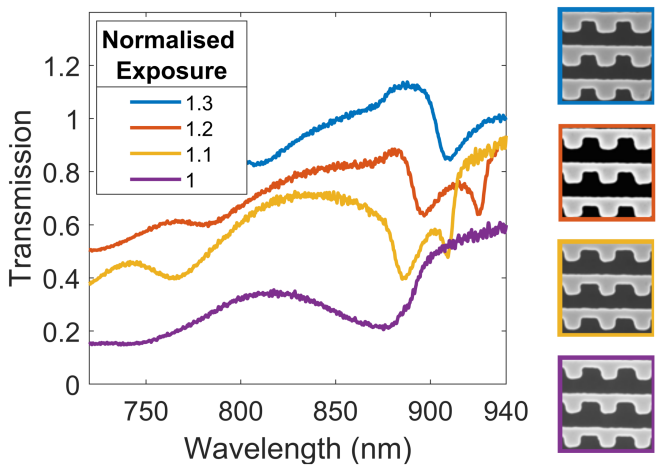

Figure 3.2: Achieving Mode Degeneracy: Transmission of metasurfaces patterned with different EBL exposures, offset from each other for clarity. Panels (right) show SEMs of the corresponding metasurfaces in the graph.

In Section 2.3 it was demonstrated that once modes are degenerate, modifying the bar width allows tuning of the modal wavelengths whilst maintaining degeneracy. Figure 3.3 shows the effect of tuning the bar width experimentally. The measured transmission spectra are shown for a set of metasurfaces with varied bar widths, along with the simulated transmission for structures with similar dimen-

sions to the fabricated structures. For each structure a deep dip in transmission can be seen where the two modes overlap - indicating strongly enhanced absorption. As the bar width is varied the transmission dip shifts in wavelength without splitting into two peaks - demonstrating the ability to tune the two mode wavelengths simultaneously with bar width.

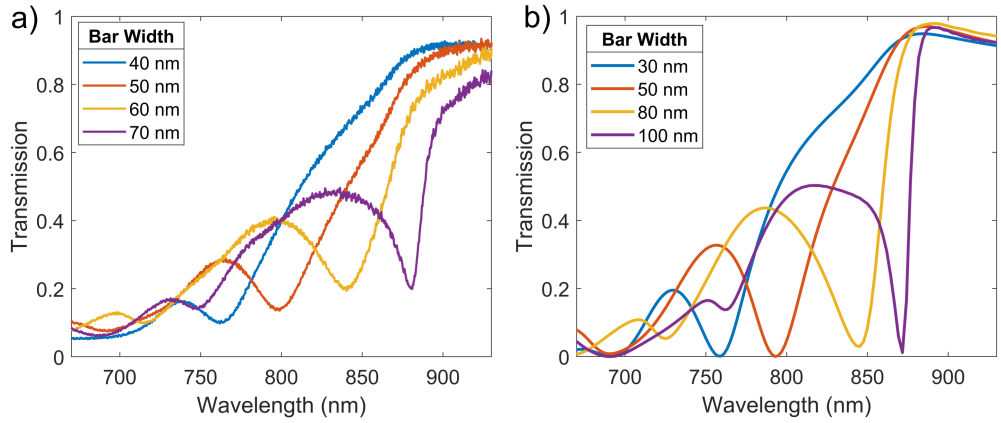

Figure 3.3: Tuning operation wavelength with bar width: a) Measured transmission for metasurfaces with varying bar width. b) Simulated transmission for metasurfaces with different bar widths. Other metasurface parameters are chosen to match those in the fabricated structures.

In Figure 3.3a it is observed that with increasing bar width the minimum transmission increases - indicating a reduction in peak absorption. This is due to the effect of changing the modal wavelengths on the critical coupling of the modes. As the modes shift to higher wavelengths their absorption decreases and the structure moves further away from the critical coupling condition where the mode absorption matches the radiative loss. In the simulation the minimum transmission does not change as drastically with increasing bar width. However, by simulating the reflectance with increasing bar width (Figure 3.4) we see that the reflectance increases for larger bar widths, instead of the transmission. When the structure is close to the critical coupling condition a reflection minimum is seen at the resonance frequency (Fig. 3.4b blue line). However, as the bar width increases this becomes a reflection maximum (Fig. 3.4b purple line). Therefore, in both simulations and experimental data absorption decreases as the structure moves away from the critical coupling condition as the bar width increases.

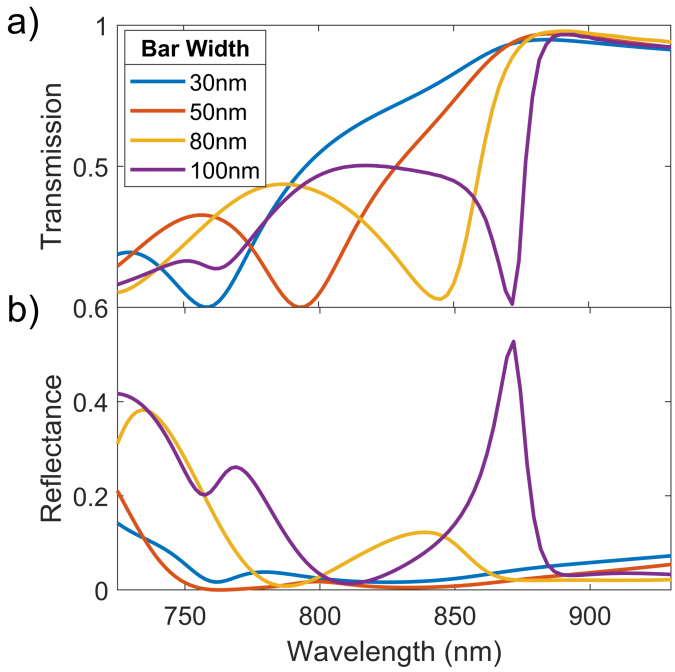

Figure 3.4: Simulated transmission (a) and reflectance (b) for metasurfaces with varying bar width.

It is noted that in addition to the disparity between the minimum transmission, there are other minor differences between the transmission spectra of simulated and fabricated structures. For example, in the simulation the metasurface is almost completely transparent at 890 nm, whereas in the fabricated structures we only measure 80 - 90% transmission in this region. This difference is the result of a standard GaAs model [11] which does not accurately describe the permittivity of LT-GaAs at longer wavelengths. In reality, the presence of As islands and crystal defects results in a non-negligible absorption [85], whereas the modelled material has an imaginary permittivity approaching zero (as shown in Fig. 2.2).

To regain high absorption the periodicity is experimentally varied. Figure 3.5 shows the measured (a) and simulated (b) transmission spectra for three metasurfaces of different periodicities. The minimum transmission decreases with increasing periodicity. This is a consequence of changing the radiative loss of the metasurface with the periodicity - as the period increases the structure moves closer to the critical coupling condition where the radiative loss matches the absorption loss

of each mode. The ability to tune the radiative losses with periodicity in the fabri-

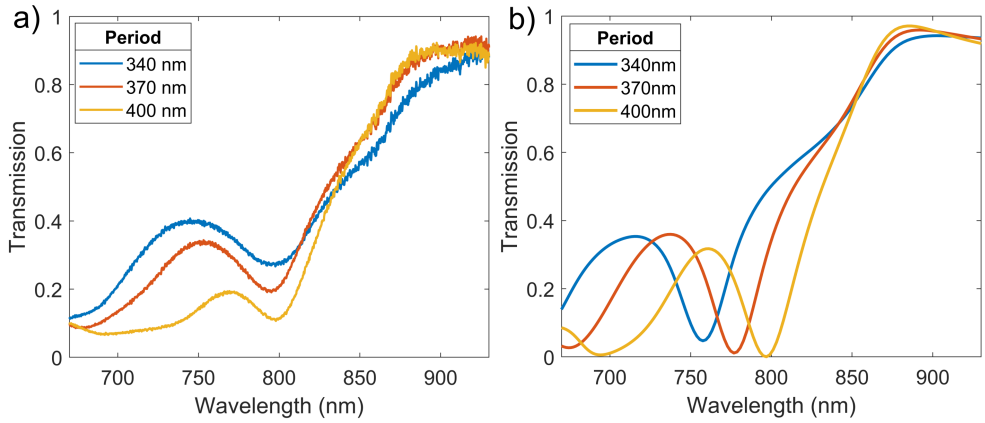

Figure 3.5: Tuning absorption with periodicity: a) Measured transmission for metasurfaces with varying periodicities. b) Simulated transmission for metasurfaces with different periodicities. Other metasurface parameters are chosen to match those in the fabricated structures.

cation process is particularly advantageous when fabricating structures close to the bandgap edge. As previously explained, in this spectral region published models for GaAs imaginary permitivitty may not closely match LT-GaAs due to the presence of defects, making it difficult to find the optimum geometry using simulations. However, varying the periodicity in the fabrication process allows us to optimise the radiative loss and match it to real absorption loss experimentally. This leads to different optimum periodicity in fabricated structures in comparison to simulations.

3.2.2 The Proximity Effect

There are some discrepancies between the simulated and experimental transmission data in Figures 3.3 and 3.5, which can be attributed to inaccuracies in the parameter sizes of fabricated structures as a result of the proximity effect in the EBL stage of fabrication [70].

In Figure 3.3, a smaller range of bar widths is required in the experiment to span the same range of wavelengths as in the simulation. This is due to the fact that as the bar width in the EBL pattern increases, the proximity effect causes an increase in the electron beam spot size, and thereby a superlinear increase in both the bar and block size. This results in a larger overall structure, and the modes are red shifted

to larger wavelengths. Given that the difference in the fabricated structure sizes is on the order of a few nanometres, this is difficult to measure accurately from SEM images. In the simulated structures, however, the bar size is increased in precise increments without affecting other parameter sizes - therefore capturing the true effect of increasing the bar size alone.

In Figure 3.5, we also see that as the periodicity increases, the wavelength of the fabricated structures is unaffected (Fig. 3.5a), whereas an increase in wavelength is seen for simulated structures (Fig. 3.5b). This is also a consequence of the proximity effect. For smaller periodicities, neighboring resonators are closer together, leading to slight overdosing of neighbouring resonators and increase in the resonator size over the whole metasurface area. Therefore, at smaller periodicities the wavelength of the fabricated structures is red shifted in comparison to the simulated design, resulting in all three structures in Fig. 3.5a being resonant at similar wavelengths. In contrast, in the simulations shown in Fig. 3.5b the periodicity changes without affecting the resonator sizes.

3.2.3 Final Fabricated Metasurfaces

Finally, the above process was used to fabricate the two metasurfaces designed in Figure 2.11. Their measured optical properties are shown in Figure 3.6. Absorption is also plotted for each structure. As with the simulated designs, the fabricated structures show enhanced absorption at 790 nm (Fig. 3.6a) and $\sim$870 nm (Fig. 3.6b). For the structure in Figure 3.6a we see a broad absorption peak, whereas in Figure 3.6b the modes are slightly misaligned and the peak is split in two. In this region of the spectrum the lack of strong material absorption causes the modes to become much narrower and therefore more sensitive to mode misalignment. In principle, similarly to the step described in Section 2.3, small adjustments of the central block size can be performed in fabrication in order to align the two modes.

I also show an experimentally measured absorption spectrum for an unpatterned (uniform) 200 nm thick LT-GaAs layer (black line). In comparison to this, the metasurfaces show a resonant absorption enhancement of 3-fold for the 790 nm structure and over 15-fold for the 875 nm structure. It is particularly notable that

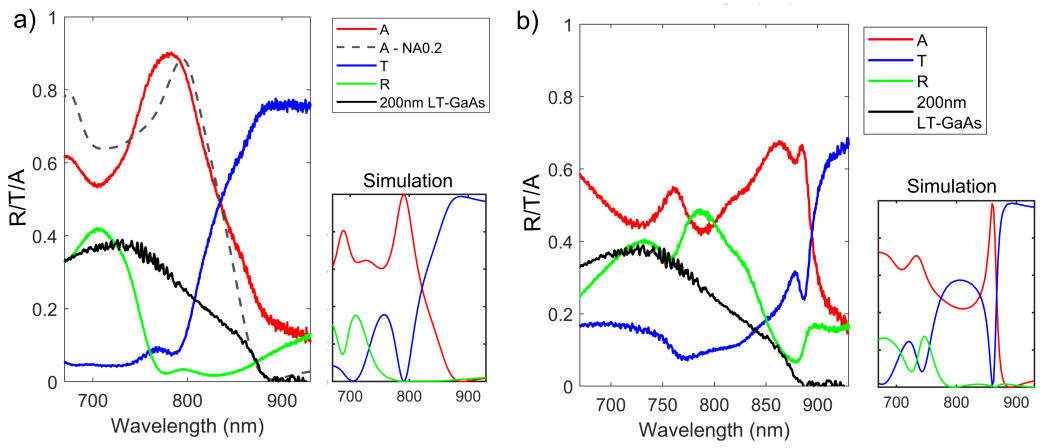

Figure 3.6: Measured optical properties of fabricated structures (based off designs in Fig. 2.11, Chapter 2). Black line shows the absorption measured from unpatterned LT-GaAs of the same thickness as the metasurface. Grey dashed line (a) shows absorption simulated for the metasurface with a Gaussian excitation beam (NA = 0.2). Insets show simulated optical properties for designs corresponding to each fabricated metasurface.

absorption in unpatterned LT-GaAs approaches zero around 875 nm, whereas for the structure in Fig. 3.6b ∼70% of incident light is absorbed.

The peak absorption levels in both fabricated metasurfaces are not as high as predicted in the simulations. For example, for the structure in Figure 3.6a only ∼90% absorption is achieved. This is due to the fact that the experimental spectra were measured using a focused optical beam with numerical aperture of NA ≈ 0.16, rather than the perfect plane wave used in simulations. In a focused beam not all field components are polarized in the direction required for exciting the two modes, leading to a broadening of the absorption peak and reduction in peak absorption. In order to quantify the effect of this on the results, a full 15 x 15 metasurface array was simulated with a gaussian beam for excitation, which had a similar numerical aperture (NA = 0.2) to that used in the experiment (see Appendix B for details). In this case, it was found that the peak broadens and maximum absorption decreases by ∼10%. The simulated absorption in this case is plotted for the metasurface in Fig. 3.6a (gray dashed line) – a good agreement can be seen between the simulated and experimental absorption spectra.

3.2.4 Summary of Optical Measurements

This section has shown that the prescriptive methods described in Chapter 2 for designing perfectly absorbing metasurfaces at a chosen wavelength can also be used in the fabrication process. Degeneracy is achieved by tuning EBL exposure, operation wavelength is selected by tuning the bar width, and high absorption is gained by tuning the metasurface periodicity. In particular, tuning the periodicity experimentally enables tuning of critical coupling even when the intrinsic material absorption is not directly known (as for low-temperature materials) and therefore cannot be accurately simulated. Highly absorbing metasurfaces are fabricated at a range of wavelengths corresponding to different levels of intrinsic GaAs absorption. Over 90% absorption was achieved for a metasurface operating at 790 nm and $\sim$70% absorption for a metasurface at 875 nm, very close to the bandgap edge. Despite some mode splitting, this is a 15-fold improvement on the absorption of bare LT-GaAs of the same thickness. These metasurface designs can be readily implemented in THz detectors operating at a range of NIR pump wavelengths.

3.3 Terahertz Detection Properties

Following the investigation of optical characteristics, one metasurface was also used as the photoconductive element in a THz detector. This section describes the electronic and THz characteristics of the metasurface and demonstrates that the metasurface exhibits many beneficial properties for THz detection. The effect of a highly absorbing metasurface on the spectral bandwidth of the detector is also investigated.

3.3.1 Detector Fabrication

A perfectly absorbing metasurface operating at 800 nm was designed and fabricated for use as a THz detector in order to match the wavelength of a Ti:Sapphire laser used in the TDS system in the lab at UCL. The metasurface dimensions and simulated optical properties can be seen in Figures 3.7c and 3.7d. As with the metasurfaces in Chapter 2, the photoconductive metasurface layer is 200 nm thick. This is remarkably thin in comparison to normal PCA detectors, which are limited in how thin they can be made by the absorption length in GaAs and therefore typically

have photoconductive regions of 1-2 µm [39].

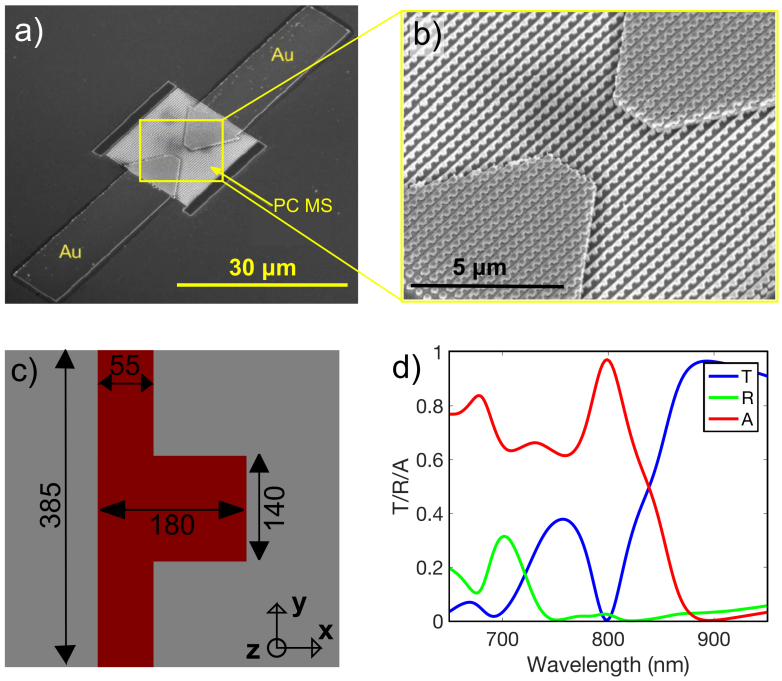

Figure 3.7: Perfectly Absorbing Metasurface as Terahertz Detector: a) SEM of metasurface including metallic antennae. b) Close up SEM of photoexcitation region. c) Unit cell diagram showing metasurface dimensions in nm. d) Simulated optical characteristics of metasurface.

In order to give the metasurface THz detecting capabilities, metallic dipole antennae with tapered ends were deposited onto the metasurface after the metasurface etch using EBL and metal evaporation techniques. This was done before the metasurface was glued to the sapphire substrate (see Figure. 3.1). The antennae are centered on the middle of the metasurface, with a 3 µm gap between them where the metasurface is photoexcited. Figures 3.7a and 3.7b show an SEM of a metasurface with antennae.

3.3.2 Electronic Measurements

A semiconductor parameter analyser was used to measure the IV characteristics of the device in a dark chamber, and thereby deduce its dark resistance. A bias from 0 - 50 mV was applied across the antennae in steps of 0.01 mV. Linear IV characteristics were observed and the dark resistance was found from the gradient to be 50 GΩ. This value is remarkably high in comparison to PCAs based on unstructured

GaAs layers (typically $\sim$1GΩ), owing to the fact that there is much less absorbing material in a metasurface than a bulk GaAs layer. As a result of this large dark resistance, high switching (ON/OFF) contrast of $\sim 10^7$ is measured, which is beneficial for high SNR, particularly at low optical pump powers.

3.3.3 Terahertz Measurements

The detector was used in a standard TDS system in order to measure its THz detection ability. The experimental set up can be seen in Figure 3.8c. A femtosecond pulsed Ti:Sapphire laser centered at 800 nm with 80 MHz repetition rate was used to excite both the detector and a zinc telluride (ZnTe) crystal which was used as a THz source. A silicon lens was attached to the ZnTe crystal to improve the THz directionality. The NIR beam (and thereby the THz beam) were polarized in the direction of the dipole antenna (horizontally) - allowing excitation of both dipole modes in the metasurface. An optical chopper was used to intensity modulate the THz beam at 2.7 kHz, and the photocurrent from the THz detector was measured with a lock-in amplifier with an integration time of 300 ms.

An example THz waveform measured from the ZnTe source can be seen in Fig. 3.8a. By varying the power of the NIR pulse gating the detector, the dependence of the peak photocurrent and noise on the gating pulse power was investigated (Fig. 3.8b). The gating power was varied from 50 – 750 μW using a polariser in the probe beam path. The root mean square (RMS) noise was calculated over 200 data points before the THz pulse and was seen to increase roughly linearly for higher excitation powers. It is therefore likely that the main source of noise is fluctuations in laser power, which increase linearly with pump power.

Figure 3.9 shows the SNR calculated as the square of the ratio of maximum signal to RMS noise. Maximum SNR of almost 10^8 is achieved at 100 μW. To provide context, this is compared against a previous detector developed by our group in ref. [12]. For the detectors here, maximum SNR is reached at a power level approximately an order of magnitude lower than in [12]. This improvement can be attributed to two key factors: firstly, much higher absorption results in drastically improved conversion of photons in the gating pulse to charge carriers; and

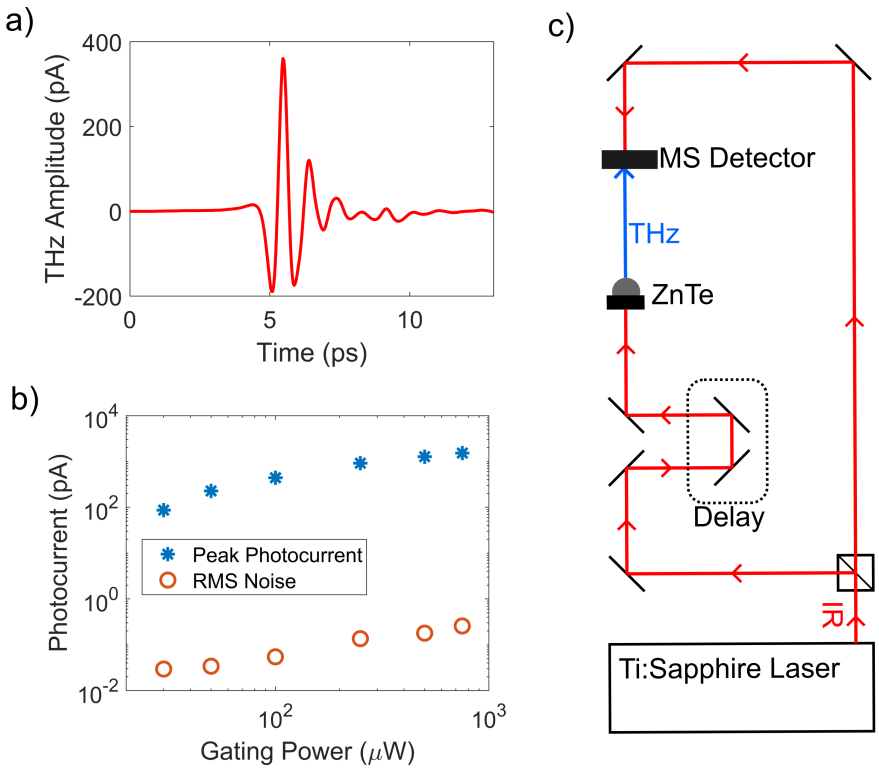

Figure 3.8: THz Detector Measurements: a) Example waveform measured with the metasurface detector from a ZnTe crystal. b) Maximum photocurrent and root mean square (RMS) noise measured for different powers of the near-infrared pump beam. c) Schematic of the TDS set-up used for the measurements shown in (a) and (b).

secondly, the reduced volume of the metasurface photoconductive layer increases the dark resistance, reducing the detector noise [39].

3.3.3.1 Terahertz Detection Bandwidth

Figure 3.10 shows the power spectrum of detector as calculated by Fourier transforming the time domain pulse. The detector shows a typical PCA response, with an operational frequency range of approximately 0.2 - 3 THz.

It is possible that using the perfect absorption mechanism has a detrimental effect on the detection bandwidth. When the modes are excited within the photoconductive layer, the field oscillates within the material before being absorbed. To demonstrate how this could affect the detection bandwidth, the frequency re-

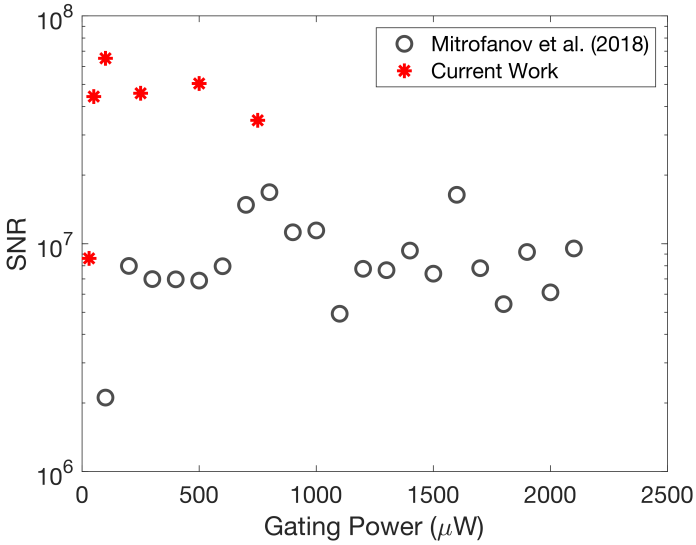

Figure 3.9: Signal-to-noise (SNR) of the metasurface detector, compared to the SNR of the detector used in ref. [12]. Both calculated as $(\frac{Photocurrent_{peak}}{Noise_{RMS}})^2$.

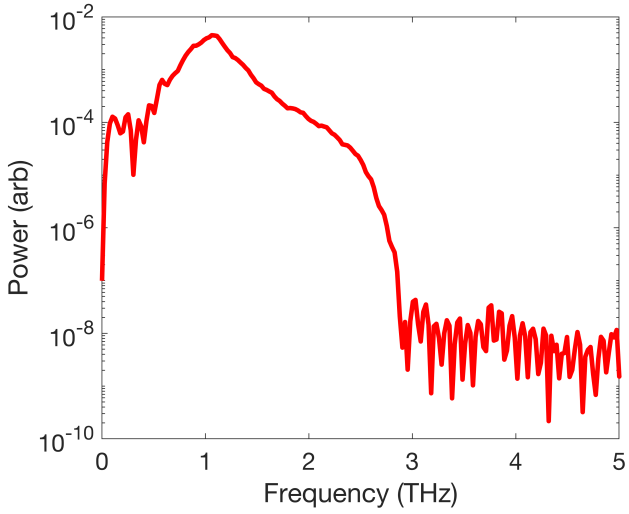

Figure 3.10: Power spectrum of the metasurface detector.

sponse of the detector is considered as the Fourier transform of the measured photocurrent [84]. The measured photocurrent can be written as the integral of the time-dependant bias induced by the THz field, $V_{THz}(t)$ and photo-generated charge carrier density, n:

$$i(\tau) = A\int_{-\infty}^{\infty} V_{THz}(t)\cdot n(t-\tau)dt \tag{3.1}$$

Where A is a constant and τ represents the time delay between the arrival of the

THz pulse and the optical gating pulse. The frequency response is therefore given by the Fourier transform of this quantity:

$$F\{i(\tau)\} = A \cdot F\{V_{THz}(t)\} \cdot F\{n(-t)\} \tag{3.2}$$

Given that the charge carrier density is a function of the field intensity inside the material as a function of time, $I(t)$, and the carrier recombination over time, $r(t)$, Equation 3.2 can be written as:

$$F\{i(\tau)\} = AB \cdot F\{V_{THz}(t)\} \cdot F\{I(-t)\} \cdot F\{r(-t)\} \tag{3.3}$$

As a result, the frequency response is affected by the both the optical field intensity inside the material and the carrier recombination time in the material.

The optical field intensity corresponding to each mode will differ depending on the Q-factor of the mode. We can understand the effect of each mode on the bandwidth by measuring the power spectrum when the metasurface is excited by light in two different excitation polarisations. When the metasurface is excited in the y-polarisation (Fig. 3.7c), both modes are excited by the incident beam. However, when excited by light polarised in the x-direction, only one in-plane mode, M_y, is directly excited. Given that the structure is not symmetrical in the x-y plane, this will be excited at a different wavelength to the M_x mode. Using these two polarisations, we can compare the bandwidth when both in-plane and out-of-plane dipoles are excited to the bandwidth when only an in-plane dipole is excited. This is demonstrated in Figure 3.11a. Figure 3.11b shows the calculated power spectrum ratio of the two polarisations, P_y/P_x, for two different THz sources. For both sources, at lower frequencies the spectral power is larger for the y-polarised case (when both modes are excited). However, at higher frequencies the P_x becomes larger than P_y. This effect can be attributed to the excitation of the out-of-plane M_z mode, which has a longer lifetime. Exciting both modes simultaneously increases the absorption and therefore improves the detector performance at lower frequencies, however at larger frequencies the longer lifetime of the M_z mode degrades the bandwidth, and

so the device performs better when excited in the horizontal polarisation. Whilst this makes a measurable difference to the power spectrum, it can be seen from Fig. 3.11a that the effect is minimal. Given that the difference in absorption between the two excitation polarisations is around 40%, one would expect a larger enhancement in the power spectrum at lower frequencies [84]. The fact that this is not seen is most likely due to the use of a focused gaussian beam. As discussed for the results in Figure 3.6, not all field components in the gaussian beam are polarised in the same direction. As a result, when excited with the x-polarised beam, the M_z dipole will still partially be excited and the difference between the two polarisation cases will be minimal.

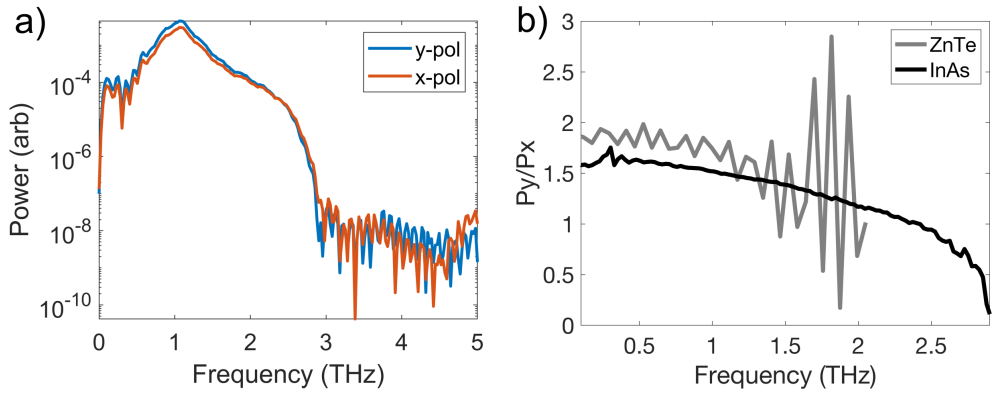

Figure 3.11: Effect of mode lifetimes on spectral response: a) Power spectrum measured for two different excitation beam polarisations. b) Ratio of the power spectrums measured in the y and x-polarisations, measured from both ZnTe and InAs sources.

3.4 Summary

This section has demonstrated the THz detection properties of the perfectly absorbing metasurface PCA. The fact that high absorption is achieved in such a thin photoconductive layer (200 nm) is particularly beneficial for near-field applications in which the sensitivity of the detector is dependent on the distance from the aperture plane to the detecting antennae (as discussed in Section 1.3.3). The highly absorbing nature of the metasurface also results in extremely efficient use of the NIR gating pulse to generate photocarriers, resulting in a maximum SNR ($\sim 10^8$)

at remarkably low gating powers (100 μW). As well as improving the energy efficiency of the device, this is also attractive for near-field applications, in which it is necessary to avoid heating around the sample space. The perfectly absorbing mechanism has some slight drawbacks relating to the frequency response of the detector, however in practice the effect of this is minimal. Finally, the metasurface has a very high dark resistance (50 GΩ) due to the small amount of photoconducting material required for high absorption in comparison to bulk LT-GaAs. This leads to a very high contrast between conductive and non-conductive states of 10^7.

Chapter 4

Metasurfaces for Terahertz Emission

All simulations and metasurface design shown in this chapter were carried out by L. Hale. Fabrication and optical characterisation measurements shown in this chapter were carried out in the Centre for Integrated Nanotechnologies (CINT), Sandia National Labs, USA, by O. Mitrofanov.

In Chapter 2 I demonstrated two different metasurface designs that achieve perfect absorption when illuminated with linearly polarised light perpendicular to the metasurface plane. These were designed for use in THz photoconductive detectors, and Chapter 3 demonstrated how the metasurface can be used in a PCA detector to improve device efficiency. In addition to THz detection, photoconductive metasurfaces could also replace bulk semiconductor elements in other applications. One example is direct THz emission from photoconductive materials via photoexcited charge carrier transients. This is when a semiconductor material such as GaAs or InAs is excited by pulsed NIR light and broadband THz pulses are generated as a result. Unlike in PCA emitters, no external bias is applied in this configuration. Whilst the dominant mechanism of this emission is debated (see Section 4.1), generally THz emission is most efficient when the material is excited by light at an angle to the metasurface plane [86, 87]. In this chapter I investigate if perfect absorption can be achieved in our metasurfaces when excited at an angle, with the view to using perfectly absorbing metasurfaces as THz emitters.

4.1 Emission Mechanisms

In order to understand the benefits of using a metasurface for THz emission, it is necessary to briefly explain how the emission occurs in semiconductors. It is broadly described as being due to photocurrent transients that are generated when incident light excites charge carriers in the material. This photocurrent can be caused by built-in electric field gradients at the surface of a semiconductor (due to Fermi-level pinning) [86] or by what is most commonly known as the photo-Dember effect [88–90] - when electrons and holes diffuse at different rates due to their different mobilities, resulting in an asymmetric charge density distribution. Traditionally, both of these effects are thought to mainly occur perpendicular to the material plane. However, several studies now suggest that lateral (in-plane) photo-Dember effects can play a significant, if not dominant, role in THz emission [91–93].

Regardless of the specific photocurrent transients present, one can see that THz emission will be enhanced if optical photon-to-charge carrier conversion is maximised. This is possible using a metasurface that fully absorbs incident light. In addition, the fact that the metasurface is ultra-thin (100 - 200 nm) means that THz emitters could be easily integrated into current microscale optoelectronics where bulk semiconductors are too large. Finally, comparing THz emission from a metasurface to emission from bulk materials could shed light on the emission mechanism itself. Due to the small thickness of the metasurface, contributions from the surface built-in field on each side should cancel each other out, meaning the two effects could be separated and studied independently. For maximum out-coupling of emission, the semiconductor surface is typically oriented at an angle ($\sim$45°) to the optical axis. In the following sections I explore whether our metasurface designs can efficiently absorb light in this orientation.

4.2 Metasurfaces for Angular Excitation

In order to test the suitability of the initial metasurface design in Chapter 2 for THz emission, a metasurface design with degenerate modes when excited at normal inci-

dence and with E-field polarisation along the vertical bar was simulated at multiple incident beam angles with respect to the metasurface plane (Fig. 4.1a). The simulation region was set up in a similar way to the simulations shown in Chapter 2, however different boundary conditions were used to account for the angled source (see Appendix B for more detail). The goal of this simulation was to observe how the modes move in wavelength space as the incident angle increases. Firstly, the metasurface was simulated using the dispersive GaAs model (Fig. 4.1b). However, given the broad nature of the modes, it was difficult to discern the movement of individual modes in this way. Alternatively, the metasurface was simulated with constant n, κ values ($n = 3.67, \kappa = 0.01$) to decrease mode linewidth and more clearly observe the individual modes (Fig. 4.1c).

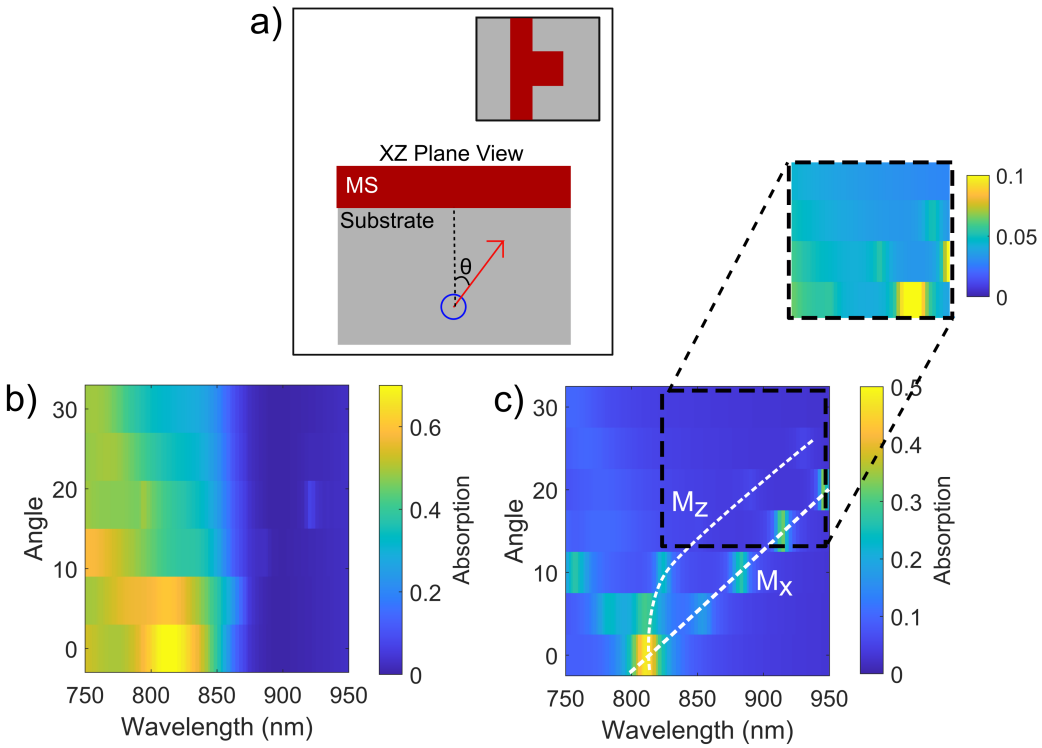

Figure 4.1: Angled Simulations of Bar and Block Structure: a) Schematic of simulation set-up and unit cell. Red arrow shows direction of k-vector whereas blue circle indicates E-field polarisation (out of plane). b) Absorption spectra simulated for a range of angles using a dispersive GaAs model. c) Absorption spectra simulated for a range of angles using low loss, constant material parameters ($n = 3.67$, $\kappa = 0.01$). Inset shows area of plot in dashed square with enhanced colour scale to show the weakly absorbing M_z mode.

From Figure 4.1c it is clear that as the incident angle increases, the modes contributing to absorption at 810 nm at 0° move apart and other higher order modes appear in the spectrum. The M_x dipole remains absorbing as the angle increases and shifts to longer wavelengths. The absorption due to the M_z dipole, on the other hand, appears to rapidly reduce as the angle is increased. For angles greater than 10°, very little absorption can be seen for the M_z mode. Typical angles used for THz emission are approximately 40 - 50°, which correspond to an incident source angle of ∼28° in the simulation as the source is launched in the substrate and therefore refraction at the substrate surface must be accounted for (see Appendix B). Further investigation is required to understand the disappearance of this mode at angled illumination, however this clearly poses problems with using this metasurface design for angled excitation.

Alternatively, the metasurface design described in Section 2.4 was investigated in order to determine if the same effect is seen for a metasurface design based on two in-plane dipoles (M_x and E_y). This metasurface also has the added benefit of connection in both x and y-directions, meaning the metasurface could be designed for emission in two different orientations. To understand the mode behavior at an angle, a metasurface design that is perfectly absorbing at 775 nm was used as a starting point, as its operation wavelength is close to the wavelength of the Ti:Sapphire laser (800 nm) that will be used in emission experiments. The geometry of this design and its optical properties under perpendicular illumination can be seen in Figure 4.2a.

The angle of incidence is varied along the horizontal axis (Fig. 4.2a inset) with the intention of producing lateral photocurrents along the wider, horizontal bar. Figure 4.2b shows the simulated absorption in this case. A highly absorbing region can be seen at 750 nm – 800 nm, which remains at a similar wavelength for increasing angle. In addition, lower absorption bands can be seen at higher and lower wavelengths, which appear only to be present at non-zero incident angles. While some features such as these can be easily seen, it is difficult to see the distinct absorption spectra of each mode.

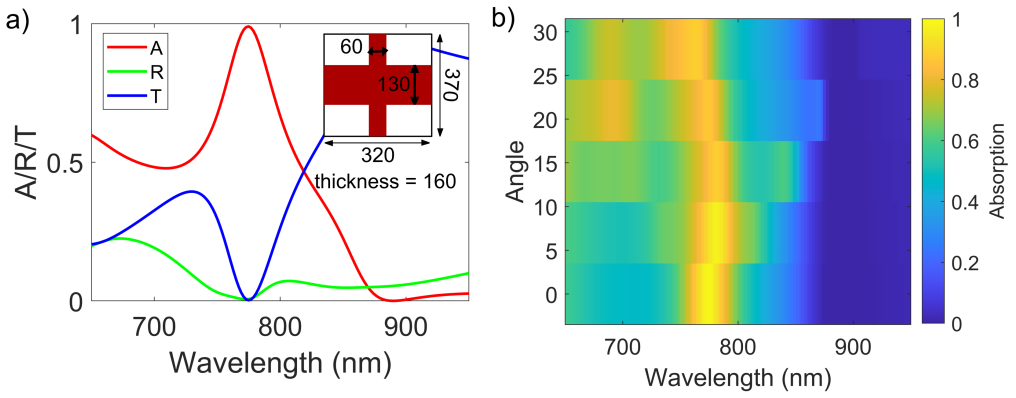

Figure 4.2: a) Absorption (A), reflectance (R) and transmission (T) spectra of perfectly absorbing design under perpendicular illumination (dimensions in nm shown in inset figure). b) Absorption spectra of design shown in (a) for varied incident angle.

To identify which modes these absorption bands corresponds to, the electric and magnetic field intensities in each polarisation can be used to track the modes across the wavelength space. Assuming the modes have maximum field intensity in the centre of the unit cell, the modes can be identified by plotting the field intensity in the appropriate polarisation at the centre of the unit cell for each wavelength and angle. This is shown in Figure 4.3 for magnetic fields polarised in the x and z-directions (Fig. 4.3a, b) and electric field polarised in the y-direction (Fig. 4.3c).

The x-polarised magnetic field in Figure 4.3a clearly contributes to the broad absorption band in the centre of Figure 4.2b. By observing the magnetic field profile in this band (at the position of the white circle in Figure 4.3a), the M_x mode is identified (Fig. 4.3d). This mode is present at normal incidence and is one of the two modes contributing to degenerate critical coupling.

In addition to the x-polarised magnetic field, we also see strong magnetic field in the z-direction. One intensity band shifts from approximately 800 nm to 900 nm as the angle increases. This mode can be identified as the out-of-plane M_z dipole by observing the field profiles at these wavelengths (Fig. 4.3e). This mode cannot be directly excited at normal incidence so no field is observed in the centre at 0°; however, it is excited at non-zero source angles.

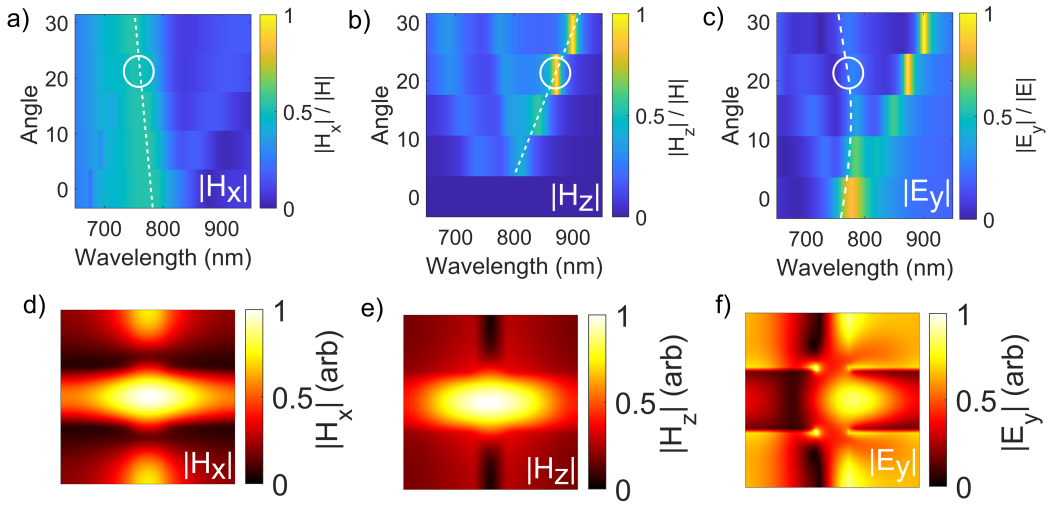

Figure 4.3: Identifying modes for angled excitation: a) absolute magnetic field polarised in x-direction, b) absolute magnetic field polarised in z-direction and c) absolute electric field polarised in the y-direction in the centre of the unit cell are plotted across the spectrum for each angle. All are normalised to the field magnitude at the centre of the x-y plane. Dotted white lines show the high field associated with the a) M_x mode, b) M_z mode, c) E_y mode. White circles show the point at which the corresponding field profiles in d) e) and f) are extracted.

Finally, we observe the electric field intensity in the y-direction (Fig. 4.3c). We see the highest field intensity at exactly the same wavelengths as for the out-of-plane magnetic field. Having identified this as the M_z mode, we can deduce that the electric field in y-polarisation here corresponds to the circulating electric field associated with the M_z mode, which sits in the x-y plane (see discussions in Section 2.2). In addition, we see two bands of significant field intensity at lower wavelengths, which decrease with wavelength as the angle increases. Out-of-plane polarised magnetic field intensity is also present at these wavelengths. Looking at the electric field profiles in the area indicated in Fig. 4.3c (white circle), the middle band (750 – 800 nm) appears to be the E_y mode (Fig. 4.3f). It is slightly off-centre due to the angled excitation, which partly accounts for why only moderate field intensity is seen in Fig. 4.3c. The lower wavelength band (700 – 750 nm) is identified as a higher order M_z mode (not shown). We can therefore conclude that the highly absorbing absorption band in Figure 4.2b contains a combination of the M_x and E_y modes, and that the M_x mode sits at a slightly lower wavelength for

angles 20 – 30°.

Once the separate modes were identified, I investigated how to regain perfect absorption at a fixed angle of 28° (corresponding to incident angle on a glass substrate of 45°) at approximately 800 nm. Only two degenerate modes are required for perfect absorption. Given that the M_z is at significantly higher wavelengths, the original two modes – E_y and M_x - were chosen to use. Remarkably, near-perfect absorption can be achieved for this design at 28° by changing only a single parameter – the periodicity in the y-direction (Figure 4.4). Increasing the periodicity in the y-direction increases the wavelength of both E_y and M_x modes, but has a larger effect on the M_x mode. Because the M_x mode sits at a lower wavelength to the E_y mode initially, increasing the periodicity in the y-direction merges the modes and near-full absorption is achieved at a periodicity of 440 nm. Figure 4.5 shows the optical properties of this design along with the field profiles of the M_x and E_y modes at peak absorption. At lower wavelengths, a complex absorption, transmission and reflectance spectra indicate that several higher order modes overlap in this region. The sharp peak in reflectance and dip in transmission at ∼900 nm corresponds to the M_z mode, which has very low absorption due to the low extinction coefficient of GaAs in this area of the spectrum.

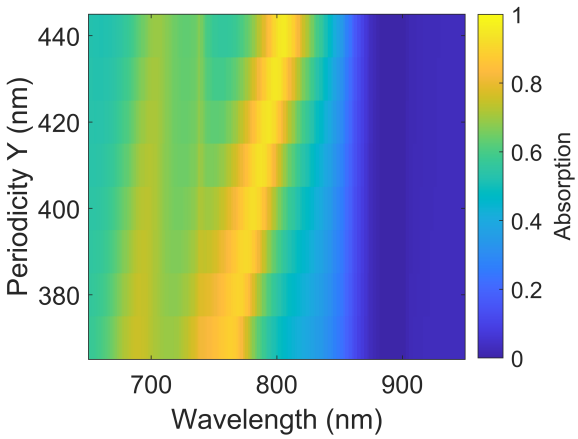

Figure 4.4: Absorption spectra for increasing periodicity in the y-direction. Incident angle is fixed at 28° for all periodicities.

For practical use, it is important that both the peak absorption and absorption wavelength are not highly sensitive to the metasurface angle, as it may not be

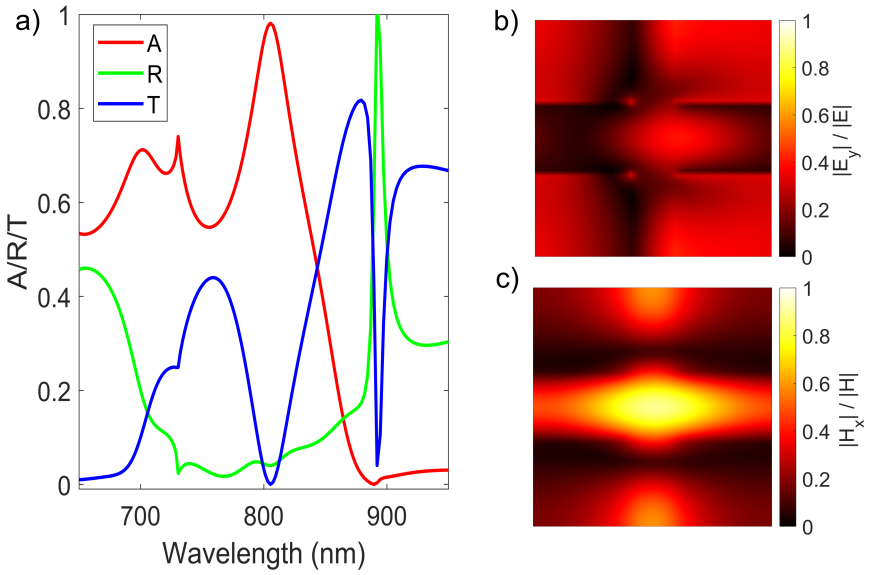

Figure 4.5: Perfectly Absorbing Design at 28°: a) Simulated absorption, reflectance and transmission spectra of design. b) and c) show field profiles at peak absorption wavelength of the E_y dipole and M_x dipole respectively, normalised to electric and magnetic field magnitude.

possible to position the metasurface at the precise angle used in simulations. Furthermore, if a transparent substrate is used with a slightly different refractive index to $n = 1.5$, such as sapphire ($n = 1.76$), it is important that the metasurface still displays high absorption. To investigate this the metasurface was simulated with constant structure parameters, and the source incidence angle was again varied up to 30° (Fig. 4.6). This angle range translates to incident angles up to 51° when taking into account refraction in the substrate. Surprisingly, the modes remain overlapping and very high absorption ($> 90\%$) is maintained over a range of angles from 15 - 30°. Even when modes finally diverge, high absorption of around 70% is maintained for each mode. This robustness suggests metasurfaces may efficiently emit THz radiation at a large range of incident angles. It is also worth emphasising that the metasurface thickness has not been changed from the initial design - it is only 160 nm, making it appropriate for use in many different experimental set-ups. The final design also does not have particularly large variation in parameter sizes, with the smallest parameter being 60 nm. This suggests it can be fabricated reasonably

easily with electron beam lithography.

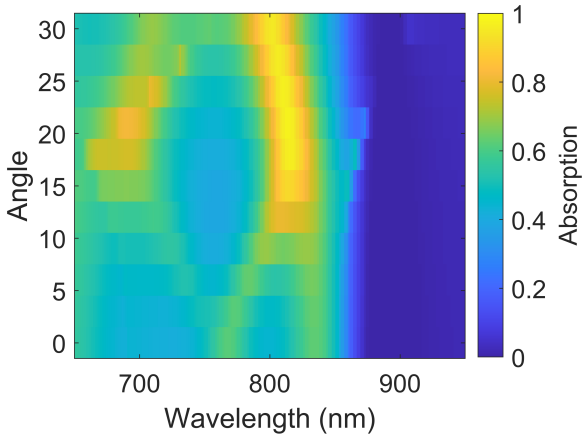

Figure 4.6: Angle dependence of final angled design: absorption spectra of design in Figure 4.5 for varying incident angle.

4.3 Fabricated Designs

Metasurfaces based on the design in Figure 4.5 were fabricated on a sapphire substrate using the same methods as those outlined in Section 3.1.1. The transmission of the fabricated metasurfaces was measured using the confocal microscope as described in Section 3.1.2, except that the angle of the metasurface with respect to the incident beam was varied. Figure 4.7 shows some preliminary results for metasurfaces angled at 45°. Metasurfaces of slightly different geometries were fabricated by varying the EBL exposure and vertical bar width in the EBL pattern. For all metasurfaces in Fig. 4.7 three separate modes are seen: one at ∼800 nm, one at ∼860 nm, and one that is just visible at the edge of the spectrometer range - around 930 nm. The effects of increasing the exposure and vertical bar width are similar: both shift all modes to higher wavelengths.

From simulations in the previous section we can assume that the three modes observed are the E_y, M_x and M_z dipoles; however, these transmission measurements alone do not give us insight into which mode is which. Identifying the modes is necessary in order to decide how to modify the fabrication procedure to make the modes degenerate and increase metasurface absorption (thereby reducing transmission). To identify the modes, the angle of incidence in the transmission mea-

surements was varied from 0° to 45°, and the wavelength shift of the modes with incident angle is compared to simulated transmission data in Figure 4.8. Note that the simulated angle accounts for refraction in the substrate, and therefore both plots show absorption when the incident angle in air ranges from 0° to 45°. The experimental and simulated data have many similarities. In particular, very similar behavior can be seen for the higher wavelength mode, which appears only at larger incident angles and moves linearly with angle increase. From field intensity and mode profiles in the previous section, this mode was identified as the M_z dipole. The two lower wavelength modes must therefore be the E_y and M_x dipoles. From the simulation it can be seen that the E_y dipole wavelength changes more rapidly with angle. For this mode, the relationship between the angle and wavelength is very non-linear - its movement traces a curved line across the absorption spectra. In contrast, the M_x dipole decreases relatively linearly with angle increase. From these observations we can deduce that the mode at ∼770 nm at 45° in Figure 4.8a is the M_x mode, and the mode at ∼850 nm is the E_y mode. In comparison to the simulations, the modes intersect at a smaller angle (10°). Minimum transmission of ∼0.1 is observed here, indicating maximum absorption when the modes are degenerate.

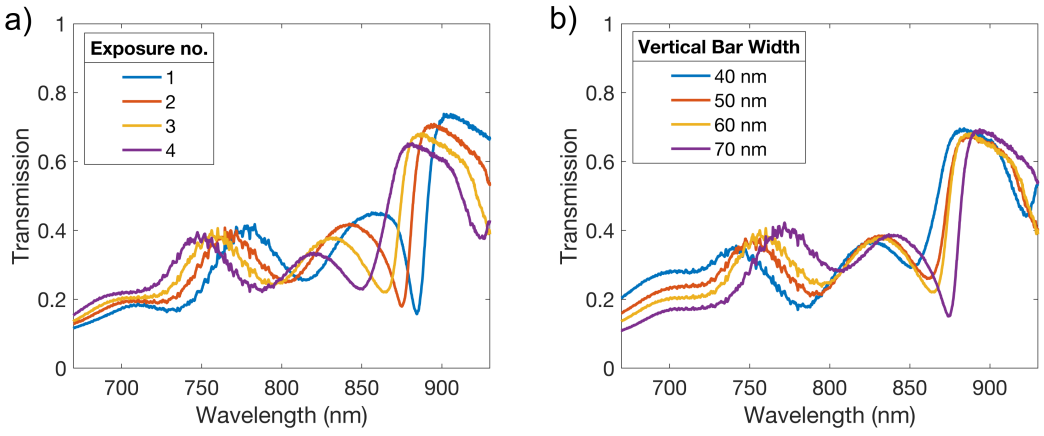

Figure 4.7: Initial Fabricated Designs: Experimentally measured transmission at a 45° angle for structures with: a) varied EBL exposure; b) varied vertical bar width.

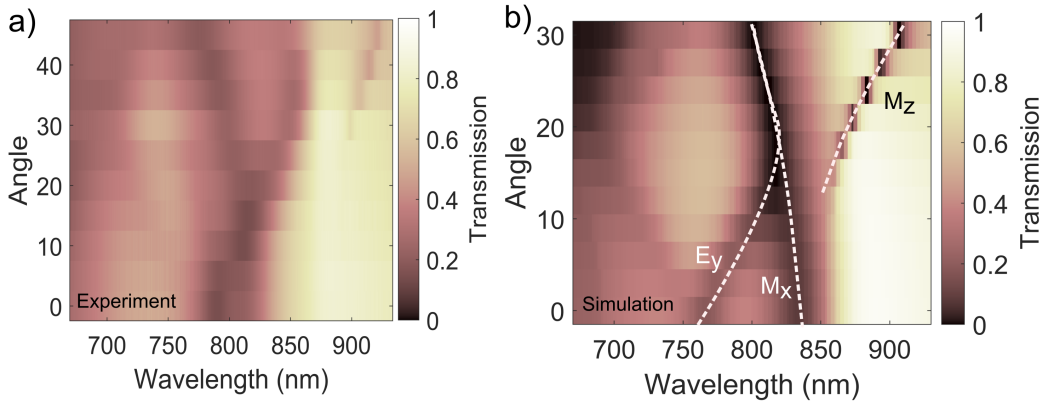

Figure 4.8: Transmission with angle of fabricated and simulated structures: a) Measured transmission spectra of a fabricated structure for varying incidence angle. b) Simulated transmission with varying incidence angle for perfectly absorbing design in Figure 4.5.

4.4 Summary

This chapter has demonstrated the design of a metasurface which is highly absorbing when excited at an incident angle of 45°, with a view to using this metasurface for THz emission. Simulations are used to understand the complicated way in which modes respond to change in incident angle, and this has been used to identify the modes in the transmission spectra of fabricated structures. Further work is required to understand the reason for discrepancies in the experimental and simulated data, and to readjust the fabricated structures to make the modes degenerate and increase absorption. Once high absorption is achieved with an angled metasurface, this metasurface can be used as a source in a THz-TDS system to evaluate its THz emission properties. Simulations suggest that the perfect absorption is robust to variation in incident beam angle, therefore making the metasurface a practical option for a broadband pulsed THz source in a range of experimental set-ups.

Chapter 5

Metasurfaces for Sub-Bandgap Photoexcitation

All the simulations and metasurface design shown in this chapter were carried out by L. Hale.

In Chapters 2 - 4, metasurfaces were designed and fabricated to operate at pump wavelengths around 800 nm, as this is the wavelength of Ti:Sapphire lasers typically used in TDS systems. However, despite their ubiquity, Ti:Sapphire lasers have several drawbacks: they are very large, expensive and often require sensitive handling and alignment as well as regular maintenance. Therefore, it would be preferable to design detectors which operate at different pump wavelengths, for which more convenient ultrafast lasers exist. For example, at 1550 nm femtosecond pulsed fiber lasers have been developed for telecom purposes which are more compact, robust and turn-key operated. Moreover, the use of 1550 nm fiber lasers suggests the attractive possibility of fully fiber-coupled THz-TDS systems. This chapter is about designing metasurfaces for PCA detectors at this new wavelength.

5.1 Terahertz PCAs at Telecom Wavelengths

The metasurfaces designed so far in this work have used LT-GaAs due to its low carrier lifetime, relatively high mobility and high dark resistance. However, because the photon energy at 1550 nm (0.8 eV) is below the GaAs bandgap energy (1.6 eV), direct absorption at this wavelength is not possible with GaAs-based photoconduc-

tors. Several methods have been proposed to tackle this issue.

One possible solution is to simply use a different photoconductive material with a lower energy bandgap. The most common are materials based on InGaAs, which has a bandgap of 0.75 eV, approximately half that of GaAs. However, using materials with a reduced bandgap has the inherent disadvantage that the bandgap is close to the thermal noise energy of the detector, resulting in poor dark resistivity. In addition, InGaAs lacks the short-carrier lifetimes required for sub-picosecond response times [27]. Attempts have been made to improve the carrier lifetime and dark resistivity by adding trapping centres by ion-implantation (usually Fe^{2+}) [94–98] and nanoparticle embedding [99, 100]. The most successful technique has been to use multi-quantum well structures (MQW) or superlattices made of alternating InGaAs/InAlGaAs layers. For example, in [101] a multilayer InGaAs:Be^{2+}/InAlGaAs structure was used to develop PCAs for an all-fiber TDS system that achieved SNR on the order of 10^3. This design has been implemented in commercial devices [102]. Despite the advancements made with InGaAs PCAs at 1550 nm, their success comes at the cost of very complex material and device designs that are difficult to grow and fabricate. Moreover, their performance as detectors is still inferior to GaAs detectors at 800 nm, which remain the popular choice. Other III-V semiconductors have also been proposed as possible candidates for PCAs, but there has been much less practical study on these, and more work is required to optimise the growth conditions for ultrafast purposes [27].

Alternatively, it is possible to excite carriers in LT-GaAs at 1550 nm via sub-bandgap absorption. Though the exact mechanism of this process is debated [13, 14, 103–108], it is thought that this is possible through two different processes: two-photon absorption (TPA) and two-step absorption (TSA) via mid-gap As defects (Fig. 5.1a). Ideally, by harnessing these effects, high absorption can be achieved without sacrificing the beneficial properties of using LT-GaAs. However, the strength of sub-bandgap absorption is particularly weak in comparison to direct absorption. In order to take advantage of this effect for efficient photoconductive antennas, it is clear that this absorption process needs to be enhanced.

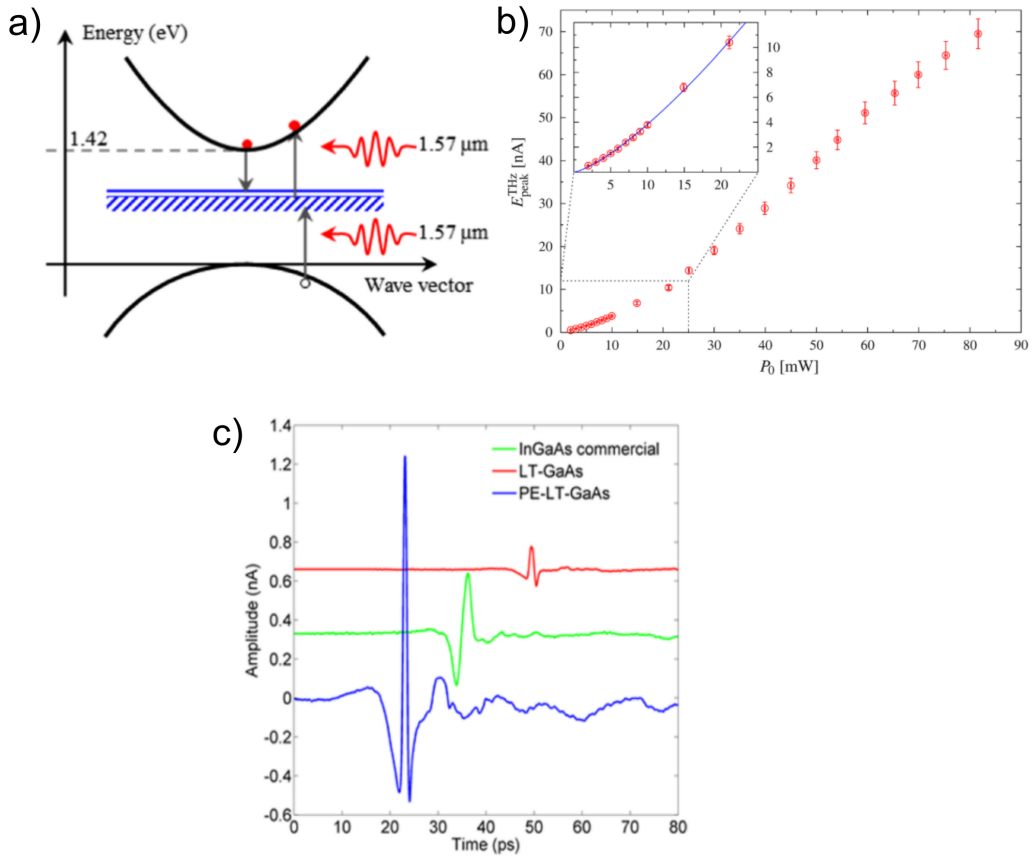

Figure 5.1: Sub-bandgap absorption in the literature: a) Schematic showing sub-bandgap absorption via midgap states, from [13]. b) THz peak amplitude dependence on optical pump power for sub-bandgap absorption, measured in [14]. A PCA emitter was used operating at 780 nm, with PCA detector operating at 1560 nm. Inset shows data fitted to $P^{1.35}$. c) Example of a THz waveform measured with a plasmon-enhanced PCA detector in [13] (operating at below-bandgap energies) which performs better than a commercial InGaAs detector.

In order to enhance sub-bandgap absorption in GaAs it is necessary to understand the absorption mechanism in more detail. For photoconductive devices, measuring photocurrent against the incident optical power provides some insight into the dominant means of absorption. For TPA, photocurrent increases quadratically with optical pump power as two photons are needed to excite a single electron into the conduction band. Erlig et al. observed this in [104], concluding that TPA was the main mechanism for absorption. However, since this, several other groups have observed different photocurrent-to-optical power relations. A superlinear but subquadratic relation (Fig. 5.1b) is most commonly observed before satu-

ration [13, 14, 103, 105] suggesting that TSA is the dominant mechanism. TSA is possible as the transition energy from the valence band to midgap states has been reported to be 0.8 eV - corresponding approximately to the wavelength of 1550 nm [108]. Although two photons are still required for excitation of an electron into the conduction band, instead of recombining the excited electron can be trapped in a mid-gap state. For electrons trapped in mid-gap states, only a single photon is required for excitation into the conduction band. TSA therefore results in the sub-quadratic but superlinear power dependence as observed in the studies mentioned. In addition, it is argued in [14] that TSA is more likely to be the dominant absorption mechanism, because the percentage of absorption by LT-GaAs photoconductors at lower optical power levels is far too high for TPA to contribute significantly. Saturation characteristics can also provide some insight into the absorption method. For TPA, the photocurrent at which saturation occurs should be the same as that of direct absorption at energies larger than the bandgap. However, saturation is observed at lower photocurrents at 1550 nm in some studies [13, 14], suggesting absorption via alternative or intermediate states which are populated quicker than conductance band states.

From the literature we can therefore conclude that whilst it is likely that both TPA and TSA play a role in sub-bandgap absorption, at the optical pump powers used in PCA detectors TSA is the dominant absorption mechanism. A few studies have focused on increasing the rate of TSA to improve sub-bandgap PCAs. The rate of absorption via midgap states is likely to be particularly high in LT-GaAs in comparison to other photoconductive materials, due to the high percentage of arsenide defects formed in the growth process. These are beneficial for short carrier lifetimes, but also provide more midgap sites for valence electrons to transition into [107]. It therefore follows that growth and annealing conditions can have a large effect on the amount of sub-bandgap absorption. In [109] it was found that reducing the anneal temperature from 580°C to 450°C increased absorption to 25% of the absorption measured when a similar device is excited at 800 nm. However, as a consequence dark resistivity is reduced. As well as studies on growth and anneal-

ing, some work done to improve sub-bandgap absorption for LT-GaAs PCAs has involved adding nanostructures, such as plasmonic features, rather than modifying the LT-GaAs material itself. One particularly notable example is [13], in which plasmonic electrodes were used to increase the photocurrent of a PCA detector at below bandgap energies by an order of magnitude (Fig. 5.1c). These devices outperformed commercial InGaAs PCA detectors in THz amplitude and bandwidth. This group also experimented with using a variety of shaped plasmonic structures which act as anti-reflection coatings as well as field enhancers [35]. Plasmonic structures were also used to improve sub-bandgap detection in [110], except in this work RF sputtering was used to deposit gold nanoislands - preventing the need for high precision EBL patterning. However, whilst plasmonic structures may improve performance to some extent they still have several drawbacks, as discussed in Section 1.3.2, such as increased dark current and higher damage threshold. Alternatively, in [38] the authors demonstrated a PCA source operating at 1550 nm that used an optical cavity with a gold grating on one side to trap photons in the photoconductive layer. This device achieved a much higher photocurrent-to-optical power ratio compared to similar, non-cavity LT-GaAs PCAs at 1550 nm. Apart from these examples, successful demonstrations of LT-GaAs PCAs operating at 1550 nm, particularly as detectors, still remain few and far between.

In Chapters 2 and 3 it was demonstrated that with the degenerate critical coupling technique, very enhanced absorption can be achieved in GaAs at wavelengths as high as 880 nm, where existing data and models for GaAs predict near-zero intrinsic absorption. This work implies that good absorption may also be possible at 1550 nm, where absorption is also predicted to be very low. In the following sections of this chapter, LT-GaAs metasurfaces operating at 1550 nm are designed, with the view to using these in PCA detectors.

5.2 Metasurface Designs at 1550 nm

The fact that there is no direct absorption in GaAs at 1550 nm poses a challenge when accurately simulating material properties. Most material data sets show very

little or no absorption at 1550 nm [11, 111–113], making it very difficult to accurately model material absorption due to TPA or TSA. Moreover, the amount of sub-bandgap absorption varies greatly between LT-GaAs samples from different sources due to different growth and annealing conditions [114]. Therefore, for the simulations shown in this chapter an estimate of the the intrinsic material absorption was used, based on typical photocurrent measurements from the literature. The generated photocurrent from unpatterned GaAs at 1550 nm has been measured to be approximately 10% of the generated photocurrent at 800 nm [14, 103], so an estimate for the extinction coefficient of $\kappa = 0.01$ – approximately 10% of the extinction coefficient at 800 nm - provides a lower bound on the intrinsic absorption at 1550 nm. The extinction coefficient and refractive index were set as constant values across the spectral range used in the simulation ($n = 3.37, \kappa = 0.01$).

The initial metasurface design used was based on the symmetric design in Section 2.4, which uses electric and magnetic dipoles for degenerate coupling. Considering the change in refractive index change with wavelength ($n = 3.68$ to $n = 3.37$), one can deduce that by simply doubling all the parameter sizes of a perfectly absorbing design at 840 nm, both modes will be degenerate at approximately 1550 nm. Figure 5.2a shows the optical properties of a simulated metasurface, which was scaled up from a design at 840 nm in [83]. The metasurface thickness was 320 nm and remains fixed at this value for all the subsequent metasurface designs simulated in this Chapter. Whilst the modes have remained degenerate (only one absorption peak is seen), the maximum absorption has significantly reduced because the critical coupling condition is no longer satisfied. This is a result of the change in intrinsic material absorption. To show how this affects the absorption spectra, in Figure 5.2b the absorption of the metasurface was simulated for varying extinction coefficient. It can be seen that, as the extinction coefficient increases, initially the peak absorption increases, as well as the modal linewidth. At approximately $\kappa = 0.06$ the metasurface is critically coupled to the incident field. As the extinction coefficient increases further, the linewidth continues to increase, but the maximum absorption decreases.

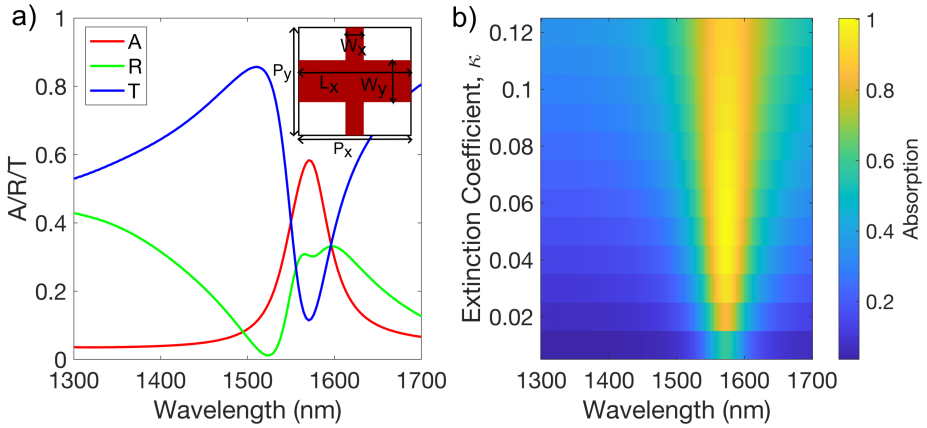

Figure 5.2: Optical properties of metasurface design, scaled up from perfectly absorbing design at 840 nm. Inset shows metasurface unit cell design. b) Absorption spectra of metasurface for varied extinction coefficient.

The metasurface geometry was then modified in order to rematch the critical coupling condition and increase the maximum absorption. In [83] it was shown that it is possible to modify absorption by changing the width of the vertical bar (W_x in Fig. 5.2a). Figure 5.3 shows the process of tuning the vertical bar width from 60 nm to 200 nm (original size in Fig. 5.2 is 180 nm). In order to critically couple the modes, it was initially expected that the bar width must increase to increase the spatial overlap of the modes with the absorbing GaAs material, and thereby increase the absorption of each mode. However, we observe that the peak absorption increases as the bar width decreases. Furthermore, the linewidth of the absorption spectra becomes extremely narrow as the absorption increases. At a bar width of 60 nm, $>$ 80% absorption is reached (Fig. 5.3b); however, the linewidth is $<$ 10 nm - less than half that of the original perfectly absorbing design at 840 nm.

By considering the critical coupling condition, one can see that a very narrow linewidth is a necessary consequence of high absorption in a material with low intrinsic absorption. If the material absorption is very small, the radiative losses must reduce in order to match the absorption loss and increase maximum absorption, thereby resulting in a narrow linewidth. However, to use the metasurface as a THz detector the linewidth of the absorption peak must be comparable to the spectral range of the laser used for excitation, in order to absorb a large percentage of the

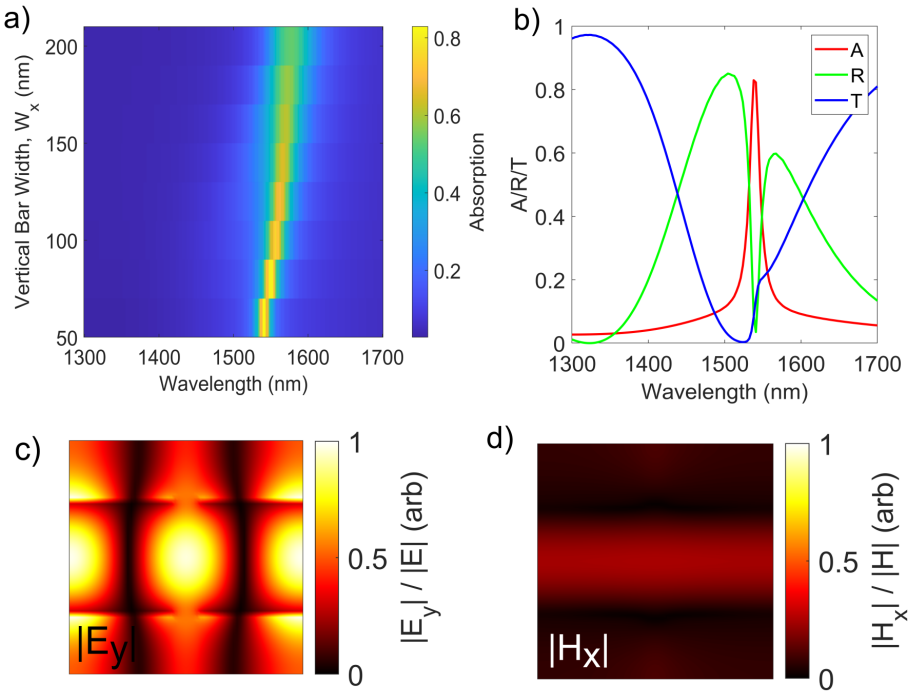

Figure 5.3: High absorption structure at 1550 nm: a) Absorption for increasing vertical bar width, W_x. b) Simulated optical properties of metasurface with $W_x = 60$ nm. c) Normalised absolute electric field in y-direction at peak absorption wavelength in (b) (showing field profile of E_y mode). d) Normalised absolute magnetic field in x-direction at peak absorption wavelength in (b) (showing field profile of M_x mode).

incident beam and have low transmission through the structure. For the 1550 nm laser intended for excitation of the metasurface (Toptica Femtofiber Pro), the spectral linewidth is approximately 35 nm [115]. Therefore, the design in Figure 5.3b is much too narrow to absorb a large proportion of the incident laser beam and must be modified to increase the linewidth. Because the narrow linewidth is a consequence of the intrinsic material properties, this cannot be done without decreasing the peak absorption. An acceptable trade off must be found between these two attributes.

The optical properties of the smallest bar width structure in Figure 5.3b, along with the mode profiles at peak absorption shown in Figures 5.3c, d, help us understand how the modes have changed in order to produce such a narrow linewidth. The transmission and reflectance spectra appear to show an almost Fano-like lineshape [116], where a broad resonance overlaps with a sharp resonance. The field

profiles at the central resonance frequency show very strong electric field corresponding to the E_y mode. In comparison, the magnetic field due to the M_x mode appears much weaker. As we move away from the central resonance frequency, the magnetic field of the M_x mode does not considerably change intensity, whereas the E_y mode intensity reduces rapidly (not shown). From this information it is deduced that the broad resonance in the spectrum is the M_x mode, whereas the E_y mode is the very narrow resonance. This is can be further understood by looking at the field profile shapes. The M_x mode profile no longer appears confined in the centre of the unit cell and the field is evenly distributed across the whole area of the horizontal bar - resembling a guided mode which is a resonance of the metasurface lattice as a whole. In contrast, the E_y mode still has a clear localised shape similar to a typical Mie mode.

It was then considered how the design could be modified to find an acceptable trade-off between peak absorption and acceptable linewidth whilst also maintaining low transmission. This is possible by reducing the linewidth of the M_x mode and thereby increasing its peak absorption, whilst increasing the linewidth of the E_y mode and accepting an inevitable decrease in peak absorption. The E_y mode is predominantly affected by changes to the metasurface in the x-direction. In Figure 5.4 the horizontal bar is shortened, so that there is a gap between neighbouring resonators in the x-direction. Fig. 5.4a shows that the E_y mode is broadened (and peak absorption decreased) by increasing the periodicity in this direction for a fixed horizontal bar length - thereby increasing the gap between resonators. The M_x mode wavelength remains unaffected by this change. Similarly, the absorption and linewidth of the M_x mode can be modified by adjusting the metasurface in the y-direction. By increasing the width of the vertical bar (Fig. 5.4b), more of the M_x mode sits in the vertical bar and the mode becomes re-localised in the centre of the unit cell. As a result, the linewidth of the M_x mode is reduced and peak absorption increases, whilst the E_y mode is relatively unaffected.

Finally, the modes can be recentered at 1550 nm by modifying other parameters, such as the horizontal bar width (Fig. 5.5a) and the periodicity in the x-

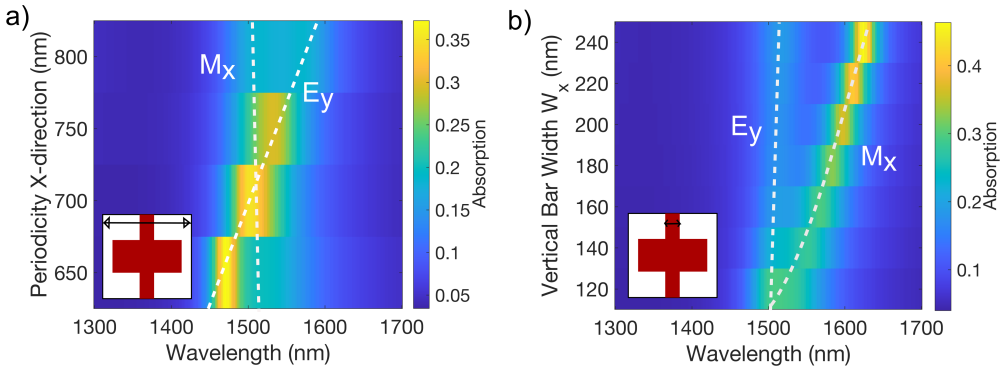

Figure 5.4: Simulated absorption spectra for varied periodicity in x-direction (horizontal bar length is 580 nm, so that neighbouring resonators are not connected). b) Simulated absorption for varied vertical bar width, W_x. White lines show the movement of each mode across the parameter space.

direction when a constant gap size is maintained between resonators (Fig. 5.5b). In Figure 5.5 it can be seen that the horizontal block width (a) affects mainly the M_x mode wavelength, whereas the the periodicity in the x-direction affects mainly the E_y mode wavelength (b).

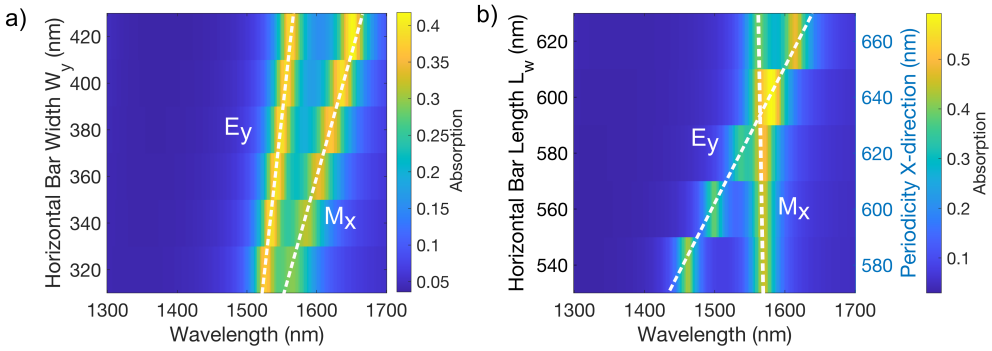

Figure 5.5: Tuning mode wavelengths: a) Simulated absorption for varied horizontal bar width, W_y. b) Simulated absorption for varied periodicity in x-direction, P_x. Horizontal bar length, L_x is also increased to maintain a constant horizontal gap size between neighbouring resonators. White lines show the movement of each mode across the parameter space.

The methods shown in Figures 5.4 and 5.5 were used to design the metasurface shown in Figure 5.6. This metasurface design reaches a maximum absorption of approximately 60% and a linewidth of $\sim$50 nm in a layer that is only 320 nm thick. This is only a slight improvement in absorption from the original design shown in

Figure 5.2, however this design also has very little transmission at the resonance wavelength and therefore is more applicable to THz detectors.

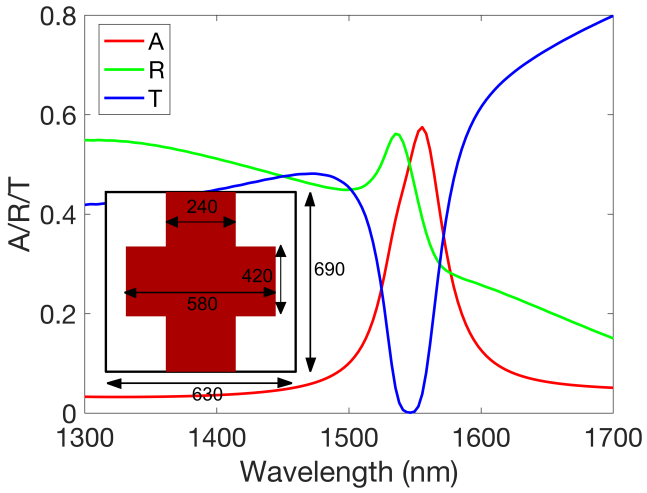

Figure 5.6: Metasurface design for absorbing metasurface below bandgap: Simulated optical properties. Inset shows dimensions of metasurface and the metasurface thickness is 320 nm.

5.3 Summary

In this chapter I have reviewed the existing literature on sub-bandgap absorption in LT-GaAs for use in PCA detectors at telecom wavelengths. I have then shown how the degenerate critical coupling mechanism can be used to design highly absorbing metasurfaces even when intrinsic absorption is very weak - such as absorption via two-photon and two-step processes. Considering the practicalities of using such metasurfaces as THz detectors, a balance needs to be struck between linewidth and peak absorption, and transmission needs to be minimised. I have shown how this is possible through modifying a few key design parameters, and demonstrated an appropriate design taking these factors into account. The next stage of this work is to fabricate the design shown in Figure 5.6. Given that an estimate was used for the 1550 nm material absorption, it is expected that the absorption for the fabricated structures may be somewhat different from the simulated values. Comparing metasurfaces simulated with varying extinction coefficients to initial measurements of the transmission and reflectance of fabricated structures would help improve our

estimate of the extinction coefficient, and the metasurface design could be modified based on this new value.

Chapter 6

Conclusions & Future Work

6.1 General Conclusions

Metasurfaces have the potential to transform optoelectronic devices by replacing bulky, sub-optimal semiconductor elements with ultra-thin layers which are tailored to have optimal optical and electronic properties. The objective of this work was to develop photoconductive metasurfaces for THz applications - in particular for THz PCA detectors, with the aim of integrating these into THz near-field probes.

Chapter 2 shows that it is possible to design metasurfaces which reach full (100%) absorption using the concept of degenerate critical coupling. By using these metasurfaces as the photoconductive layer in PCAs, optical photon-to-charge carrier conversion efficiency is maximised. Furthermore, I demonstrate that perfect absorption can be adapted across the wavelength range of typical pump lasers with simple modifications of the metasurface geometry. Using the prescriptive technique developed in Section 2.3, perfect absorption is attainable even at wavelengths where intrinsic material absorption is very low. LT-GaAs is the material of choice in this work due to its beneficial properties for ultrafast applications - however, the general design method is readily applicable to a wide range of semiconductor materials and could be used to improve devices operating across the electromagnetic spectrum.

Chapter 3 describes the fabrication of these metasurfaces and demonstrates their performance when integrated into THz PCA detectors. The metasurface PCA detectors exhibit remarkably high dark resistance, and achieve maximum SNR at

unprecedentedly low pump powers, enabling their use in a wide range of THz-TDS and imaging systems. In particular, their low pump energy requirement makes them attractive for arrays of detectors or cryogenic systems, where it is preferable to minimise heating from the pump laser. Moreover, the metasurface PCA detectors are extremely thin ($\leq$200 nm), making them highly applicable to near-field aperture probes.

In Chapter 4, the functionality of the metasurface is extended to THz emission via photoexcited charge carrier transients. It is demonstrated that perfect absorption is possible for angled illumination of the metasurface. Metasurface THz emitters could be easily integrated into a wide range of experimental set-ups, and would be particularly versatile as they do not require an applied bias for operation.

Finally, Chapter 5 explores the possibility of using metasurfaces for THz PCA detectors operating at sub-bandgap energies. It is proposed that the weak extrinsic absorption in LT-GaAs can be enhanced using metasurfaces based on degenerate critical coupling. These metasurfaces could be used in sensitive LT-GaAs PCA detectors that operate using ultrafast fiber lasers at telecom wavelengths, thus improving the efficiency of fully fiber-coupled TDS systems. Moreover, these devices could be used to develop fiber-coupled near-field systems which would be more robust, compact and easier to align - enabling widespread adoption of the aperture near-field technique.

6.2 Future Work

Potential avenues for future work can be split into three main themes: improving near-field systems, developing THz emitters and developing PCA detectors for THz systems which use ultrafast fiber lasers at telecom wavelengths.

6.2.1 Near-Field Terahertz Detectors

The most obvious progression of this work is to integrate the metasurface PCA detectors demonstrated in Section 3.3 into near-field aperture probes. The thin photoconductive region in these devices would improve the sensitivity of near-field probes, allowing weaker fields to be detected. This could allow smaller apertures to

be used (1-2 μm), increasing spatial resolution.

In addition, in Chapter 2 highly absorbing metasurfaces were developed at operation wavelengths up to 860 - 870 nm. Further work is required to test the THz detection properties of these metasurfaces, and to determine whether they achieve the same sensitivity, efficiency and bandwidth as the detectors developed at 800 nm. Following this, these detectors could also be adopted in TDS systems, or integrated into near-field probes for systems that use Ti:Sapphire lasers operating in this longer wavelength range.

6.2.2 Terahertz Emitters

To develop THz metasurface emitters, further work is required to understand the discrepancies between the fabricated and simulated metasurfaces in Chapter 4, and to fabricate metasurfaces which are highly absorbing at 45°. Following this, the emission properties of the metasurface could be tested using a standard TDS set-up. Comparing the emission of the metasurfaces to the emission from bulk semiconductors such as GaAs and InAs would elucidate the relationship between THz emission and material thickness, which will further develop our understanding of how lateral and perpendicular photocurrents contribute to emission.

6.2.3 Terahertz Systems at Telecom Wavelengths

Finally, the metasurface design for sub-bandgap absorption in Chapter 5 should be experimentally tested. Measuring the optical properties of a fabricated structure based on this design would allow us to better understand the intrinsic material absorption at this wavelength, which can then be used to inform further metasurface designs. Subsequently, these metasurfaces could be used in THz detectors, and their performance compared to typical InGaAs detectors operating at the same wavelength. I anticipate that the superior ultrafast material properties of LT-GaAs and heightened absorption of the metasurface will result in improved performance compared to typical InGaAs devices.

Appendix A

Derivation of Conditions for Perfect Absorption

As discussed in Section 2, perfect absorption can be achieved if a metasurface supports two modes which are: 1) degenerate, 2) critically coupled to the incident field and 3) of opposite symmetries to each other with respect to the metasurface plane. To understand how these conditions lead to perfect absorption we consider the excitation of a single lossy dielectric resonator using temporal coupled mode theory (TCMT) [15, 69, 117]. The metasurface described in Section 2 can be considered as an extension of this case, as it is made up of an array made up of unit cells which each contain a single GaAs resonator that individually support Mie resonances of opposing symmetries. The discussion here is adapted from [15] and [69].

For simplicity, a cylindrical dielectric resonator is considered as shown in Figure A.1. The resonator is symmetrical about its mirror plane, which cuts through the central resonator axis. It is excited on one side by light with an electric field amplitude, E, oriented normal to the mirror plane. Given that the metasurface is symmetric about its mirror plane and can be accessed from both sides (2-port system), the single port excitation can be decomposed into a combination of even and odd eigenexcitations, incident from the two identical ports. This is shown schematically in Figure A.1 – the total excitation is split into even and odd contributions, and the excitations from each port carry half of the total electric field amplitude, E/2. The even and odd eigenexcitations can only couple to even and odd eigenmodes of

matching symmetry within the resonator due to the boundary conditions imposed by the eigenexcitation decomposition [69].

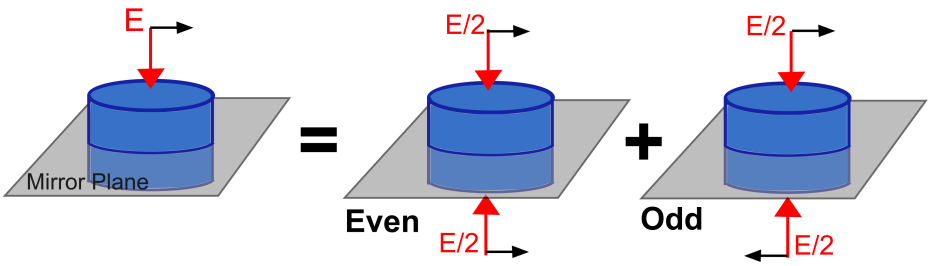

Figure A.1: Schematic of eigenexcitaion decomposition for a single 2-port dielectric cylinder resonator, adapted from [15]. A one-sided excitation can be considered as the sum of odd and even eigenexcitations with respect to the metasurface plane (grey). Each eigenexciation is made up of an excitation at each port of equal amplitude (E/2) which are symmetric and anti-symmetric to each other for the even and odd cases respectively.

If the even and odd eigenmodes are close in resonant frequency but far from other higher order modes, they can be analysed using TCMT [15, 69, 117]. Considering a system which responds linearly to the incident field, the total absorption, A of the resonator at a given frequency, ω, is a sum of the absorption from even and odd modes, given by the Lorentz terms [15]:

$$A(\omega) = A_{even} + A_{odd} = \frac{2\gamma_1\delta_1}{(\omega-\omega_{0,1})^2+(\gamma_1+\delta_1)^2} + \frac{2\gamma_2\delta_2}{(\omega-\omega_{0,2})^2+(\gamma_2+\delta_2)^2} \quad \text{(A.1)}$$

Where ω_0 is the central frequency of each mode, δ is the material loss rate and γ is the radiative loss rate. One can see from these equations that for each term, the maximum absorption possible of 1/2 is achieved at the central frequency for the mode ($\omega = \omega_0$), and when the radiative loss matches the absorption loss of the material, $\gamma = \delta$ i.e. when the mode is *critically coupled* to the incident field. It therefore follows that full (100%) absorption is achieved when the modes are degenerate. In practice the Lorentz parameters such as γ and δ are functions of the metasurface design and can be tuned by varying the size and shape of the resonators, as well as the metasurface periodicity.

Appendix B

Finite Difference Time-Domain Simulations

All the simulations in this work were done using Lumerical [118] - a commercial solver using the finite difference time-domain method [119]. In this method, Maxwell's curl equations are solved for each cell in a discrete 3D spatial grid and at discrete time-steps:

$$\frac{\partial \overrightarrow{D}}{\partial t} = \nabla \times \overrightarrow{H} \tag{B.1}$$

and

$$\frac{\partial \overrightarrow{H}}{\partial t} = -\frac{1}{\mu_0} \nabla \times \overrightarrow{E} \tag{B.2}$$

Where t is time, E is the electric field, H is the magnetic field, μ_0 is the free space permeability and D is the displacement field given by:

$$\overrightarrow{D}(\omega) = \varepsilon_0 \varepsilon_r(\omega) \overrightarrow{E}(\omega) \tag{B.3}$$

Where ω is the angular frequency, ε_r and ε_0 are the complex relative and free space permittivities. Direct time-domain information is therefore gained, and frequency domain information can be calculated using the Fourier Transform.

A schematic of the simulation set-up for the simulations in Chapter 2 is shown in Figure B.1. A unit cell of the metasurface is simulated. A no-loss, constant refractive index material ($n = 1.56$) is used to simulate the epoxy surrounding the

metasurface, and the source is injected into this material. For simplicity, in the simulations for Figures 2.3 to 2.10 the metasurface was surrounded by this material. In subsequent simulations (Figure 2.12 onwards) this material covers only half of the simulation region (surrounding the metasurface) and air ($n = 1$) is used for the top half to reflect the arrangement of the fabricated devices (as shown in Fig. B.1). Where specified in the main text, the metasurface is simulated with constant real and imaginary refractive indices, or dispersive material properties defined by a multi-coefficient numerical fitting to material data. This multi-coefficient fit uses a wider set of basis functions than typical Drude-Lorentz fits, and the number of coefficients defines the maximum number of inflection points in the fit [120]. For example, Figure 2.2 of the main text shows the imaginary material data fit using 6 coefficients with an RMS error of 0.0297 across the spectral range of the simulation.

A plane wave source is launched in the substrate material to excite the metasurface. Periodic boundary conditions are applied in x and y-directions, in order to simulate an infinite metasurface excited by a uniform plane wave. At the z-boundaries, perfectly matched layer (PML) boundaries are used. These are modelled as layers of absorbing material which is impedance-matched to the materials in the simulation region in order to absorb incident light with minimal reflections.

The size of the finite mesh used is decided by the smallest feature sizes in the simulation. For the simulations in Chapters 2 - 4, a uniform mesh with cell size of 5 nm is used in the region of the metasurface in order to fit the geometry of the metasurface, with larger, graded meshing in surrounding regions. For the simulations in Chapter 5 a larger mesh of minimum 10 nm cell size is used, due to the larger parameter sizes.

Reflection, transmission, and spatial field profile information is gained using frequency domain power monitors. For reflection and transmission, these are placed at the top and bottom of the simulation region and integrated output power is measured across the monitor area (see Fig. B.1) and is normalised to the source power. These monitors must be placed greater than a wavelength's length in the material away from the absorbing structure for accurate results. For field profiles, the mon-

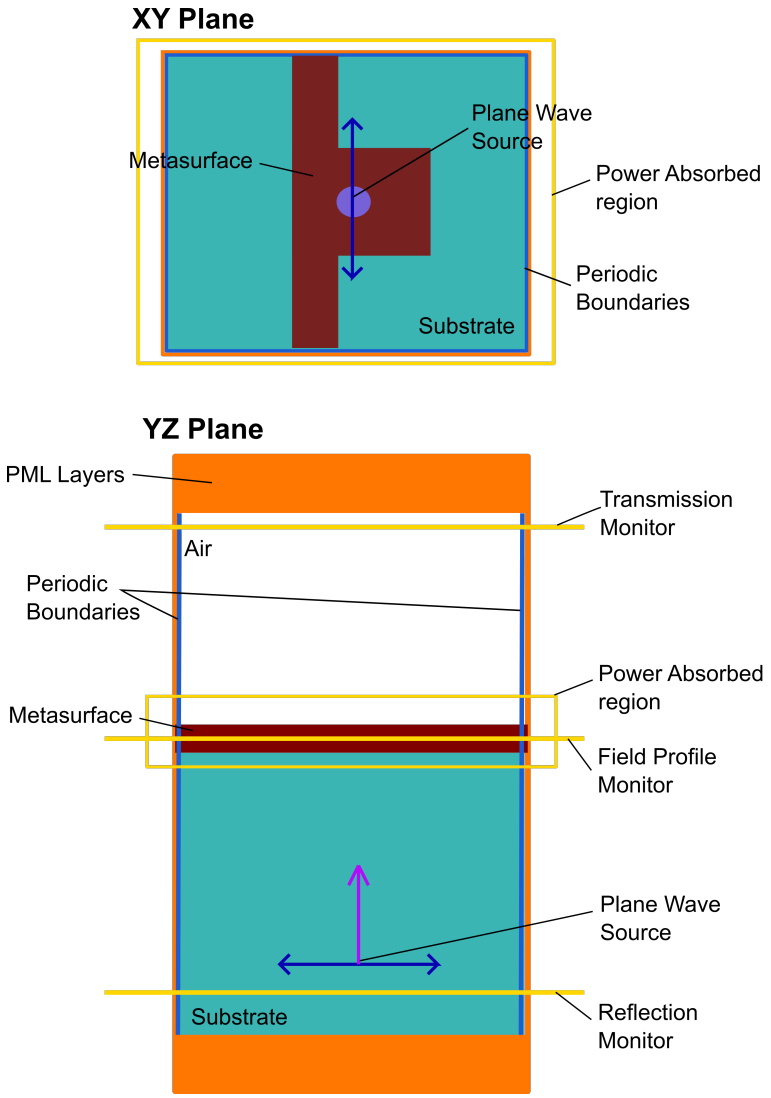

Figure B.1: Schematic of typical periodic simulation set up in x-y and y-z planes.

itor is placed across the x-y plane, through the centre of the metasurface in the z-direction. Output fields in all directions (E_x, E_y, E_z, H_x, H_y and H_z) across the simulation frequency range can be measured.

Absorption is measured as a product of the electric field intensity and imaginary part of the permittivity, and is integrated over a volume of the simulation region containing absorbing material. To confirm the accuracy of this measurement, it is compared against the absorbtion measured as $A = 1 - (R + T)$.

B.1 Finite Numerical Aperture Simulations

In Section 3.2.3 the metasurface was simulated with a gaussian beam excitation, in order to understand the effect of a finite numerical aperture on the metasurface absorption. A finite 15 x 15 metasurface array was simulated with PML boundaries in all directions. Instead of a plane wave source, a gaussian beam source was focussed on the centre of the metasurface with a numerical aperture of NA = 0.2. Given the substantially larger simulation size and memory requirement, it was not possible to measure the power absorbed over the whole metasurface array. Alternatively, absorption was calculated as $A = 1 - (R + T)$ using reflection and transmission monitors.

B.2 Angled Simulations

In order to calculate the metasurface properties when illuminated at an oblique angle in Chapter 4, several changes must be made to the simulation set-up. As shown in Figure 4.1 of the main text, the metasurface remained perpendicular to the simulation x and y boundaries, and the source itself was angled. The source polarisation was maintained at 90° to the source angle i.e. in the direction of the vertical bar for both structures.

In the simulation, the source is launched in the 'epoxy' substrate itself, whereas in reality the light is incident on the sapphire substrate from air, and travels through the sapphire to the epoxy. To account for this difference, the angle of incidence used in the simulation was calculated using Snell's law, to take into account the change in angle when travelling through the change refractive index in the substrate. Figure B.2 shows this change in angle and the injection angle from air for each incident angle in the simulation.

Several problems arise from using a broadband plane wave source at an angle. Firstly, light is incident on PML boundaries at grazing angles, causing unwanted reflections. To avoid this, more PML layers are required. For the simulations in Chapter 4, the 'Steep Angle' PML settings were used, which has a minimum of 12 PML layers, rather than the standard 8 layers. The number of layers is increased as

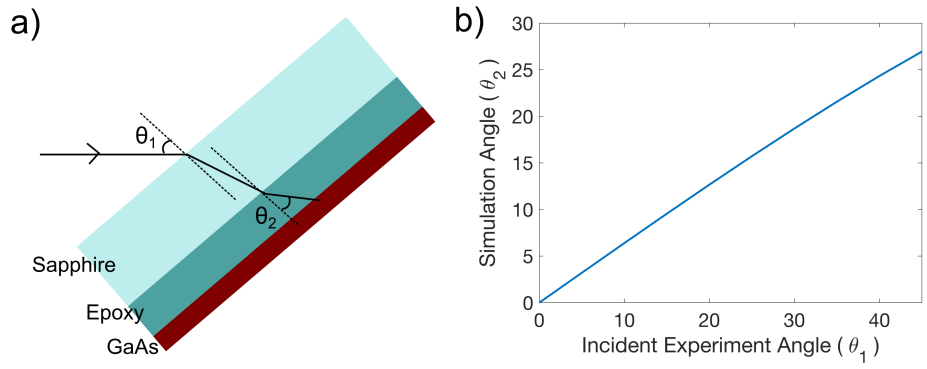

Figure B.2: Angled illumination: a) Schematic showing refraction of incident beam in sapphire and epoxy substrates. b) Graph showing the simulation angle (θ_2) used to reflect each incident angle from air (θ_1).

the source angle increases.

Periodic boundary conditions are also problematic for angled sources. Firstly, periodic boundaries do not take into account the phase change across each period for angled light. Furthermore, when using periodic boundary conditions the injection angle of the source varies for different frequencies within the source bandwidth. This arises from the fact that the in-plane k-vector, $k_{inplane}$, is calculated from the k-vector at the centre of the simulation bandwidth, k_{sim} (which is a function of frequency, f_{sim}) and the source angle, θ_{sim}:

$$k_{inplane} = k_{sim} \sin \theta_{sim} \tag{B.4}$$

$$k_{sim} = 2\pi \frac{f_{sim}}{c} \tag{B.5}$$

Where c is the speed of light. Figure B.3 shows the variation in source angle across the source spectrum for a source angle of 28°. To prevent these issues, the Lumerical BFAST setting is used, which reformulates the FDTD equations into an angle-independent basis. However, BFAST settings are inherently more unstable than standard FDTD settings, and therefore the PML layers and simulation time step must be increased for stability at larger angles. Convergence testing was used to find the appropriate values for these when carrying out the simulations in Chapter 4.

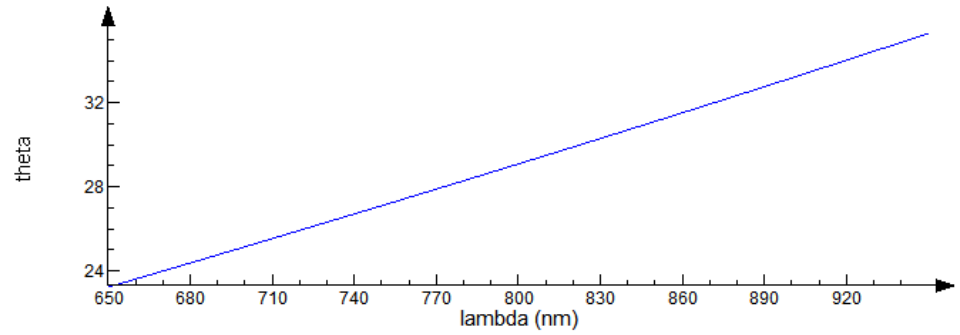

Figure B.3: Angled illumination: Change in simulated source angle with wavelength when regular periodic boundary conditions are used.

B.3 Simulations at 1550 nm

In Chapter 5 I aim to simulate metasurfaces excited by light at sub-bandgap energies. In order to do this, constant n, κ values are used. The chosen refractive index of $n = 3.37$ is taken from [112]. The GaAs refractive index does not change significantly in the 1.3 – 1.7 μm range, justifying the use of a constant value. The argument for using an extinction coefficient of $\kappa = 0.01$ is as follows. Several studies have measured that for the same PCA devices, photocurrent measured when the device is illuminated at around 1550 nm is approximately 10% of the photocurrent measured when the device is illuminated at energies above the bandgap (around 800 nm). For PCAs, the photocurrent is proportional to the charge carrier density and THz field as shown in Equation 3.1. Assuming no thermal generation of carriers, the charge carrier generation rate is proportional to the absorbance of the material, which is proportional to its extinction coefficient. Therefore, it can be estimated that the extinction coefficient is also 10% of the extinction coefficient below bandgap. This provides an estimate only, as in reality other factors may vary between absorption above and below bandgap (for example, the rate of carrier recombination may change depending on the lifetime of the conduction midgap states [106]). More analysis of the sub-bandgap absorption mechanisms and charge carrier dynamics would be required to determine a more accurate calculation of the extinction coefficient.

Appendix C

Fabrication Methods

The basic metasurface fabrication procedure is described in Section 3.1.1. This appendix aims to provide more information about specific fabrication conditions and methods used.

The low temperature (LT) GaAs used for the metasurface is grown at 250° on a semi-insulating (SI) GaAs substrate. Two AlGaAs stop-etch layers are grown 100 nm apart between the SI-GaAs and LT-GaAs. The LT-GaAs is annealed at 600° for 40 seconds in forming gas. For the metasurface EBL patterning, two layers of photoresist (PMMA495A4/PMMA950A4) are used to assist with mask lift-off. When determining the correct fabrication procedure for a specific metasurface design, several metasurfaces are patterned in a grid, with one metasurface parameter (eg. vertical bar width) varied in one direction, and electron-beam dosage varied along the other direction. By inspecting the designs in an SEM and testing their optical properties after fabrication, the pattern and electron-beam dosage are chosen which give an accurate replication of the intended metasurface design. This may vary between different metasurface designs.

The photoresist is developed using a 1:3 ratio methyl isobutyl ketone / isopropylalcohol (MBIK/IPA) solution for 60s and rinsed with IPA. A hard 30 nm SiO_2 mask is deposited using electron beam evaporation. The sample is then left to soak in acetone to remove the excess photoresist and leave the SiO_2 mask on the LT-GaAs.

The metasurface pattern is etched in an inductively coupled plasma (ICP) re-

active ion etching (RIE) chamber with BCl_3, Ar and N_2 gases in a combination that minimises undercutting. The SiO_2 mask is then removed using a buffered oxide wet etch.

If the metasurface is used in a PCA detector, the metallic dipole antennas are patterned using EBL, electron-beam evaporation and lift-off in a similar way to the metasurface pattern. The antenna bars are 200 nm thick, 10 μm wide, and ∼80 μm long.

The metasurface is then turned over and stuck to 0.5 mm thick sapphire substrate using ∼2 μm of epoxy. The metasurface is then mechanically lapped on the exposed SI-GaAs side and wet etched in citric acid and hydrogen peroxide to the AlGaAs stop-etch layers. The result is that the LT-GaAs metasurface is exposed on one side, submerged in epoxy, with the metallic antennae deposited on the other side, attached to the sapphire substrate.

Bibliography

[1] Masayoshi Tonouchi. Cutting-edge terahertz technology. *Nature Photonics*, 1(2):97–105, 2007.

[2] O. Mitrofanov, W. Yu, R. J. Thompson, Y. Jiang, Z. J. Greenberg, J. Palmer, I. Brener, W. Pan, C. Berger, W. A. De Heer, and Z. Jiang. Terahertz near-field imaging of surface plasmon waves in graphene structures. *Solid State Communications*, 224:47–52, 2015.

[3] Lucy L. Hale, Janine Keller, Thomas Siday, Rodolfo I. Hermans, Johannes Haase, John L. Reno, Igal Brener, Giacomo Scalari, Jérôme Faist, and Oleg Mitrofanov. Noninvasive Near-Field Spectroscopy of Single Subwavelength Complementary Resonators. *Laser and Photonics Reviews*, 14(4):1–9, 2020.

[4] Oleg Mitrofanov, Irina Khromova, Thomas Siday, Robert J. Thompson, Andrey N. Ponomarev, Igal Brener, and John L. Reno. Near-Field Spectroscopy and Imaging of Subwavelength Plasmonic Terahertz Resonators. *IEEE Transactions on Terahertz Science and Technology*, 6(3):382–388, 2016.

[5] Irina Khromova, Petr Kužel, Igal Brener, John L. Reno, U. Chan Chung Seu, Catherine Elissalde, Mario Maglione, Patrick Mounaix, and Oleg Mitrofanov. Splitting of magnetic dipole modes in anisotropic TiO2 micro-spheres. *Laser and Photonics Reviews*, 10(4):681–687, 2016.

[6] Sang Gil Park, Kyong Hwan Jin, Minwoo Yi, Jong Chul Ye, Jaewook Ahn, and Ki Hun Jeong. Enhancement of terahertz pulse emission by optical nanoantenna. *ACS Nano*, 3(3):2026–2031, 2012.

[7] Barmak Heshmat, Hamid Pahlevaninezhad, Yuanjie Pang, Mostafa Masnadi-Shirazi, Ryan Burton Lewis, Thomas Tiedje, Reuven Gordon, and Thomas Edward Darcie. Nanoplasmonic terahertz photoconductive switch on GaAs. *Nano Letters*, 12:6255–6259, 2012.

[8] Nezih T. Yardimci, Semih Cakmakyapan, Soroosh Hemmati, and Mona

Jarrahi. High-Power photoconductive terahertz source enabled by three-dimensional light confinement. *International Conference on Infrared, Millimeter, and Terahertz Waves, IRMMW-THz*, pages 4–5, 2017.

[9] Oleg Mitrofanov, Igal Brener, Ting Shan Luk, and John L. Reno. Photoconductive Terahertz Near-Field Detector with a Hybrid Nanoantenna Array Cavity. *ACS Photonics*, 2:1763–1768, 2015.

[10] Sergey Kruk and Yuri Kivshar. Functional Meta-Optics and Nanophotonics Govern by Mie Resonances. *ACS Photonics*, 4:2638–2649, 2017.

[11] Edward D. Palik. Optical Parameters for the Materials in HOC I, HOC II, and HOC III. In *Handbook of Optical Constants of Solids*. Academic Press, 1997.

[12] Oleg Mitrofanov, Thomas Siday, Robert J. Thompson, Ting Shan Luk, Igal Brener, and John L. Reno. Efficient photoconductive terahertz detector with all-dielectric optical metasurface. *APL Photonics*, 3(5), 2018.

[13] Afshin Jooshesh, Vahid Bahrami-Yekta, Jinye Zhang, Thomas Tiedje, Thomas E. Darcie, and Reuven Gordon. Plasmon-Enhanced below Bandgap Photoconductive Terahertz Generation and Detection. *Nano Letters*, 15:8306–8310, 2015.

[14] Jan-Martin Ramer, Frank Ospald, Georg von Freymann, and Rene Beigang. Generation and detection of terahertz radiation up to 4.5 THz by low-temperature grown GaAs photoconductive antennas excited at 1560nm. *Applied Physics Letters*, 2013.

[15] Xianshun Ming, Xinyu Liu, Liqun Sun, and Willie J. Padilla. Degenerate critical coupling in all-dielectric metasurface absorbers. *Optics Express*, 25(20):24658, 2017.

[16] S S Dhillon, M S Vitiello, E H Linfield, A G Davies, Matthias C Hoffmann, John Booske, Claudio Paoloni, M Gensch, P Weightman, G P Williams,

E Castro-Camus, D R S Cumming, F Simoens, I Escorcia-Carranza, J Grant, Stepan Lucyszyn, Makoto Kuwata-Gonokami, Kuniaki Konishi, Martin Koch, Charles A Schmuttenmaer, Tyler L Cocker, Rupert Huber, A G Markelz, Z D Taylor, Vincent P Wallace, J Axel Zeitler, Juraj Sibik, Timothy M Korter, B Ellison, S Rea, P Goldsmith, Ken B Cooper, Roger Appleby, D Pardo, P G Huggard, V Krozer, Haymen Shams, Martyn Fice, Cyril Renaud, Alwyn Seeds, Andreas Stöhr, Mira Naftaly, Nick Ridler, Roland Clarke, John E Cunningham, and Michael B Johnston. The 2017 terahertz science and technology roadmap. *Journal of Physics D: Applied Physics*, 50(4):043001, 2017.

[17] R. A. Lewis. Physical phenomena in electronic materials in the terahertz region. *Proceedings of the IEEE*, 95(8):1641–1645, 2007.

[18] Aurele Joseph Louis Adam. Review of near-field Terahertz measurement methods and their applications: How to achieve sub-wavelength resolution at THz frequencies. *Journal of Infrared, Millimeter, and Terahertz Waves*, 32(8-9):976–1019, 2011.

[19] F. Blanchard, A. Doi, T. Tanaka, and K. Tanaka. Real-Time, Subwavelength Terahertz Imaging. *Annual Review of Materials Research*, 43(1):237–259, 2013.

[20] Oleg Mitrofanov, Mark Lee, Julia W.P. Hsu, Igal Brener, Roey Harel, John F. Federici, James D. Wynn, Loren N. Pfeiffer, and Ken W. West. Collection-mode near-field imaging with 0.5-THz pulses. *IEEE Journal on Selected Topics in Quantum Electronics*, 7(4):600–607, 2001.

[21] Xinzhong Chen, Debo Hu, Ryan Mescall, Guanjun You, D. N. Basov, Qing Dai, and Mengkun Liu. Modern Scattering-Type Scanning Near-Field Optical Microscopy for Advanced Material Research. *Advanced Materials*, 31(1804774), 2019.

[22] George R. Keiser and Pernille Klarskov. Terahertz field confinement in nonlinear metamaterials and near-field imaging. *Photonics*, 6(22), 2019.

[23] A. J. Huber, F. Keilmann, J. Wittborn, J. Aizpurua, and R. Hillenbrand. Terahertz near-field nanoscopy of mobile carriers in single semiconductor nanodevices. *Nano Letters*, 8(11):3766–3770, 2008.

[24] Bernhard Knoll and Fritz Keilmann. Enhanced dielectric contrast in scattering-type scanning near-field optical microscopy. *Optics Communications*, 182:321–328, 2000.

[25] D. Grischkowsky, Søren Keiding, Martin van Exter, and Ch. Fattinger. Far-infrared time-domain spectroscopy with terahertz beams of dielectrics and semiconductors. *Journal of the Optical Society of America B*, 7(10):2006, 1990.

[26] Oleg Mitrofanov, Filip Dominec, Petr Kužel, John L Reno, Igal Brener, U-Chan Chung, Cathy Elissalde, Mario Maglione, and Patrick Mounaix. Near-field probing of Mie resonances in single TiO_2 microspheres at terahertz frequencies. *Optics Express*, 22(19):23034, 2014.

[27] Nathan M. Burford and Magda O. El-Shenawee. Review of terahertz photoconductive antenna technology. *Optical Engineering*, 56(1), 2017.

[28] Nezih Tolga Yardimci and Mona Jarrahi. Nanostructure-Enhanced Photoconductive Terahertz Emission and Detection. *Small*, page 1802437, 2018.

[29] Christopher W. Berry, Ning Wang, Mohammad R. Hashemi, and Mona Jarrahi. Plasmonic photoconductive antennas for high-power terahertz generation and high-sensitivity terahertz detection. In *8th European Conference on Antennas and Propagation, EuCAP 2014*, 2014.

[30] Shang Hua Yang, Mohammad R Hashemi, Christopher W Berry, and Mona Jarrahi. 7.5% Optical-to-terahertz conversion efficiency offered by photocon-

ductive emitters with three-dimensional plasmonic contact electrodes. *IEEE Transactions on Terahertz Science and Technology*, 4(5), 2014.

[31] Giorgos Georgiou, Clément Geffroy, Christopher Bäuerle, and Jean François Roux. Efficient Three-Dimensional Photonic-Plasmonic Photoconductive Switches for Picosecond THz Pulses. *ACS Photonics*, 7:1444–1451, 2020.

[32] Sang-Gil Park, Yongje Choi, Young-Jae Oh, and Ki-Hun Jeong. Terahertz photoconductive antenna with metal nanoislands. *Optics Express*, 20(23), 2012.

[33] Nathan M. Burford, Michael J. Evans, and Magda O. El-Shenawee. Plasmonic Nanodisk Thin-Film Terahertz Photoconductive Antenna. *IEEE Transactions on Terahertz Science and Technology*, 8(2):237–247, 2018.

[34] Afshin Jooshesh, Levi Smith, Mostafa Masnadi-Shirazi, Vahid Bahrami-Yekta, Thomas Tiedje, Thomas E Darcie, and Reuven Gordon. Nanoplasmonics enhanced terahertz sources. *Optics Express*, 22(23):27992–28001, 2014.

[35] Faezeh Fesharaki, Afshin Jooshesh, Vahid Bahrami-Yekta, Mahsa Mahtab, Tom Tiedje, Thomas E. Darcie, and Reuven Gordon. Plasmonic Antireflection Coating for Photoconductive Terahertz Generation. *ACS Photonics*, 4(6):1350–1354, 2017.

[36] Xurong Li, Nezih Tolga Yardimci, and Mona Jarrahi. A polarization-insensitive plasmonic photoconductive terahertz emitter. *AIP Advances*, 7(11), 2017.

[37] C. W. Berry, N. Wang, M. R. Hashemi, M. Unlu, and M. Jarrahi. Significant performance enhancement in photoconductive terahertz optoelectronics by incorporating plasmonic contact electrodes. *Nature Communications*, 4:1610–1622, 2013.

[38] M Billet, P Latzel, F Pavanello, G Ducournau, J.-F Lampin, and E Peytavit. Resonant cavities for efficient LT-GaAs photoconductors operating at λ = 1550 nm. *APL Photonics*, 1:076102, 2016.

[39] Sascha Preu, Gottfried H. Döhler, Stefan Malzer, Andreas Stöhr, Vitaly Rymanov, Thorsten Göbel, Elliott R. Brown, Michael Feiginov, Ramón Gonzalo, Miguel Beruete, and Miguel Navarro-Cía. *Principles of THz Generation*, chapter 2, pages 3–68. John Wiley & Sons, Ltd, 2015.

[40] M.D. Sturge. Optical Absorption of Gallium Arsenide between 0.6 and 2.75 eV. *Physical Review*, 127(3):2835, 1963.

[41] Raimund Mueckstein and Oleg Mitrofanov. Imaging of terahertz surface plasmon waves excited on a gold surface by a focused beam. *Optics Express*, 19(4):3212, 2011.

[42] R. J. Thompson, T. Siday, S. Glass, T. S. Luk, J. L. Reno, I. Brener, and O. Mitrofanov. Optically thin hybrid cavity for terahertz photo-conductive detectors. *Applied Physics Letters*, 110(4):1–6, 2017.

[43] Hou Tong Chen, Antoinette J. Taylor, and Nanfang Yu. A review of metasurfaces: Physics and applications. *Reports on Progress in Physics*, 79(7):0–59, 2016.

[44] Igal Brener, Sheng Liu, Isabelle Staude, Jason Valentine, and Christopher L Holloway. *Dielectric Metamaterials: Fundamentals, Designs and Applications*. Woodhead Publishing, 1st edition, 2019.

[45] Isabelle Staude, Thomas Pertsch, and Yuri S. Kivshar. All-Dielectric Resonant Meta-Optics Lightens up. *ACS Photonics*, 6(4):802–814, 2019.

[46] Arseniy I. Kuznetsov, Andrey E. Miroshnichenko, Mark L. Brongersma, Yuri S. Kivshar, and Boris Luk'yanchuk. Optically resonant dielectric nanostructures. *Science*, 354(6314), 2016.

[47] Shang Sun, Zhenxing Zhou, Zonghui Duan, Shumin Xiao, and Qinghai Song. All-dielectric metasurface for polarization-insensitive color printing. *ACS Nano*, 11:4445–4452, 2017.

[48] Sheng Liu, Polina P. Vabishchevich, Aleksandr Vaskin, John L. Reno, Gordon A. Keeler, Michael B. Sinclair, Isabelle Staude, and Igal Brener. An all-dielectric metasurface as a broadband optical frequency mixer. *Nature Communications*, 9(1):1–6, 2018.

[49] Kebin Fan, Jonathan Y. Suen, Xinyu Liu, and Willie J. Padilla. All-dielectric metasurface absorbers for uncooled terahertz imaging. *Optica*, 4(6):601, 2017.

[50] Claire M. Watts, Xianliang Liu, and Willie J. Padilla. Metamaterial electromagnetic wave absorbers. *Advanced Materials*, 24(23), 2012.

[51] Y. Ra'di, C. R. Simovski, and S. A. Tretyakov. Thin Perfect Absorbers for Electromagnetic Waves: Theory, Design, and Realizations. *Physical Review Applied*, 3(3):1–37, 2015.

[52] Harry A. Atwater and Albert Polman. Plasmonics for improved photovoltaic devices. *Nature Materials*, 9(3):205–213, 2010.

[53] Chun Chieh Chang, Li Huang, John Nogan, and Hou Tong Chen. Invited Article: Narrowband terahertz bandpass filters employing stacked bilayer metasurface antireflection structures. *APL Photonics*, 3(5), 2018.

[54] Abul K. Azad, Wilton J.M. Kort-Kamp, Milan Sykora, Nina R. Weisse-Bernstein, Ting S. Luk, Antoinette J. Taylor, Diego A.R. Dalvit, and Hou Tong Chen. Metasurface Broadband Solar Absorber. *Scientific Reports*, 6:20347, 2016.

[55] M. D. Goldflam, E. A. Kadlec, B. V. Olson, J. F. Klem, S. D. Hawkins, S. Parameswaran, W. T. Coon, G. A. Keeler, T. R. Fortune, A. Tauke-Pedretti,

J. R. Wendt, E. A. Shaner, P. S. Davids, J. K. Kim, and D. W. Peters. Enhanced infrared detectors using resonant structures combined with thin type-II superlattice absorbers. *Applied Physics Letters*, 109(25), 2016.

[56] Na Liu, Martin Mesch, Thomas Weiss, Mario Hentschel, and Harald Giessen. Infrared perfect absorber and its application as plasmonic sensor. *Nano Letters*, 10(7):2342–2348, 2010.

[57] Chi Yin Yang, Jhen Hong Yang, Zih Ying Yang, Zhong Xing Zhou, Mao Guo Sun, Viktoriia E. Babicheva, and Kuo Ping Chen. Nonradiating Silicon Nanoantenna Metasurfaces as Narrowband Absorbers. *ACS Photonics*, 5(7):2596–2601, 2018.

[58] Viktoriia E. Babicheva and Andrey B. Evlyukhin. Resonant Lattice Kerker Effect in Metasurfaces With Electric and Magnetic Optical Responses. *Laser and Photonics Reviews*, 11(6):1–10, 2017.

[59] Xiaoguang Zhao, Yue Wang, Jacob Schalch, Guangwu Duan, Kevin Cremin, Jingdi Zhang, Chunxu Chen, Richard D. Averitt, and Xin Zhang. Optically Modulated Ultra-Broadband All-Silicon Metamaterial Terahertz Absorbers. *ACS Photonics*, 6(4):830–837, 2019.

[60] Michael A Cole, David A Powell, and Ilya V Shadrivov. Strong terahertz absorption in all-dielectric Huygens' metasurfaces. *Nanotechnology*, 27(42), 2016.

[61] Jonathan Y. Suen, Kebin Fan, and Willie J. Padilla. A Zero-Rank, Maximum Nullity Perfect Electromagnetic Wave Absorber. *Advanced Optical Materials*, 7(8):1–6, 2019.

[62] Xinyu Liu, Kebin Fan, Ilya V. Shadrivov, and Willie J. Padilla. Experimental realization of a terahertz all-dielectric metasurface absorber. *Optics Express*, 25(1):191, 2017.

[63] Alexander E. Yachmenev, Denis V. Lavrukhin, Igor A. Glinskiy, Nikolay V. Zenchenko, Yurii G. Goncharov, Igor E. Spektor, Rustam A. Khabibullin, Taiichi Otsuji, and Dmitry S. Ponomarev. Metallic and dielectric metasurfaces in photoconductive terahertz devices: a review. *Optical Engineering*, 59(6):061608, 2019.

[64] Qing Yu, Jianqiang Gu, Quanlong Yang, Ying Zhang, Yanfeng Li, Zhen Tian, Chunmei Ouyang, Jiaguang Han, John F. O'hara, and Weili Zhang. All-dielectric meta-lens designed for photoconductive terahertz antennas. *IEEE Photonics Journal*, 9(4), 2017.

[65] Xue Jiang, Hao Chen, Zeyu Li, Hongkuan Yuan, Luyao Cao, Zhenfei Luo, Kun Zhang, Zhihai Zhang, Zhongquan Wen, Li-guo Zhu, Xun Zhou, Gaofeng Liang, Desheng Ruan, Lianghui Du, Lingfang Wang, and Gang Chen. All-dielectric metalens for terahertz wave imaging. *Optics Express*, 26(11):14132, 2018.

[66] Mohammad Bashirpour, Matin Forouzmehr, Seyed Ehsan Hosseininejad, Mohammadreza Kolahdouz, and Mohammad Neshat. Improvement of Terahertz Photoconductive Antenna using Optical Antenna Array of ZnO Nanorods. *Scientific Reports*, 9(1414):1–8, 2019.

[67] L. L. Hale, P. P. Vabischevich, T. Siday, C. T. Harris, T. S. Luk, S. J. Addamane, J. L. Reno, I. Brener, and O. Mitrofanov. Perfect absorption in GaAs metasurfaces near the bandgap edge. *Optics Express*, 28(23):35284, 2020.

[68] Rasoul Alaee, Mohammad Albooyeh, and Carsten Rockstuhl. Theory of metasurface based perfect absorbers. *Journal of Physics D: Applied Physics*, 50(50):1–14, 2017.

[69] Jessica R. Piper, Victor Liu, and Shanhui Fan. Total absorption by degenerate critical coupling. *Applied Physics Letters*, 104(25), 2014.

[70] T. H. P Chang. Proximity effect in electron-beam lithography. *Journal of Vacuum Science and Technology*, 12(1271), 1975.

[71] Seyoon Kim, Min Seok Jang, Victor W. Brar, Kelly W. Mauser, Laura Kim, and Harry A. Atwater. Electronically Tunable Perfect Absorption in Graphene. *Nano Letters*, 18(2):971–979, 2018.

[72] Joo Yun Jung, Kyungjun Song, Jun Hyuk Choi, Jihye Lee, Dae Geun Choi, Jun Ho Jeong, and Dean P. Neikirk. Infrared broadband metasurface absorber for reducing the thermal mass of a microbolometer. *Scientific Reports*, 7(1):1–8, 2017.

[73] Salvatore Campione, Sheng Liu, Lorena I. Basilio, Larry K. Warne, William L. Langston, Ting S. Luk, Joel R. Wendt, John L. Reno, Gordon A. Keeler, Igal Brener, and Michael B. Sinclair. Broken Symmetry Dielectric Resonators for High Quality Factor Fano Metasurfaces. *ACS Photonics*, 3(12):2362–2367, 2016.

[74] Younes Ra'di, Alex Krasnok, and Andrea Alú. Virtual Critical Coupling. *ACS Photonics*, 7(6):1468–1475, 2020.

[75] Polina P. Vabishchevich, Sheng Liu, Michael B. Sinclair, Gordon A. Keeler, Gregory M. Peake, and Igal Brener. Enhanced Second-Harmonic Generation Using Broken Symmetry III-V Semiconductor Fano Metasurfaces. *ACS Photonics*, 5(5):1685–1690, 2018.

[76] Kirill Koshelev, Sergey Lepeshov, Mingkai Liu, Andrey Bogdanov, and Yuri Kivshar. Asymmetric Metasurfaces with High- Q Resonances Governed by Bound States in the Continuum. *Physical Review Letters*, 121(19):193903, 2018.

[77] Jianfa Zhang, Kevin F. MacDonald, and Nikolay I. Zheludev. Near-infrared trapped mode magnetic resonance in an all-dielectric metamaterial. *Optics Express*, 21(22):26721, 2013.

[78] Saman Jahani and Zubin Jacob. All-dielectric metamaterials. *Nature Nanotechnology*, 11(1):23–36, 2016.

[79] Christian C. Nadell, Bohao Huang, Jordan M. Malof, and Willie J. Padilla. Deep learning for accelerated all-dielectric metasurface design. *Optics Express*, 27(20):27523, 2019.

[80] Moritz Wenclawiak, Karl Unterrainer, and Juraj Darmo. Cooperative effects in an ensemble of planar meta-atoms. *Applied Physics Letters*, 110(261101), 2017.

[81] Janine Keller, Curdin Maissen, Johannes Haase, Gian Lorenzo Paravicini-Bagliani, Federico Valmorra, José Palomo, Juliette Mangeney, Jérôme Tignon, Sukhdeep S. Dhillon, Giacomo Scalari, and Jérôme Faist. Coupling Surface Plasmon Polariton Modes to Complementary THz Metasurfaces Tuned by Inter Meta-Atom Distance. *Advanced Optical Materials*, 5(6), 2017.

[82] Ivana Sersic, Martin Frimmer, Ewold Verhagen, and A Femius Koenderink. Electric and Magnetic Dipole Coupling in Near-Infrared Split-Ring Metamaterial Arrays. *Physical Review Letters*, 103(213902), 2009.

[83] Oleg Mitrofanov, Lucy L. Hale, Polina P. Vabishchevich, Ting Shan Luk, Sadhvikas J. Addamane, John L. Reno, and Igal Brener. Perfectly absorbing dielectric metasurfaces for photodetection. *APL Photonics*, 5(10), 2020.

[84] Thomas Siday, Polina P. Vabishchevich, Lucy Hale, Charles Thomas Harris, Ting Shan Luk, John L. Reno, Igal Brener, and Oleg Mitrofanov. Terahertz Detection with Perfectly-Absorbing Photoconductive Metasurface. *Nano Letters*, 19(5):2888–2896, 2019.

[85] H. C. Casey, D. D. Sell, and K. W. Wecht. Concentration dependence of the absorption coefficient for n- and p-type GaAs between 1.3 and 1.6 eV. *Journal of Applied Physics*, 46(1):250–257, 1975.

[86] X. C. Zhang, B. B. Hu, J. T. Darrow, and D. H. Auston. Generation of femtosecond electromagnetic pulses from semiconductor surfaces. *Applied Physics Letters*, 56(11):1011–1013, 1990.

[87] X. C. Zhang and D. H. Auston. Optoelectronic measurement of semiconductor surfaces and interfaces with femtosecond optics. *Journal of Applied Physics*, 71(1):326–338, 1992.

[88] Kai Liu, Jingzhou Xu, Tao Yuan, and X. C. Zhang. Terahertz radiation from InAs induced by carrier diffusion and drift. *Physical Review B - Condensed Matter and Materials Physics*, 73(15):1–6, 2006.

[89] Antanas Reklaitis. Terahertz emission from InAs induced by photo-Dember effect: Hydrodynamic analysis and Monte Carlo simulations. *Journal of Applied Physics*, 108(5), 2010.

[90] M. Nakajima, M. Hangyo, M. Ohta, and H. Miyazaki. Polarity reversal of terahertz waves radiated from semi-insulating InP surfaces induced by temperature. *Physical Review B - Condensed Matter and Materials Physics*, 67(19):1–7, 2003.

[91] G. Klatt, D. Stephan, F. Hilser, R. Gebs, A. Bartels, M. Fischer, J. Faist, and T. Dekorsy. Terahertz emission from lateral photo-Dember currents. *2010 Conference Proceedings - ICECom: 20th International Conference on Applied Electromagnetics and Communications*, 18(5):3842–3849, 2010.

[92] M. E. Barnes, S. A. Berry, P. Gow, D. McBryde, G. J. Daniell, H. E. Beere, D. A. Ritchie, and V. Apostolopoulos. Investigation of the role of the lateral photo-Dember effect in the generation of terahertz radiation using a metallic mask on a semiconductor. *Optics Express*, 21(14):16263, 2013.

[93] Raimund Mueckstein, Michele Natrella, Osama Hatem, Joshua R Freeman, Chris S Graham, Cyril C Renaud, Alwyn J Seeds, Edmund H Linfield, A Giles Davies, Paul J Cannard, Mike J Robertson, Dave G Moodie, and

Oleg Mitrofanov. Near-Field Analysis of Terahertz Pulse Generation From Photo-Excited Charge Density Gradients. *IEEE Transactions on Terahertz Science and Technology*, 5(2), 2015.

[94] C. D. Wood, O. Hatem, J. E. Cunningham, E. H. Linfield, A. G. Davies, P. J. Cannard, M. J. Robertson, and D. G. Moodie. Terahertz emission from metal-organic chemical vapor deposition grown Fe:InGaAs using 830 nm to 1.55 μm excitation. *Applied Physics Letters*, 96(19):98–101, 2010.

[95] Masato Suzuki and Masayoshi Tonouchi. Fe-implanted InGaAs photoconductive terahertz detectors triggered by 1.56 μm femtosecond optical pulses. *Applied Physics Letters*, 86(16):1–3, 2005.

[96] O. Hatem, J. Cunningham, E. H. Linfield, C. D. Wood, A. G. Davies, P. J. Cannard, M. J. Robertson, and D. G. Moodie. Terahertz-frequency photoconductive detectors fabricated from metal-organic chemical vapor deposition-grown Fe-doped InGaAs. *Applied Physics Letters*, 98(12):1–4, 2011.

[97] J. R. Middendorf and E. R. Brown. THz generation using extrinsic photoconductivity at 1550 nm. *Optics Express*, 20(15):16504, 2012.

[98] N Chimot, J Mangeney, L Joulaud, P Crozat, H Bernas, K Blary, and J F Lampin. Terahertz radiation from heavy-ion-irradiated $In_{0.53}Ga_{0.47}As$ photoconductive antenna excited at 1.55 μm. *Applied Physics Letters*, 2005.

[99] R. Salas, S. Guchhait, S. D. Sifferman, K. M. McNicholas, V. D. Dasika, E. M. Krivoy, D. Jung, M. L. Lee, and S. R. Bank. Growth and properties of rare-earth arsenide InGaAs nanocomposites for terahertz generation. *Applied Physics Letters*, 106(8), 2015.

[100] Keisuke Murakumo, Yuya Yamaoka, Naoto Kumagai, Takahiro Kitada, and Toshiro Isu. Photoconductivity of Er-doped InAs quantum dots embedded in strain-relaxed InGaAs layers with 1.5μm cw and pulse excitation. *Japanese Journal of Applied Physics*, 55(4), 2016.

[101] B. Sartorius, H. Roehle, H. Künzel, J. Böttcher, M. Schlak, D. Stanze, H. Venghaus, and M. Schnell. All-fiber terahertz time-domain spectrometer operating at 1.5 μm telecom wavelengths. *Optics Express*, 16(13):9565–9570, 2008.

[102] Toptica. Photoconductive Switches, https://www.toptica.com/products/terahertz-systems/time-domain/photoconductive-switches/, 2021.

[103] Masahiko Tani, Kwang-Su Lee, and X.-C. Zhang. Detection of terahertz radiation with low-temperature-grown GaAs-based photoconductive antenna using 1.55 μm probe. *Applied Physics Letters*, 77(9):1396–1398, 2000.

[104] H Erlig, S Wang, T Azfar, H R Fetterman, and D C Streit. LJ-GaAs detector with 451 fs response at 1.551m via two-photon absorption. *Electronics Letters*, 35(2), 1999.

[105] T. Kataoka, K. Kajikawa, J. Kitagawa, Y. Kadoya, and Y. Takemura. Improved sensitivity of terahertz detection by GaAs photoconductive antennas excited at 1560 nm. *Applied Physics Letters*, 97(20):1–4, 2010.

[106] P. Grenier and J.F. Whitaker. Subband gap carrier dynamics in low-temperature-grown GaAs. *Applied Physics Letters*, 70(15), 1997.

[107] Hany S. Loka, Seldon D. Benjamin, and Peter W.E. Smith. Optical characterization of low-temperature-grown GaAs for ultrafast all-optical switching devices. *IEEE Journal of Quantum Electronics*, 34(8):1426–1436, 1998.

[108] PW Yu, GD Robinson, JR Sizelove, and CE Stutz. 0.8-eV photoluminescence of GaAs grown by molecular-beam epitaxy at low temperatures. *Physical Review B*, 49(7):4689–4694, 1994.

[109] C. Tannoury, M. Billet, C. Coinon, J. F. Lampin, and E. Peytavit. Low-temperature-grown gallium arsenide photoconductors with subpicosecond carrier lifetime and photoresponse reaching 25 mA/W under 1550 nm CW excitation. *Electronics Letters*, 56(17):897–899, 2020.

[110] Hironaru Murakami, Tomoya Takarada, and Masayoshi Tonouchi. Low-temperature GaAs-based plasmonic photoconductive terahertz detector with Au nano-islands. *Photonics Research*, 8(9):1448, 2020.

[111] Aleksandar D. Rakić and Marian L. Majewski. Modeling the optical dielectric function of GaAs and AlAs: Extension of Adachi's model. *Journal of Applied Physics*, 80(10):5909–5914, 1996.

[112] Sadao Adachi. Optical dispersion relations for GaP, GaAs, GaSb, InP, InAs, InSb, $Al_xGa_{1-x}As$, and $In_{1-x}Ga_xAs_yP_{1-y}$. *Journal of Applied Physics*, 60(6030), 1998.

[113] Shunji Ozaki and Sadao Adachi. Spectroscopic ellipsometry and thermoreflectance of GaAs. *Journal of Applied Physics*, 78(5):3380–3386, 1995.

[114] D. Streb. Optical characterization of low temperature grown GaAs by transmission measurements above the band gap. *Journal of Vacuum Science & Technology B: Microelectronics and Nanometer Structures*, 14(3):2275, 1996.

[115] Toptica. Toptica FemtoFiber Pro IR Specifications, https://www.toptica.com/products/psfs-fiber-lasers/femtofiber-pro/femtofiber-pro-ir/, 2021.

[116] Mikhail F. Limonov, Mikhail V. Rybin, Alexander N. Poddubny, and Yuri S. Kivshar. Fano resonances in photonics. *Nature Photonics*, 11(9):543–554, 2017.

[117] Wonjoo Suh, Zheng Wang, and Shanhui Fan. Temporal coupled-mode theory and the presence of non-orthogonal modes in lossless multimode cavities. *IEEE Journal of Quantum Electronics*, 40(10):1511–1518, 2004.

[118] Lumerical. Lumerical FDTD, https://www.lumerical.com/products/fdtd/, 2021.

[119] S D Gedney. *Introduction to the Finite-Difference Time-Domain (FDTD) Method for Electromagnetics*. Synthesis lectures on computational electromagnetics. Morgan & Claypool, 2011.

[120] Lumerical. Overcoming the Multi-Wavelength FDTD Challenge, https://www.lumerical.com/learn/whitepapers/overcoming-the-multi-wavelength-fdtd-challenge/, 2021.